Discipline of Engineering & Energy
College of Science, Health, Engineering & Education

Investigation of Indentations versus Surface Roughness for Fluid Induced Motion of an Elastically Attached Circular Cylinder at Velocities Relevant to the Marine Environment using CFD

David Plant*

Dissertation submitted to the

Discipline of Engineering & Energy

College of Science, Health, Engineering & Education

Murdoch University

for the partial fulfilment of

Master of Renewable and Sustainable Energy

2019

* Tel: +61 456 611 015
Email: david@repowerplant.com.au

Declaration

I declare that this dissertation is my own account of my research, except where acknowledged and referenced, and contains as its main content work which has not previously been submitted for a degree at any tertiary education institution.

David Plant

May 2019

Abstract

Vortex induced vibration aquatic clean energy (VIVACE) is a renewable energy (RE) device being developed that uses multiple oscillating circular cylinders in one degree of freedom to produce electrical energy due to fluid induced motion (FIM). VIVACE is a modular system intended for use in ubiquitous slow velocity water flows of rivers, tides and ocean currents. Velocities of 1 to 5 knots are to slow for use by turbines and represents a massive opportunity for widespread, continuous RE power.

VIVACE currently uses passive turbulence control (PTC), a pair of symmetrical roughened surfaces on the circular cylinder to increase amplitudes and therefore increase power output. PTC works by effecting the fluid-structure interaction (FSI) within the boundary layer and the separation of the water from the cylinder creating changes in the characteristics of forces on the cylinder. The problem with a roughened surface in the marine environment is become fouled by marine organisms and therefore lose its effectiveness.

The intent of this research is to investigate the likelihood of biofouling of the PTC and suggest an alternative using indentations partially covering a circular cylinder to act in a similar wat to PTC increasing amplitudes. Indentations are an alternative design because they have smooth surfaces which can be treated with anti-biofouling coatings while still creating the disturbance to the boundary layer mechanism that causes the increased amplitude.

A review of FIM, FSI and computational fluid dynamics (CFD) is conducted to inform the research. A literature review is conducted on topics of current FIM technologies, surface roughness and indentation research on FIM and marine biofouling. The literature analysis strongly suggests that biofouling will be an issue for the current VIVACE PTC design. CFD using ANSYS is conducted to baseline the design against existing studies and then investigate four cases of indentations. Of the four indentation designs trialled they produce a reduced amplitude compared to PTC or completely dampened FIM. Further research with improved computational resources is required to complete this work.

Keywords: fluid induced motion, vortex induced vibration, galloping, dimples, passive turbulence control, roughened surfaces

Contents

Abstract iii
List of Figures vi
List of Tables viii
List of Abbreviations ix
List of Definitions ix
Antonyms xiii
Nomenclature xiii
Frequencies xiii
Basic Terms xiii
Coefficients xiv
Masses xv
Non-dimensional parameters for an elastically mounted cylinder in a fluid xv
Other nomenclature xv
Acknowledgements xvi
1 Introduction 1
1.1 Fluid Induced Motion (FIM) 3
1.2 VIV Description and Problem Definition 8
1.2.1 Vortex induced vibration (VIV) 8
1.2.2 Problem Definition and Aim of Research 9
1.3 FIM Terminology 11
1.3.1 Reynolds Number 11
1.3.2 Reduced velocity 13
1.3.3 Damping ratio and Griffin Plots 14
1.3.4 Mass ratio 17
1.3.5 Vortices analysis 18
1.3.6 Amplitude versus Reduced Velocity 19
1.3.7 Boundary Layer 21
1.4 Computational Fluid Dynamics Terminology 23
1.4.1 CFD Process 23
1.4.2 Numerical Analysis by CFD 25
1.4.3 Mesh Quality 26
1.4.4 Turbulence Models 28
1.4.5 Pressure-Velocity Couplings Methods 30
1.4.6 The Law of the Wall and y+ 30
2 Literature Review 32
2.1 FIMEG Technologies 32
2.2 Surface Roughness 35

2.2.1 Complete Roughness Cover 36
2.2.2 Localised Roughness 36
2.2.3 Passive Turbulence Control 37
2.3 Dimples and Channels 39
2.4 Marine Biofouling 41
2.5 Computational Fluid Dynamics (CFD) for Surface Texturing 42
3 Model Design and CFD Setup 44
4 PTC CFD Comparison 53
5 Indentation Cylinder CFD Results and Discussion 63
5.1 Dimple Case 1 (D1) – Five indentations, Same $kd/D = 6.05x10-3$, Arc 20° - 60° 63
5.2 Dimple Case 2 (D2) – Three indentations, Varying $kd/D = 6.05x10-3 - 1.21x10-2$, Arc 20° - 43° 64
5.3 Dimple Case 3 (D3) – One indentation, $kd/D = 8x10-3$, Arc 55° 64
5.4 Dimple Case 4 (D4) – One indentation, $kd/D = 8x10-3$, Arc 15° 66
5.5 Discussion of Results 66
6 Conclusion and Recommendations 68
References 71
Appendix 1 – Fluid Domains A1-1
Appendix 2 – Sub-domain Mesh Diagrams A2-1

List of Figures

Figure 1: Vortices about a rigid cylinder from fixed cylinder analysis using ANSYS Fluent 2

Figure 2a: Boundary layer development of flat plate showing flow regimes (Çengel and Ghajar 2011, figs. 6–14) 4

Figure 2b: Velocity amplitude with elevation from the wall (taken from figure 2a) highlighting the difference in velocity changes (a) in the laminar boundary layer and (b) in the turbulent boundary layer 5

Figure 2c: Representations of fluid flow around a solid circular structure (Groh 2016) 6

Figure 2d: Pressure gradients of the fluid (air) and infrared colours describing heat transfer in air around a smooth cylinder (Scobie, Sangan, and Lock 2014) 6

Figure 3: Classification of vortex induced motion (Rostami and Armandei 2017, 195) 7

Figure 4: Reynolds numbers of varying circular cylinders diameters versus maritime environment water speeds with tidal turbine systems annotated (Z. Zhou et al. 2014) 10

Figure 5: Reynolds number versus coefficient of drag for various 2D shapes (Munson, Young, and Okiishi 1998) 11

Figure 6: Modified Griffin plot with adjusted for Reynolds number and least-squares fit (Soti et al. 2018) 17

Figure 7: Peak amplitude vs reduced velocity for multiple damping ratio $\boldsymbol{m * \zeta = 0.013}$ showing all three response branches of VIV (Khalak and Williamson 1999, fig. 2) 18

Figure 8: Schematic diagram showing modes of vortices from an elastically mounted cylinder (Williamson and Govardhan 2004, C–1) 19

Figure 9a: Peak amplitude (top 10% max amplitude responses) vs reduced velocity for multiple damping ratios (Soti et al. 2018). 2200<Re<6661 and m*=3.0. Blue and red indicate upper and lower branches respectively. Note how the upper branch dissolves as damping increases. 20

Figure 9b: 2-DOF Traces (Sarpkaya 2004) 20

Figure 10: (a) Turbulent boundary layers (Savory and Toy 1989, fig. 11) (b) Diagram of cylinder wake and layer terminology (Williamson 1996, fig. 4) 21

Figure 11: Definition of critical Reynolds number and the effect of rough surfaces explained later (Alonzo-García et al. 2015, fig. 1) 22

Figure 12: (a) Skewness (ANSYS 2019c, fig. 54) (b) orthogonal quality (ANSYS 2019c, fig. 58) 27

Figure 13: Aspect ratio examples for triangles (ANSYS 2016, fig. 399) and quadrilaterals (ANSYS 2019c, fig. 44) .. 28

Figure 14: Jacobian Ratio Examples (ANSYS 2016, figs. 46–48) 28

Figure 15: Comparison of different modelling approaches to turbulent spatial scales (Hart 2016, fig. 1) 29

Figure 16: The Law of the Wall Figure (Pletcher, Anderson, and Tannehill 1984, 224) 31

Figure 17: Pictorial representation of Vortex Hydro Energy (Vortex Hydro Energy 2019) 33

Figure 18: Comparison of CFD turbulence models for spheres versus experimental data 44

Figure 19: Model Domain Design 45

Figure 20: Image of the total domain 47

Figure 21: Mesh diagrams (a) Overall mesh (b) Sections including inlet (blue), outlet (red), cylinder (centre grey) and outer-wall (top and bottom grey) 49

Figure 22: Residual plots for three PTC grid sizes (a) course (b) medium (c) fine 52

Figure 23: Position of cylinder during frame freezes for pressure and velocity analysis around PTC and how they appear in the figures 24 below from frame 1 on the bottom to frame 3 on top. 53

Figure 24: Comparison of pressures and velocities as the cylinder is in motion for three different Re of 30,000 (left) and 90,000 (right) 54

Figure 25: Ding et al (Ding et al. 2016, fig. 8) Re=30,000 displacement ratio and frequency spectrum 57

Figure 26: Current Study PTC Re=30,000 displacement ratio and frequency spectrum showing the same scales as figure 25 and then more realistic scales 57

Figure 27: Ding et al (Ding et al. 2016, fig. 8) Re=60,000 displacement ratio and frequency spectrum 58

Figure 28: Current Study PTC Re=60,000 displacement ratio and frequency spectrum showing the same scales as figure 27 and then more realistic scales 58

Figure 29: Ding et al (Ding et al. 2016, fig. 8) Re=90,000 displacement ratio and frequency spectrum 59

Figure 30: Current Study PTC Re=90,000 displacement ratio and frequency spectrum showing the same scales as figure 29 and then more realistic scales 59

Figure 31: Amplitude measured by video stills for Re=30,000 in Photoshop CC© 60

Figure 32: Amplitude measured by video stills for Re=90,000 in Photoshop CC© 61

Figure 33: Correction factors for cylinder position as reported by Fluent 62

Figure 34: Actual data for amplitude ratio and frequency spectrum for PTC of Re=30,000 62

Figure 35: Pressure and velocity diagrams for D1 at Re=30,000 63

Figure 36: Five dimple setup results for amplitude ratio and frequency spectrum at Re=30,000 64

Figure 37: Case D3 pressure contours and velocity vectors at varying levels of zoom. 65

Figure 38: D4 results of amplitude and frequency spectrum at Re=30,000 before simulation failure 66

List of Tables

Table 1 Characteristics of FIM by classification (Rostami and Armandei 2017, 194–98) 8

Table 2 Dimensional quantities important in predicting VIV for an elastically mounted smooth cylinder in a turbulent-free stream 9

Table 3 Characterisation of Reynolds number regimes for a circular cylinder wake (Zdravkovich 1990, 54–55; Raghavan and Bernitsas 2011, 720) 15

Table 4: Model physical properties (Ding et al. 2016, 1248–49) 45

Table 5: Pressure-Velocity Coupling Solution Scheme for Grid Independence Study 50

Table 6: Grid Sensitivity Study Re=30,000 50

Table 7: Pressure-Velocity Coupling Solution Scheme for PTC and indentations 52

Table 8: Comparison of amplitude ratio and frequency ratio between Ding et al (2016) and current study 56

Table 9: Measurement comparisons of amplitude ratio using images 60

List of Abbreviations

AF	Antibiofouling
CFD	Computational fluid dynamics
DDES	Delayed DES
DES	Detached eddy simulation model
DOF	Degree-of-freedom
DNS	Direct numerical simulation model
FIM	Flow induced motion
FIMEG	Flow induced motion energy generator
FR	Fouling-release (with reference to biofouling)
FSI	Fluid structure interaction
$k-\varepsilon$	Turbulence kinetic energy (k) and rate of dissipation of k (ε) turbulence model
$k-\omega$	Turbulence kinetic energy (k) and specific rate of dissipation of k (ω) turbulence model
LES	Large eddy simulation model
MAPDL	Mechanical ANSYS parametric design language
MRELab	Marine renewable energy laboratory
MUSCL	Monotonic upwind scheme for conservation laws
PISO	Pressure implicit splitting operation
PIV	Particle-image velocimetry
PTC	Passive turbulence control
PhD	Doctor of Philosophy degree
RANS	Reynolds averaged Navier-Stokes turbulence model
SA	Spalart-Allmaras model
SAS	Scale adaptive simulation model
SCESP	Smooth cylinder equivalent separation point
SIMPE	Semi-implicit method for pressure linked equations
SRS	Scale resolving simulations model
SST	Shear stress transport
TO-SLIPS	Tungsten oxide slippery liquid-infused porous surfaces
TrBL	Transition of bubble layer
TrSL	Transition of shear layer
URANS	Unsteady RANS turbulence model
VHE	Vortex Hydro Energy
VIV	Vortex induced vibration
VIVACE	Vortex induced vibration aquatic clean energy

List of Definitions

Added Mass
: The increase in effective mass that occurs when the acceleration of a body is nonzero. This is also called the hydrodynamic mass. The inference is that the effective mass is the sum of the mass of the body and the added mass. The added mass doesn't influence the situation until there is acceleration.

ANSYS
: An engineering simulation software company based in the United States that produces the computation fluid dynamics software used in this study.

Betz limit
: Theoretical maximum power conversion efficiency that can be extracted from an open flow fluid equal to 59.62%.

Bluff body

A structure is said to be a bluff body if its drag profile is dominated by pressure drag while a body is streamlined if it is dominated by frictional drag. An aerofoil shape is streamlined while a cylinder is a bluff body.

Boundary layer

An area close to the boundary of a solid and fluid moving relative to each other where the effects of viscosity are significant. This results in a reduced velocity near the surface of the solid.

Channel

A rounded indentation spanwise along the cylinder.

Coefficient of drag

The ratio of the drag force to the force produced by the dynamic pressure times the area.

Coefficient of lift

The ratio of the lift force to the force produced by the dynamic pressure times the area.

Computational fluid dynamics

The use of computers to simulate fluid flows to examine the properties of pressure, velocity, temperature, density and viscosity. It may or may not be associated with interactions with solid objects.

Critical Reynolds number

The critical Reynolds number is where the minimum value for the coefficient of drag C_D is reached on a C_D versus Re graph. This value will be at the bottom of rapid decrease in C_D called the drag crisis.

Damping

The dissipation of energy from restraining vibratory motion.

Damping factor

The sum of all damping, specifically for VIV the sum of material and fluid damping.

Dimple

A dimple is defined as an indentation made by part of a sphere inlaid into the surface.

Drag crisis

On a coefficient of drag, C_D, versus Reynolds number graph the decrease and subsequent increase of C_D due to unstable boundary layer separation.

Flow geometry

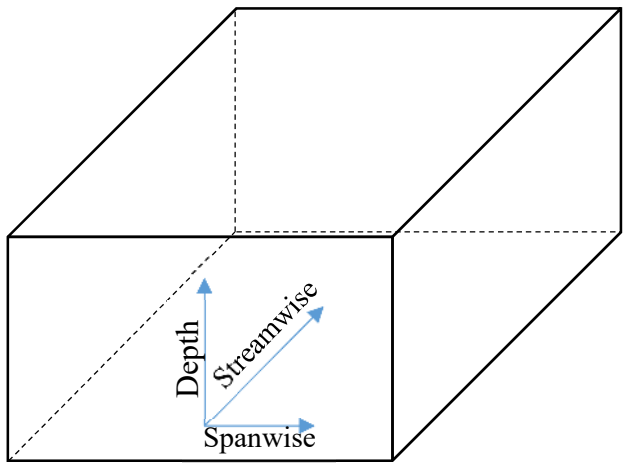

Fluid (or viscous or velocity-squared) damping

Viscous damping is caused by such energy losses as occur in liquid lubrication between moving parts or in a fluid

forced through a small opening by a piston, as in automobile shock absorbers. The viscous-damping force is directly proportional to the relative velocity between the two ends of the damping device. The motion of a vibrating body is also checked by its friction with the gas or liquid through which it moves. The damping force of the fluid in this case is directly proportional to a quantity slightly less than the square of the body's velocity and, hence, is referred to as velocity-squared damping.

Fluid-structure interaction
: The interaction between a solid but movable or deformable object and the internal or external fluid flow.

Forced vibration
: Vibrations caused by external excitations to the system. In VIV forced vibrations are driven externally at an exact frequency, amplitude and Reynolds number throughout the range of f_{ex}/f_{st}. Also see self-excited vibration.

Free vibration
: Vibrations caused by initial displacement of the system, but no further force is applied. Objects will vibrate at their natural frequency. Also see self-excited vibration.

Griffin plot
: A log-log plot of predicted maximum structural displacements as a function of the mass-damping parameter constructed initially from collection of mass and damping experimental data by Griffin, Skop and Ramberg in 1975.

Inertia
: Resistance to change or motion.

Inertia Coefficient
: Also called the added mass coefficient C_A. The in-phase component of the lift force.

Laminar
: Flow of fluid which follows consistent streamlines in the direction of the flow. Opposite of turbulent flow.

Lock-in
: Lock-in condition is established when the local vortex shedding frequency coincides with the local crossflow vibration frequency.

Mass-damping ratio
: The product of the reduced mass and damping factor

Material (or structural or hysteresis) damping
: It is composed of grain friction, dislocation friction and the presence of microscopic voids. It is caused by material deformation as the structure comes under forces and moves against itself consuming some of the energy of the motion. It is not fluid damping.

Reduced mass
: The total oscillating structure mass divided by the displaced fluid mass.

Reduced velocity
: The fluid approach velocity normalized by frequency and diameter.

Resonance
: A phenomenon in which a vibrating system or external force drives another system to oscillate with greater amplitude at a limited range of frequencies. Specifically, resonance occurs when the frequency of the applied force is close to one of the natural frequencies of vibration of the driven system.

Reynolds number
: The ratio of inertia forces and viscous forces in a fluid experiencing varying velocities. Another way to consider Reynolds number is the balance between kinetic energy and viscous damping. High Reynolds numbers indicate

that the viscous forces are small (approaching inviscid) while low Reynolds numbers indicate viscosity is having a major effect.

Roughness
: A random vertical feature with and average height above the surface.

Self-excited vibrations
: The vibration is initiated and/or controlled by the characteristics of the object and the fluid domain. The vibration is self-sustaining and may increase destructively.

Separation point
: The point on a curved surface where the boundary layer leaves the surface and does not reattach.

Shear layer
: In a fluid with varying velocity the shear layer is where a significant velocity gradient exists between two flows.

Stagnation point
: A point on in FSI where the fluid velocity is zero. Normally referred to when occurring at the first contact point of the fluid on a bluff body.

Streamline
: The path of a particle in a fluid relative to a solid body past which the fluid is moving in smooth flow without turbulence.

Strip
: A spanwise section of texture of specified width starting at a specific angle around the cylinder from the front stagnation point.

Strouhal frequency
: The vortex shedding frequency of a body at rest. Related to Strouhal number by the velocity of the flow and the characteristic size of the body.

Strouhal number
: A dimensionless number describing oscillating flow mechanisms for fluid aft of a stationary cylinder. The parameter is named after Vincent Strouhal, a Czech physicist who experimented in 1878 with wires experiencing vortex shedding and singing in the wind.

Transition of shear layer/Transition of bubble layer
: The classification of flow regimes into groups based on the behaviour of the transition of the shear layer from laminar to turbulent in the boundary layer in the wake of a cylinder in a uniform liquid flow.

Turbulent flow
: A fluid flow in which the velocity of the fluid varies in magnitude and direction erratically compared to the overall fluid motion causing mixed flow and vortices within streamlines.

Viscosity
: A quantity expressing the magnitude of internal friction. For fluids it is a measure of its resistance to gradual deformation by shear stress or tensile stress. An example being water has a lower viscosity than honey.

von Kármán vortex street model
: A regular stream of vortices shed from a body placed in a fluid stream. Investigated and named after Theodore Von Kármán (1881–1963), a Hungarian-born engineer who advanced a formula for the frequency of the shed vortices in terms of the stream velocity and the dimensions of the body.

Vortex induced vibrations
: A non-linear complex phenomenon when vortex shedding is in a frequency range (see lock-in) close to the natural frequency of the body causing increased amplitude of oscillation. The hysteresis of the body and flow interaction cause the complex non-linear action of the body.

Vortex shedding

An oscillating flow that takes place when a fluid such as air or water flows past a bluff (as opposed to streamlined) body at certain velocities, depending on the size and shape of the body. In this flow, vortices are created at the back of the body and detach periodically from either side of the body.

Antonyms

Fluid damping	Velocity squared damping Viscous damping
Material damping	Hysteresis damping Structural damping
Parallel to flow	Head on In-line Lengthwise Straight on Streamwise
Perpendicular to flow	Crosswise Spanwise Transverse

Nomenclature

Frequencies

f – frequency of oscillation of a vibrating body (either forced or self-excited) regardless of whether lock-in is present (referred to as f_{ex} in Sarpkaya 2004)

f_N – natural frequency of a system

f_{Nvac} – natural frequency of a system as found in a vacuum

f_{N0} – natural frequency in the absence of fluid effects$= 1/2\pi\sqrt{k/m}$

f_{Nair} – natural frequency of a system in air

f_{Nwater} – natural frequency of a system in water $= 1/2\pi\sqrt{k/(m+m_a)}$

f_{vs} – vortex shedding frequency of a body in motion (forced or self-excited)

f_{St} – vortex shedding frequency (Strouhal frequency) of a body at rest

ω_n – f_N in radians/second

$\omega\ (also\ \omega_{vs})$ – f_{vs} in radians/second

Basic Terms

A – amplitude of cylinder vibration

A_r – reference area of a solid object being the area perpendicular to the fluid flow in the z plane

c – material damping per unit length

D - cylinder diameter

F_D – component of total fluid force in free stream direction in steady flow (drag force)

F_L – component of total fluid force in transverse direction in steady flow (lift force)

k – spring constant per unit length

k_d – roughness (protrusion) height or dimple (indentation) depth

K – lumped spring constant

l – vortex formation length

L - cylinder length

P - pressure

t – time

$\bar{u}$ – root mean squared turbulence velocity

U - flow velocity of free stream

V – volume of a body

x – instantaneous cylinder motion in inline direction

y – instantaneous cylinder motion in transverse direction

α_d – ratio of boundary layer depth at texture leading edge to texture depth, $= \delta_0/d$

$\alpha_{r,n}$ – angle from stagnation point to the leading edge of nth texture

α_s – angle from the stagnation point to the separation of the boundary layer

δ – boundary layer thickness

δ_0 – boundary layer thickness at texture leading edge

θ_n- angular coverage of the nth texture

$\theta_{n,s}$ - angle of the texture relative to the spanwise length (ie. sawtooth)

μ – dynamic viscosity

υ – kinematic viscosity

ρ – density

τ_w- wall shear stress

ϕ – phase angle between fluid force and structure displacement

ψ – suppression (intentional) damping

Coefficients

C_D – drag coefficient, = $F_D/(\rho A_r L(U^2/2))$

C_L – lift coefficient, = $F_L/(\rho A_r L(U^2/2))$

C_A – potential added mass coefficient, = 1.0 for a circular cylinder (Govardhan and Williamson 2006)

Masses

m – also m_{osc}, total oscillation structure mass

m_a – added mass

m_c – cylinder mass

m_d – displaced fluid mass, $= \pi\rho D^2(L/4)$

m_A – ideal mass, $= C_A m_d$

Non-dimensional parameters for an elastically mounted cylinder in a fluid

A^* – amplitude ratio, = A/D

A^*_{max} – peak amplitude

A^*_n – peak amplitude as average of top n values

b* - damping parameter (Shiels, Leonard, and Roshko 2001), $= 2c/D\rho U$

c* - alternate damping parameter (Vandiver 2012), $= 2c\omega/\rho U^2$

f^* - frequency ratio, $= f/f_N$

L^* - aspect ratio, L/D

m^* - reduced mass or mass ratio, = m/m_d

Re – Reynolds number, $= (\rho UD)/\mu = UD/\upsilon$

Re_{crit} – Critical Reynolds number

Re_δ - Reynolds number at the leading edge of an indentation (groove or dimple)

U^* – also V_r, reduced velocity, velocity ratio or normalised velocity, = $U/f_N D$

U^*_t – 'true' normalised velocity (or renormalised velocity) (Williamson and Govardhan 2004); $= U^*/f^*$

α – mass-damping parameter, $= (m^* + C_A)\zeta$

ζ – damping ratio, = $c/2\sqrt{k(m + m_A)}$ (Scruton 1965)

Other nomenclature

K_C – Keulegan-Carpenter number, $(U_{max}t)/D = U_{max}/fD$

S_c – Scruton number, $= \pi^2 m^*\zeta$

S_G – Skop-Griffin parameter, $= 2\pi^3 {S_t}^2(m^*\zeta)$

S_t – Strouhal number, $= f_{st}(D/U)$

Acknowledgements

Supervisor	Dr Elaine Walker, Discipline of Engineering & Energy, Murdoch University
Coordinator	Dr Xiangpeng Gao, Lecturer Energy Studies, Murdoch University
	Dr Johnathan Whale, Academic Chair Energy Studies, Murdoch University

1 Introduction

Flowing water in rivers, tides and ocean currents is a renewable energy source. The source of energy for rivers is the sun, due to part of the global water cycle of evaporation, condensation, precipitation over land and then gravity causing surface runoff to rivers that then flow back to large water bodies or into ground storage. For tides, the energy is mostly from the gravitational action between large water bodies and the moon and to a lesser extent the sun, creating a continuous cycle. Extracting useful work from water flows has been practiced since the early Bronze Age using water wheels and similar. Since the industrial revolution humanity's increasing reliance on electricity to produce useful work has brought a higher demand for energy. This has led to water motion being increasingly used as an economic and low carbon emission method to produce electricity. The two most common methods for extracting this energy is to use kinetic energy directly, such as tidal turbines that are like wind turbines in water or to entrap the water using dams or dykes, storing its potential energy making it available as required via Pelton turbines or similar. Whatever method currently used; turbines are the most common method for extracting the energy. A significant issue for tidal turbine generators is the velocity of the water required to turn the turbine efficiently with average water flows of 5-7 knots required ruling out many locations (Lee and Bernitsas 2011, 1698), and even in good locations only around 10 hours a day are available due to the diurnal nature of tides. An alternative approach that can utilise the motion of the water at decreased velocities to produce electricity would be beneficial both from a siting perspective and for less intermittency of power in the tidal case.

One approach is to use the same phenomenon that cause wires to create a humming noise in certain wind conditions, first investigated by Czech physicist Vincenc Strouhal (1850-1922). The telegraph wire vibrates because of the air's interaction with the wire as it flows past. When the vibration of the wire back and forth is at a frequency that can be detected by human hearing it is colloquially described as 'humming'. This research led to many further and ongoing studies of fluid-structure interaction (FSI), the forces involved and phenomena such as large amplitudes of vibration create when the induced vibration frequency is near the natural frequency of the object. Objects that do not display aerodynamic characteristics such as square blocks and circular cylinders are defined as bluff bodies. Figure 1 shows vortices being simulated by water behind a bluff body, in this case a solid fixed circular cylinder.

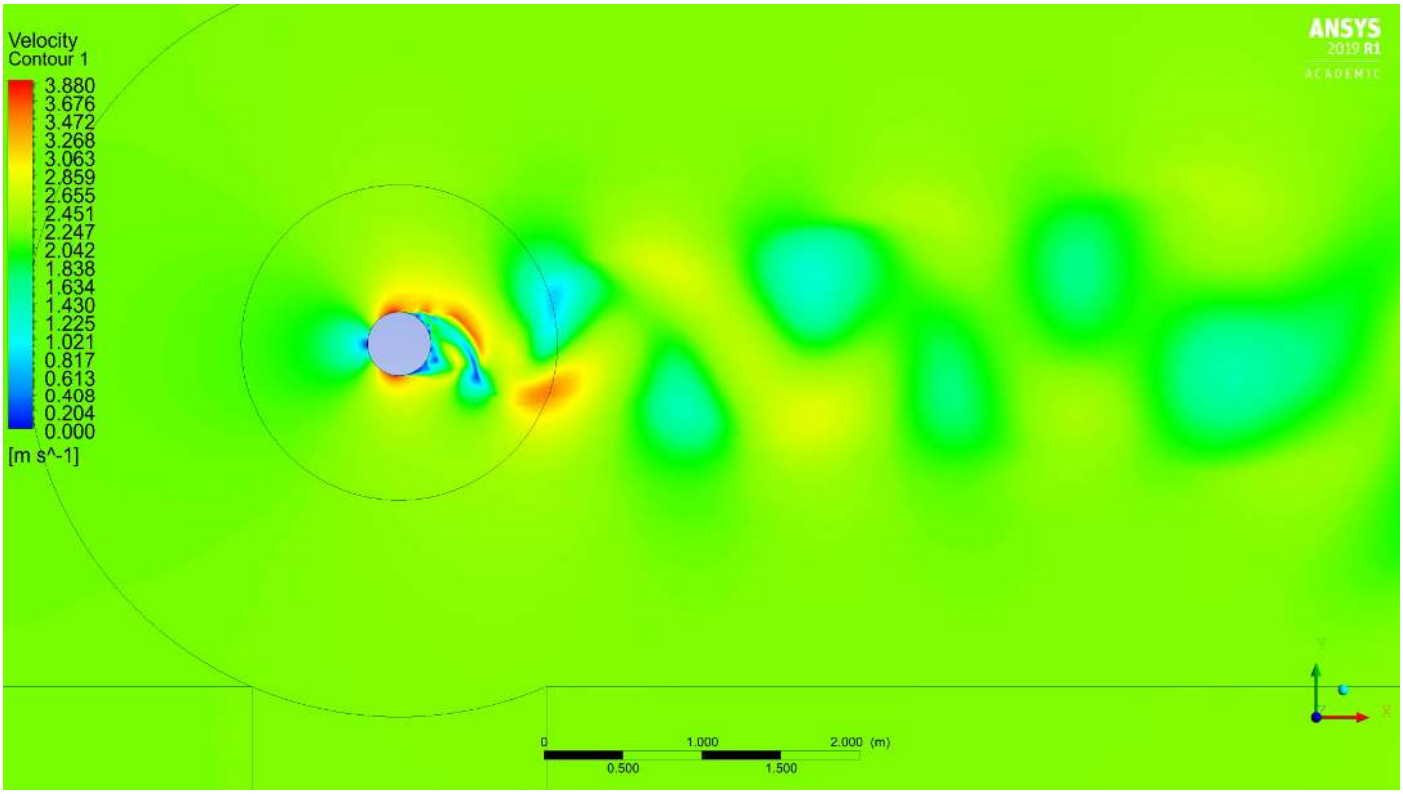

Figure 1: Vortices about a rigid cylinder from fixed cylinder analysis using ANSYS Fluent

In engineering applications, flow induced motions (FIM) have been considered something to be avoided because they create increased stress on the object being vibrated. Research efforts in FIM have concentrated on understanding the phenomena with the aim to avoid its destructive nature in applications such as aerofoil design for wings and wind turbines, architecture of buildings, bridges and industrial funnels as well as in marine applications including oil and gas risers and oil rig structures. The oscillations of the Tacoma Narrows Bridge from FIM and its resultant collapse in 1940 due to torsional failure is a classic example of the reason for such interest (Koughan 1996; Arioli and Gazzola 2015).

The phenomena of FIM has recently been utilised to develop renewable energy devices described throughout this paper as flow induced motion energy generators (FIMEG). Specific devices include the Vortex Bladeless (2019; Villarreal 2018) utilising wind and the vortex induced vibration aquatic clean energy (VIVACE) system developed by the University of Michigan and it's start-up offshoot Vortex Hydro Energy (VHE) (2019; Bernitsas 2015). VIVACE is developed for water velocities from around 1 knot to 5 knots found in rivers, tides and ocean currents. To achieve improved energy output across this range of relatively slow water velocities, the VIVACE system uses roughened strips along a small arc of the front of the cylinder to increase the FSI and therefore amplitude of vibration.

The research objective of this paper is to contribute to existing knowledge being used for the development of VIVACE by:

- Investigating the likelihood of biofouling on the existing surface texturing of VIVACE in the marine environment, and

- Investigating an alternative design utilising smooth indentation with anti-biofouling coating.

This will be achieved in two parts. The first objective is to confirm the hypothesis that biofouling will be an issue for the current VIVACE design via a desktop study. The second and main part of the study is computational fluid dynamics (CFD) analysis of the alternate design and the comparison of results with the VIVACE design.

The remainder of section 1 develops a deeper understanding of FIM, states the problem to be investigated and broadens understanding of essential terminology. Section 2 is a literature review to inform the remainder of the research in this paper. Section 3 will detail the model designs of the VIVACE cylinder and the indented alternative, explain CFD optimisation methods and explain the CFD setup. A comparison of this papers VIVACE roughened cylinder CFD simulation results with existing literature is made in section 4 to confirm reliability of the setup. Section 5 will contain results and analysis of the proposed alternative design. A summary and conclusion will be presented at the end including next steps for future research.

For clarity in this paper, an xyz coordinate system will be used with the nomenclature defined as x direction is streamwise, y direction spanwise and z direction depth as shown in the list of definitions on page x. The table of antonyms on page xiii list other terms that may be used by other researchers and texts.

1.1 Fluid Induced Motion (FIM)

Forced vibration is a physical term for an object that is being forced by an external input and capable of vibration because of its elasticity, the elasticity of its fixings or by being pivoted. FIM is a phenomenon resulting from forced vibration of a bluff body due to FSI. FSI is the complex nature of fluid behaviour as it is diverted around and, depending on velocity of the fluid, the separation from the structure. From fluid dynamics, a fluid moving relative to a

solid object exerts pressure and viscous forces with two components of the resultant forces, lift and drag. Lift is the component of the force perpendicular (spanwise) to the flow while the drag component is in the flow direction (streamwise). Lift and drag forces have the same equation $F = 1/2\,\rho U^2 C A_r$ where C is the coefficient of lift or drag (C_L and C_D respectively), ρ is the fluid density, U is the free stream velocity and A_r is the reference area. The reference area for bluff bodies is the area of the object in the z plane perpendicular to the flow and for a cylinder will be a square. The coefficient value is not constant and depends on the fluid properties, structure shape and position. In order to correctly predict the lift and drag forces on an object knowledge of the pressure fields and FSI is required. This translates to requiring an understanding of boundary layer and flow separation action. Figure 2a through 2c give an illustration of these terms and FSI.

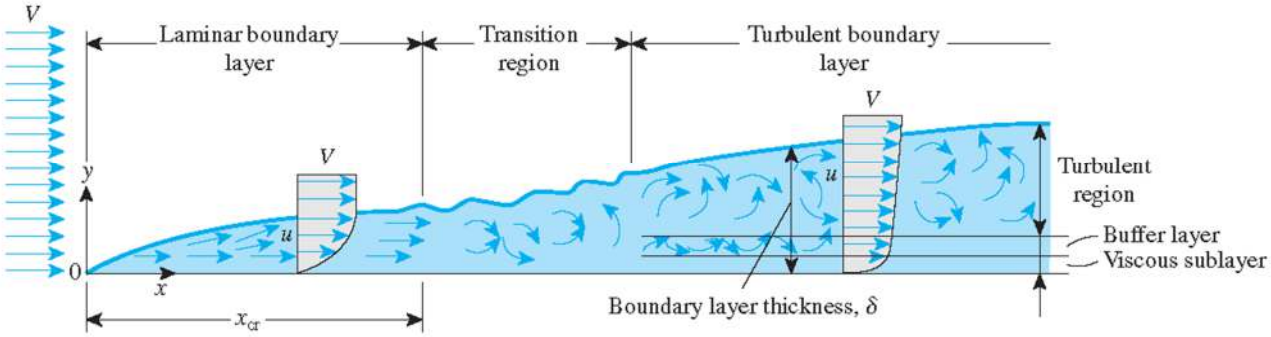

Figure 2a: Boundary layer development of flat plate showing flow regimes (Çengel and Ghajar 2011, figs. 6–14)

Figure 2a shows the boundary layer development along a flat plate to explain some terms and behaviours. When a fluid flows over a solid surface the fluid layer in contact with the solid has zero velocity and is said to be 'no slip'. This is illustrated in figure 2b by the velocity amplitude with elevation diagrams from figure 2a and the difference observable in the acceleration in fluid flow as the distance from the wall increases. In the viscous boundary layer, the velocity increase is constant as it leaves the wall and then increases gradually. The velocity in the turbulent boundary layer is quite stable and increasing very slowly in the viscous sub-layer and then rises very quickly towards the border of the buffer sub-layer with the associated increase in turbulence.

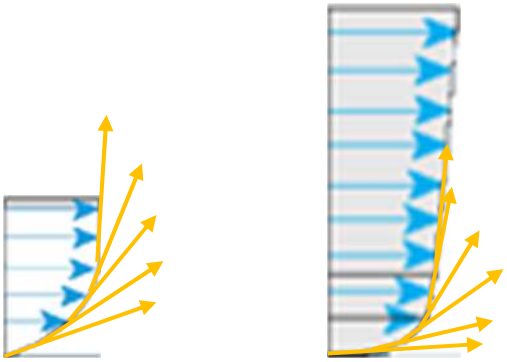

Figure 2b: Velocity amplitude with elevation from the wall (taken from figure 2a) highlighting the difference in velocity changes (a) in the laminar boundary layer and (b) in the turbulent boundary layer

The boundary layer δ is defined as the distance from the surface of the solid to a point perpendicular where the velocity is 99% of the free fluid velocity. The boundary layer thickness increases with the distance along the solid surface and velocity gradients increases between the no-slip layer and the boundary layer edge. At a certain point the gradients reach a level where they transition from laminar to turbulent flow intermittently, and then return to laminar flow, called the transition region. As the depth of the boundary layer continues to grow the transition region becomes more turbulent than laminar until eventually the boundary layer is fully turbulent in all but small sub-layers close to the solid surface. The sub-layers consist of a buffer layer that is much like the transition region being part laminar and part turbulent until the fully laminar viscous sub-layer is reached extending to the surface of the solid.

Figure 2c and 2d illustrates the flow over a curved surface where the boundary layer is influenced by the velocity of the fluid, the fluid viscosity and density, the solid shape and the roughness of the solid surface. A non-dimensional Reynolds number, which will be described in detail later, is used to represent most of these values. Two drag forces are at play, skin friction and form drag. Skin friction drag is due to the viscous shearing between the surface and the layer of fluid in contact with it called wall shear stress. Skin friction drag is calculated by the product of the wall shear stress τ_w and the area over which it is acting. Form drag is the result of changes of pressure gradients at the surface of the solid. The dynamic pressure is the pressure resulting from the conversion of kinetic energy of the flow into pressure at the surface and is a component of the total drag force which is equal to the dynamic pressure and the area over which it is acting times a drag coefficient. The boundary layer separation point is when the pressure at the surface reaches zero and the bottom of the boundary layer becomes detached. Form drag is due to the reversal of pressure at the surface of the solid after boundary layer separation and a reversal of the fluid velocity. Above a Reynolds number of around 5 the boundary layer separates off the solid surface and creates a free shear layer as

shown in figure 2c and 2 d as the dashed line leaving the separation point. This free shear layer is initially folded into steady voices or 'bubbles' behind the cylinder. With a high enough Reynolds number, the resulting flow becomes turbulent and begins to create vortices wakes in patterns behind the cylinder called von Karman street. The balance between inertia and viscous forces within the fluid strongly influence the resultant wakes.

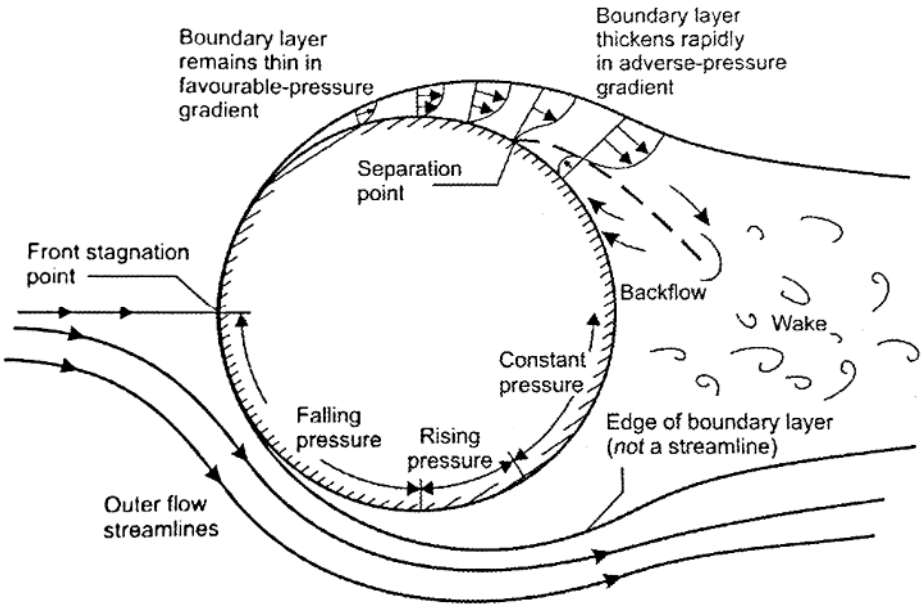

Figure 2c: Representations of fluid flow around a solid circular structure (Groh 2016)

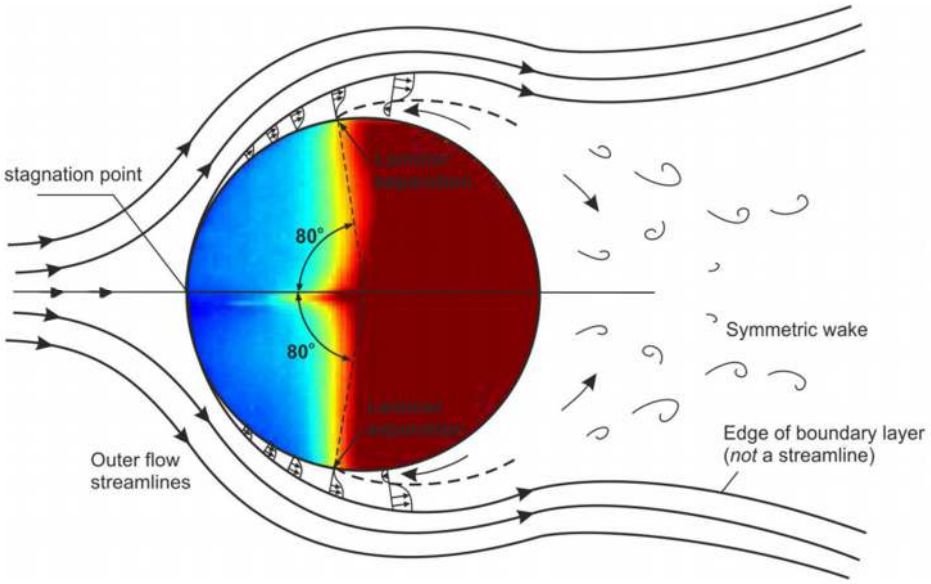

Figure 2d: Pressure gradients of the fluid (air) and infrared colours describing heat transfer in air around a smooth cylinder (Scobie, Sangan, and Lock 2014)

The physics of FIM are complex, non-linear and strongly influenced by many parameters. As an example Sarpkaya (2004) highlights that for a steady flow around a fixed structure the shear layer separation is strongly influenced by the Reynolds number and is well understood. With FIM, the motion of the structure and the alternating acceleration/deceleration creates unpredictable and complex transitions of the flow and separation points. There is much still unknown, in conjecture and unsubstantiated with regards to FIM and predicting its physical properties. From the literature review and reading on this topic one main factors that makes this topic so difficult and hinders the ability to study FIM in experiments and simulations is the number of variables involved including the fluid type, degrees of freedom of the structure, the structure rigidity, the elasticity of the endpoint attachments, solid object end conditions, relative distance to other objects including walls and free versus forced oscillations. As many of these factors as possible have been reduced to simplify this research.

FIM has been classified by FSI phenomena (Rostami and Armandei 2017) as seen in figure 3. Resonance FIM is where oscillations correspond with the natural frequency of the structure while instability refers to force changes over time due to the motion of the structure (Rostami and Armandei 2017, 194). The further sub-categorisation is based on the physics properties relating to the development of the phenomena. For resonance this relates to the flow effects on the structure, for instability it refers to the nature of the motion and is then further sub-categorised by degrees of freedom for galloping. A structure may transition through multiple FIM, an example being a cylinder with a single degree of freedom transitioning from vortex induced vibration (VIV) to galloping as Reynolds number increases (Sun et al. 2016, 936–37). A comparison of physical properties of FIM by phenomena is detailed in table 1.

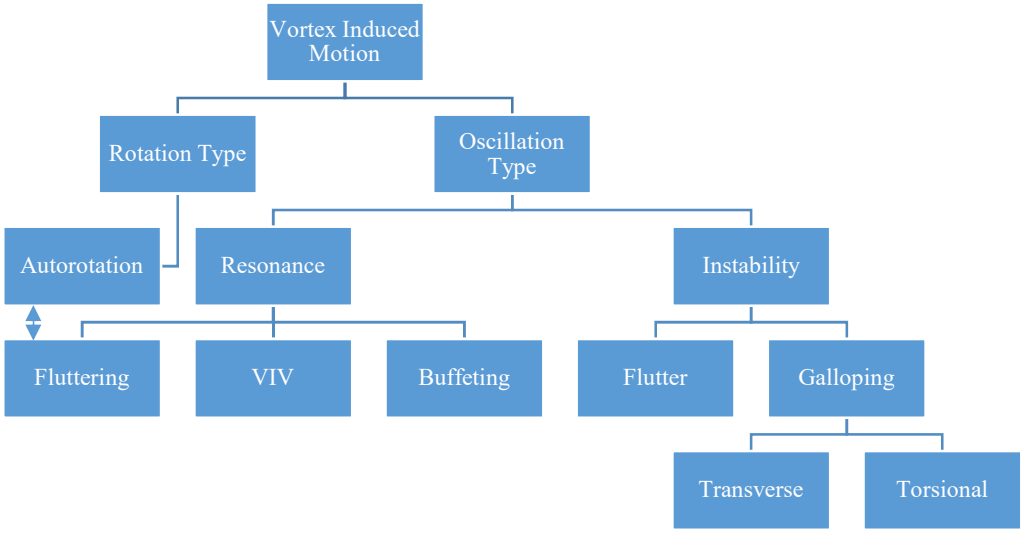

Figure 3: Classification of vortex induced motion (Rostami and Armandei 2017, 195)

Table 1
Characteristics of FIM by classification (Rostami and Armandei 2017, 194–98)

VIV	Vortex induced vibrations. Self-limiting stable oscillation due to steady external flow moving around an elastic or elastically attached non-rotatable bluff body creating vortex shedding and asymmetric pressure forces around the body. VIV is pronounced when the natural frequency of the bluff body and the frequency of vortex shedding are in synchronisation.	
Buffeting	Oscillations caused by an unsteady incoming flow stream.	
Fluttering	Angular oscillation of a freely rotatable bluff body in a steady external flow experiencing forces on the face of the body and vortex shedding aft of the body relative to the incoming flow. Angular oscillations become rotation under certain conditions (see autorotation).	
Flutter	Self-limiting stable oscillation due to steady external flow, elastic instability and an inertial coupling exists between the 2DOF of a streamline body. A cut-in flow velocity initiates the oscillation. A typical example is when the centre of lift on an aerofoil moves aft of the centre of gravity.	
Galloping	Instability within the object or its attachment mechanism cause externally excited oscillations (such as VIV) to magnify from internal forces.	
	Transverse	Limited to motion transverse to the incoming flow.
	Torsional	Limited to motion in the direction of the incoming flow.
Autorotation	Similar mechanism to fluttering except for the movement is continuous rotation instead of angular oscillation caused by the specific geometry of the body and enough moment of inertia. Stable autorotation may occur after a period of chaotic fluttering-autorotation combined.	

1.2 VIV Description and Problem Definition

1.2.1 Vortex induced vibration (VIV)

VIV has been studied in detail (Khalak and Williamson 1997, 1999; Sarpkaya 2004; Williamson and Govardhan 2004; Gabbai and Benaroya 2005; Govardhan and Williamson 2006; Williamson and Govardhan 2008; Bearman 2011) to understand the complex nature of the formation of vortices from fixed and elastically attached bluff bodies in a disturbance free fluid flow. In particular the interactions that establish large forced vibrations when near resonance with the natural frequency of a solid cylinder based on the total oscillating mass have been studied in detail (Garcia and Bernitsas 2018, 453). Vandiver (2012, 112) lists dimensional quantities important to predictions of VIV response for elastically mounted cylinders in table 2, all of which are encompassed by up to three fundamental units; mass, length and time.

Table 2
Dimensional quantities important in predicting VIV for an elastically mounted smooth cylinder in a turbulent-free stream

A	Amplitude of cylinder response
c	Damping constant per unit length
D	Cylinder diameter
k	Spring constant per unit length
L	Length of cylinder
m	Mass (without added mass) per unit length
U	Free stream fluid velocity
k_d	Roughness height
$\bar{u}$	Root mean squared turbulence velocity
ω	Excitation frequency in radians/second
ρ	Density of the fluid
μ	Dynamic viscosity

Some of the values in table 2 are fixed or well defined for the marine environment. Other depend solely on the design of the FIMEG. A reasonable size cylinder for VIV in the ocean could be quite large to capture the slower velocities as shown in figure 4 however for this study a diameter the same as the VIVACE is used to allow for direct comparison of results. It has been concluded from the above studies, and those identified below, that there are four parameters important for the study of VIV for an elastically attached smooth circular cylinder (Soti et al. 2018, 295); Reynolds number (Re), damping ratio (ζ), mass ratio (m*) and reduced velocity (U*) all of which will be further explained. All these parameters are important because they allow for the prediction of vibration average maximum amplitude (A_n^*) for a circular cylinder under specific conditions which relates directly to the maximum power available from a FIMEG (Lee and Bernitsas 2011, 1698).

1.2.2 Problem Definition and Aim of Research

To improve the efficiency and/or power output over Reynolds numbers relevant to the marine environment, surface roughness has been an active area of study (Jadidi et al. 2018; Zeinoddini et al. 2017; Park, Kumar, and Bernitsas 2016; Gao et al. 2015; Chang, Kumar, and Bernitsas 2011). A partially roughened cylinder surface causes changes in the behaviour of FIM regarding amplitudes at relevant marine velocities (Achenbach 1971; Achenbach and Heinecke 1981).

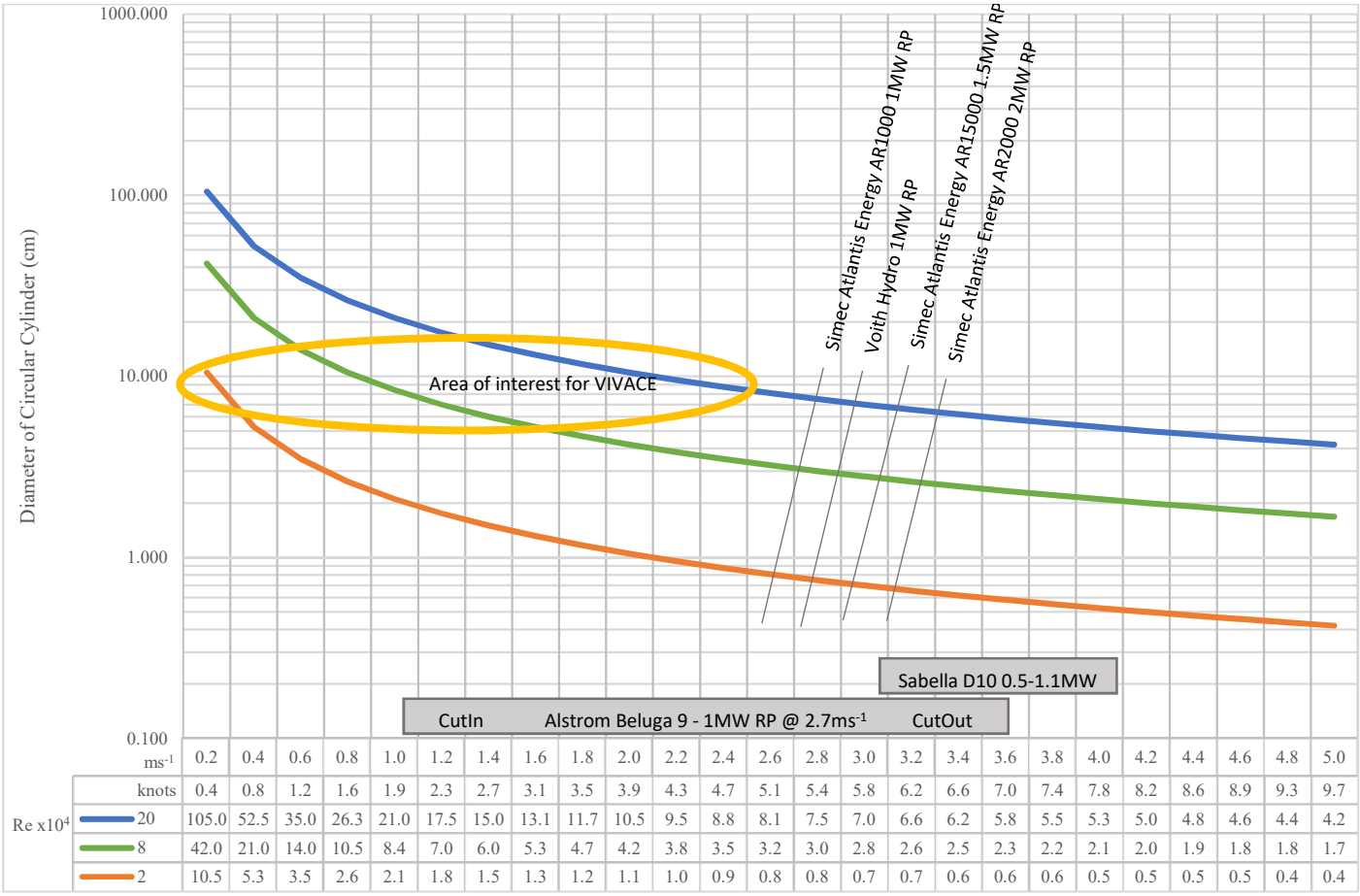

	ms-1	0.2	0.4	0.6	0.8	1.0	1.2	1.4	1.6	1.8	2.0	2.2	2.4	2.6	2.8	3.0	3.2	3.4	3.6	3.8	4.0	4.2	4.4	4.6	4.8	5.0
	knots	0.4	0.8	1.2	1.6	1.9	2.3	2.7	3.1	3.5	3.9	4.3	4.7	5.1	5.4	5.8	6.2	6.6	7.0	7.4	7.8	8.2	8.6	8.9	9.3	9.7
Re x10^4	20	105.0	52.5	35.0	26.3	21.0	17.5	15.0	13.1	11.7	10.5	9.5	8.8	8.1	7.5	7.0	6.6	6.2	5.8	5.5	5.3	5.0	4.8	4.6	4.4	4.2
	8	42.0	21.0	14.0	10.5	8.4	7.0	6.0	5.3	4.7	4.2	3.8	3.5	3.2	3.0	2.8	2.6	2.5	2.3	2.2	2.1	2.0	1.9	1.8	1.8	1.7
	2	10.5	5.3	3.5	2.6	2.1	1.8	1.5	1.3	1.2	1.1	1.0	0.9	0.8	0.8	0.7	0.7	0.6	0.6	0.6	0.5	0.5	0.5	0.5	0.4	0.4

Figure 4: Reynolds numbers of varying circular cylinders diameters versus maritime environment water speeds with tidal turbine systems annotated (Z. Zhou et al. 2014)

Surface roughness of a cylinder also affects the transition between FIM categorise of VIV and galloping (Park, Kumar, and Bernitsas 2013). The problem with a rough surface in the marine environment is twofold: roughened surfaces will promote biofouling and a fixed roughness is optimised for a specific fluid flow angles onto the cylinder which is unlikely to be realistic in real operation. Biofouling is the action of marine organisms to attach themselves to structures and will be discussed in the literature review. It is hypothesised that an alternative approach is to use smooth surface indentations to produce the desired alterations to FIM behaviour with reduced likelihood of biofouling. Partially and symmetrically covering the front edge of the cylinder (between 10° and 60° from the front stagnation point) in indentations may also give an increased approach angle of the flow without reducing effectiveness. There is no open literature found that discusses or investigates the flow of water over a cylinder partially covered with dimples other than Zhou et al (2015) who investigated half cover cylinders either fully into the flow, at 90° or 180°.

1.3 FIM Terminology

1.3.1 Reynolds Number

The introduction highlighted the importance of inertia and viscous forces because of the effect it has on the separation point from a circular cylinder. The relationship between inertia, a measure of resistance to change, and the viscosity, a fluids resistance to flow, is expressed as a dimensionless quantity, is given in equation 1.1, the Reynolds number.

$$Re = (\rho UD)/\mu \tag{1.1}$$

with ρ the density of the fluid, U the free flow velocity, D the cylinder diameter and μ the dynamic viscosity.

The Reynolds number is important in FIM because it informs the critical points at which the boundary layer flow around a cylinder will change from laminar to transitional and then turbulent and the separation point of the boundary layer (Niemann and Hölscher 1990, 198). As many experiments are conducted at fixed diameters and/or flow velocities it is often used as the independent variable (x-axis) in analysing results. Figure 5 is a plot of common shapes with coefficients of drag, C_D versus Reynolds number.

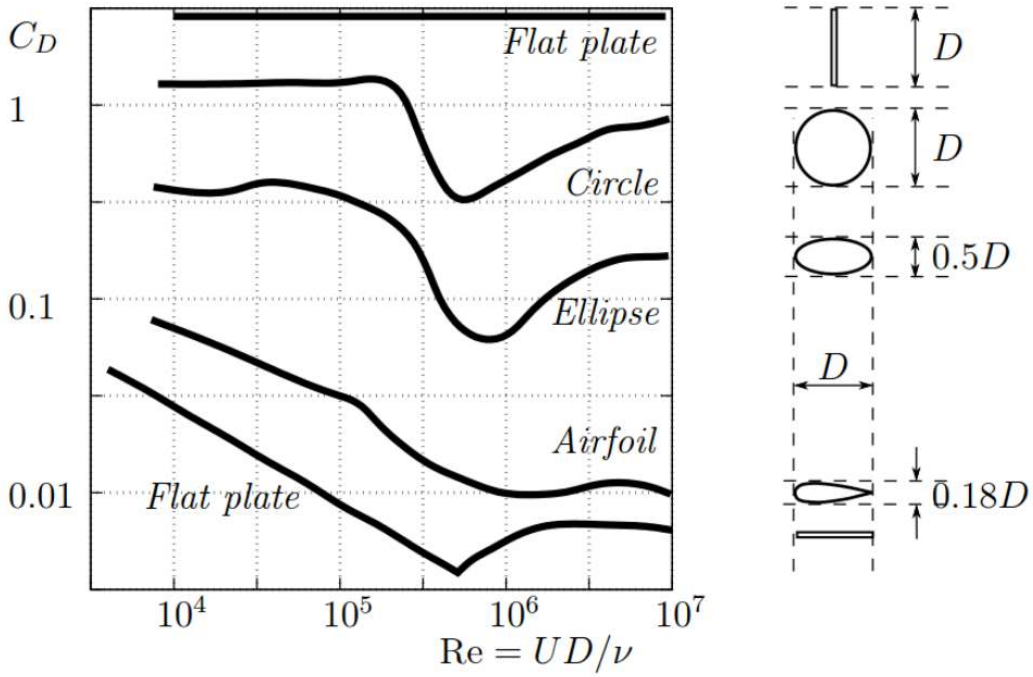

Figure 5: Reynolds number versus coefficient of drag for various 2D shapes (Munson, Young, and Okiishi 1998)

The study of high Reynolds numbers is important because the majority of marine rivers, tides and ocean currents are in the $2\text{x}10^4 < Re < 3\text{x}10^5$ (Lee and Bernitsas 2011, 1698) depending on salinity, depth, temperature and excluding surface effects such as swell and seas. Investigating FIM with respect to these high Reynolds number of is problematic with limited facilities designed to conduct experiments and its highly complex nature requires powerful computers that have only recently evolved to a sufficient level capable of the numerical calculations. Facilities capable of performing testing for high Reynolds numbers in a controlled environments including ExxonMobil, University of Michigan, California Institute of Technology (Caltech) and Cornell University (Raghavan and Bernitsas 2011, 719). Numerous low Reynolds number studies (Williamson and Govardhan 2004) have been conducted however the use of low 'idealized' Reynolds numbers to suggest the characteristics of high Reynolds numbers has received much negative critical review. Sarpkaya (2004) highlighted the complexity of the situation stating "flow kinematics … under highly idealized circumstances … is far from sufficient to draw scientific and/or industrially significant conclusions regarding the dynamic similarity of self-excited and forced oscillations."

Classification of how Reynolds numbers affect the flow around smooth circular cylinder was compiled by Roshko and Fiszdon (1969) and Schewe (1983) who looked at regimes of flow in depth. Schewe concentrated his efforts in the area where the boundary layer becomes fully turbulent and the effect on wake characteristics. This area is defined by a sharp drop in the coefficient of drag C_D and is termed the 'drag crisis' while at its lowest point of C_D the Reynolds number is termed critical Reynolds numbers Re_{crit}. The drag crisis begins with the boundary layer separating and then reattaching creating 'separation bubbles' and disturbance in the shear wake. As the Re continues to climb the separation bubble shifts sides. At the bottom of the drag crisis, the critical Reynolds number, is when the single separation bubble is replaced by two simultaneous bubbles and the C_D begins to increase again as stability in the boundary layer shedding is increased. The C_D levels at the end of the drag crisis with the boundary layer transitioning to fully turbulent (Zdravkovich 1997, chap. 6). Later clarification and reclassification by Niemann and Hölscher (1990, 199) and Zdravkovich (1990, fig. 2, 1997, fig. 1.11) produced the current classification reproduced in Table 3 which provides greater depth of classification in the sub-critical regime below the critical Reynolds number (Zdravkovich 1990, 54–55; Raghavan and Bernitsas 2011, 720). It can be seen from table 3 that the area of interest for this study, referring to figure 4 of $2\text{x}10^4 < Re < 2\text{x}10^5$ range, is in the transition regimes from the late TrSL2 through to early TrBL0. The effects of Reynolds number in this range include:

- The amplitude ratio increases with Re in high damping situations (Lee and Bernitsas 2011, 1700).

- Reynolds numbers close to $7.5x10^4$ achieved maximum efficiency

  $\eta = power\ out/power\ in = power\ out/\frac{1}{2}\rho DLU^3 = 33\%$

  where ρ is the fluid density and L is the length of the cylinder (Soti et al. 2018; Sun et al. 2016).

- High amplitude ratios of $A^*_{max} = 3$ have been proven experimentally during galloping at reduced velocities of U*>10 ($\sim Re > 1.05\text{x}10^5$) using partial surface roughness (Chang, Kumar, and Bernitsas 2011, fig. 1731).

1.3.2 Reduced velocity

For a fixed cylinder diameter, the reduced velocity and Reynolds number can be used interchangeably and is seen to be used on several graphs in the literature together along the x axis. The reduced velocity U^* is a non-dimensional value of the free flow velocity normalised by the natural frequency of the cylinder and the diameter of the cylinder.

$$U^* = U/fD \tag{1.2}$$

given U, the free flow velocity, f the frequency of the oscillating cylinder of diameter D. Rearranging equation (1.1) for U gives

$$U = Re\mu/D\rho \tag{1.2.1}$$

Substituting equation (1.2.1) into equation (1.2) gives the relationship between Reynolds number and reduced velocity

$$U^* = Re\mu/fD^2\rho \tag{1.2.2}$$

'Free flow' velocity means that the incoming flow is laminar, being free from disturbances. The 'true' reduced velocity U^*_t is where the natural frequency of the cylinder is replaced with the actual oscillating frequency (Khalak and Williamson 1999).

1.3.3 Damping ratio and Griffin Plots

Damping is the loss of energy from vibration. The mechanism for the energy loss is either intentional or through the physical properties of the system. In FIM there is intentional damping (referred to hereafter as 'suppression' and designated ψ Greek phi) and damping from the material properties and interaction with the fluid. A parameter used to consider damping was first developed by Scruton (1955) and later introduced to the research community (Scruton 1965) to became known initially as the Scruton number as shown in equation 1.3. It was used to aid the understanding of flow-induced vibration of tall structures such as chimney stacks in wind by associating it with maximum amplitude of vibration values near the structures natural frequency termed 'lock-in'.

$$Sc = \pi^2 m^* \zeta \tag{1.3}$$

where m^* is the mass ratio (equation 1.3.1) and ζ is the damping ratio (equation 1.3.2) as in

$$m^* = m/m_d \tag{1.3.1}$$

$$\zeta = c/2\sqrt{k(m + m_A)} \tag{1.3.2}$$

with m being the mass of the oscillating cylinder, m_A the added mass, c is the material damping per unit length and k is the spring constant.

Further development of the damping parameter was conducted to predict peak amplitudes associated with flow-induced motion across many shapes to increase its usefulness. A plot used to consider peak-amplitude A^*_{max} versus the 'Skop-Griffin' parameter S_G was introduced after considerable data analysis from various experiments (Griffin, Skop, and Ramberg 1975) and later revised as a linear vertical plot (Khalak and Williamson 1999) called a 'Griffin plot'. The Griffin plot represents the relationship between peak vibration amplitude of a cylinder undergoing VIV and the product of mass and damping. It has been established to fit peak amplitude at zero mass-damping over a range of Reynolds numbers.

Table 3
Characterisation of Reynolds number regimes for a circular cylinder wake (Zdravkovich 1990, 54–55; Raghavan and Bernitsas 2011, 720)

Reynolds number range	Name of the regime	Characteristic feature	General properties
$Re < 1$		Creeping flow	**Laminar regime**
$3–5 < Re < 30–40$	L	Steady separation (recirculation bubble)	
$30–40 < Re < 150–300$	L	Periodic laminar shedding	
$150–300 < Re < 1 \times 10^5–2 \times 10^5$	TrW and TrSL		**Subcritical regime:** laminar separation transition in shear layer turbulent wake
$150 –200 < Re < 200–250$	TrW1	Transition of laminar vortices in wake,	
$200–250 < Re < 350–500$	TrW2	Transition of irregular vortex during its formation	
$350–500 < Re < 1 \times 10^3–2 \times 10^3$	TrSL1	Development of transition waves in free shear layer	
$1 \times 10^3–2 \times 10^3 < Re < 2 \times 10^4–4 \times 10^4$	TrSL2	Formation of transition vortices in free shear layer	
$2 \times 10^4–4 \times 10^4 < Re < 1 \times 10^5–2 \times 10^5$	TrSL3	Fully turbulent shear layer	
$1 \times 10^5–2 \times 10^5 < Re < 3.5 \times 10^5–6 \times 10^6$	TrBL		**Critical regime:** laminar separation turbulent reattachment turbulent separation Turbulent wake
$1 \times 10^5–2 \times 10^5 < Re < 3 \times 10^5–3.1 \times 10^5$	TrS0/TrBL0	Onset of transition at separation point	
$3 \times 10^5–3.1 \times 10^5 < Re < 3.3 \times 10^5–3.4 \times 10^5$	TrS1/TrBL1	Single separation bubble regime	
$3.3 \times 10^5–3.4 \times 10^5 < Re < 3.6 \times 10^5–3.8 \times 10^5$		Unstable regime	
$3.6 \times 10^5–3.8 \times 10^5 < Re < 5 \times 10^5–1 \times 10^6$	TrS2/TrBL2	Two-bubble regime	
$5 \times 10^5–1 \times 10^6 < Re < 3.5 \times 10^6–6 \times 10^6$	TrS3/TrBL3	Supercritical regime—fragmented separation bubble.	
$3.5 \times 10^6–6 \times 10^6 < Re < 6 \times 10^6–8 \times 10^6$	TrBL4	Transcritical regime—partial transition	
$Re > 8 \times 10^6$	T	Postcritical regime—complete transition	

These equations are relevant and discussed here because they highlight some of the complexity and controversy surrounding the understanding of FIM. There has been much debate and criticism of mass damping as a predictor of FIM as reviewed by Sarpkaya (2004) as well as the meaning of added mass and its relevance to understanding of FSI. The uncertainty in the understanding of the VIV phenomenon based on an added mass and the spring-damping model $m^*\zeta$ is because it only produces accuracy in and around the systems natural frequency while VIV has been shown to occur outside these regions indicating that there a other factors having an influence on the FSI and resultant FIM (Garcia and Bernitsas 2018, 451–53). Given these limitations of the added mass model, further refinement has been conducted (Vandiver 2012; Shiels, Leonard, and Roshko 2001) to produce damping parameters for spring mounted cylinders that are independent of Reynolds number and can be used for peak amplitudes of VIV across all reduced velocities in the lock-in range. The Griffin plot was further refined and renamed the 'modified Griffin plot' to take into account and remove the effect of Reynolds numbers below 33,000 (Govardhan and Williamson 2006). This was achieved by adopting the mass-damping ratio $\alpha = m^*\zeta$ for a circular cylinder versus (Reynolds number adjusted) amplitude ${A^*}_M = A^*/{A^*}_{\alpha=0}$. Another refinement to the Griffin plot (Soti et al. 2018) has been proposed to improve the fitting function of peak amplitude to take into account asymptotic behaviour due to the logical case of a very large (towards infinite) amount of damping being required to completely supress the VIV as

$$A^*_{max} = A^*_0 \exp\left(\sum_{i=1}^{n} C_i \alpha^i\right) \tag{1.3.3}$$

with n=2, A^*_0 the peak vibration amplitude of the circular cylinder at zero damping and C_i are constants determined on a least-squares fit basis. An example of this plot is given in figure 6 with $C_1 = -0.940$ and $C_2 = -0.935$. Research continues to understand the relationship between FIM, mass and damping (Vandiver 2012; Garcia and Bernitsas 2018) and has resulted in further refinement to produce the damping parameter c^* which can be used to compile the coefficient of lift C_L data from experimental amplitude results by the relationship

$$C_L = A^* c^* \tag{1.3.4}$$

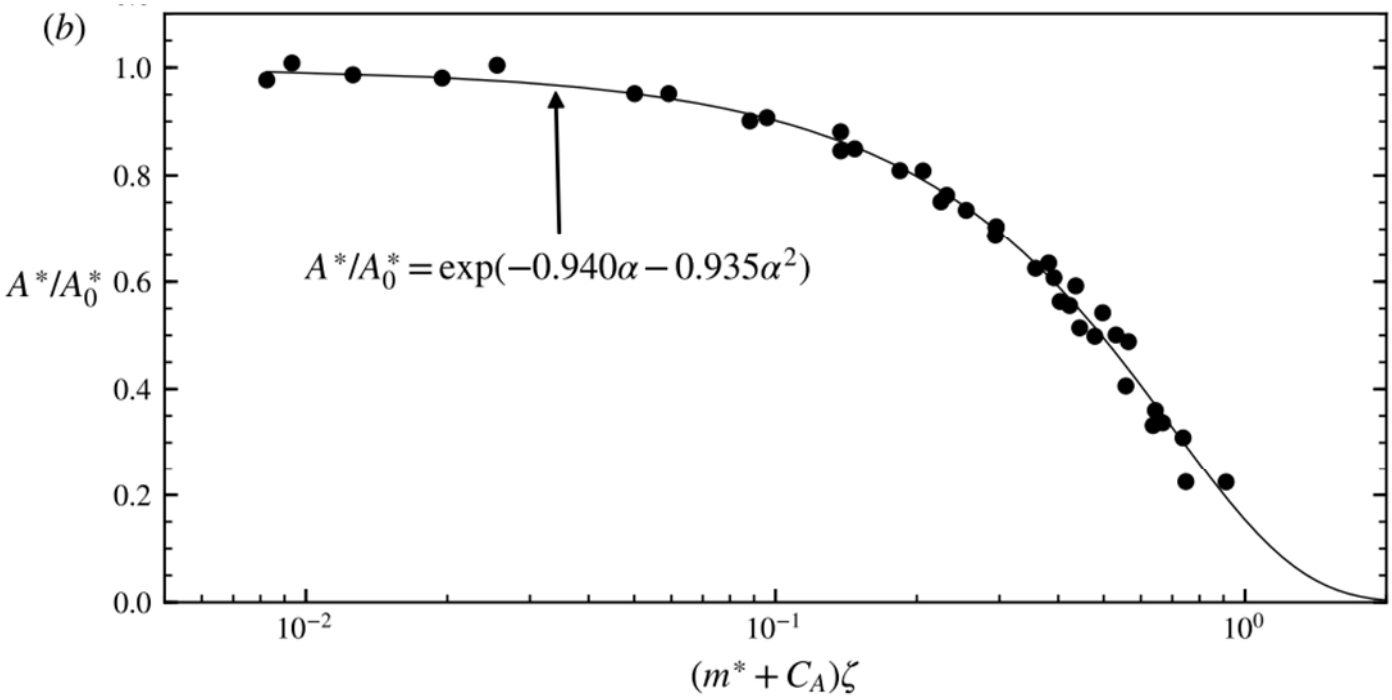

Figure 6: Modified Griffin plot with adjusted for Reynolds number and least-squares fit (Soti et al. 2018)

1.3.4 Mass ratio

FIM of a circular cylinder is influenced by the mass of the cylinder, the mass of the damping system and the mass of the displaced fluid as the cylinder moves. Typically, the damping system is an elastically mounted spring or springs. The cylinder mass to displaced fluid mass, termed mass ratio m^*, has been developed to take some of these varying masses into account. For an elastically sprung cylinder the effective spring mass of 1/3 the spring total mass is included in the total oscillating mass (Sun et al. 2016). Care needs to be taken in calculations of mass ratio to ensure that the definition of length is consistently applied as a per unit length of the cylinder or the whole cylinder. The mass ratio is important as it has implications for the formation of FIM. High mass ratios with low damping have some varying characteristics to low mass ratios while some stay the same. Figures 7 is a graph of amplitude ratio versus reduced velocity and shows three branches. These are examples of the variation of VIV lock-in due to mass ratio. All smooth cylinders in disturbance free flow appear to reach lock-in around a reduced velocity $\sim 5 < U^* < 8$ as a minimum while high mass/low damping cylinders do not reach the upper branch and for $m^* \sim 1$ the reduced velocity range is $\sim 5 < U^* < 10$ (Sun, Ma, and Bernitsas 2018, 491).

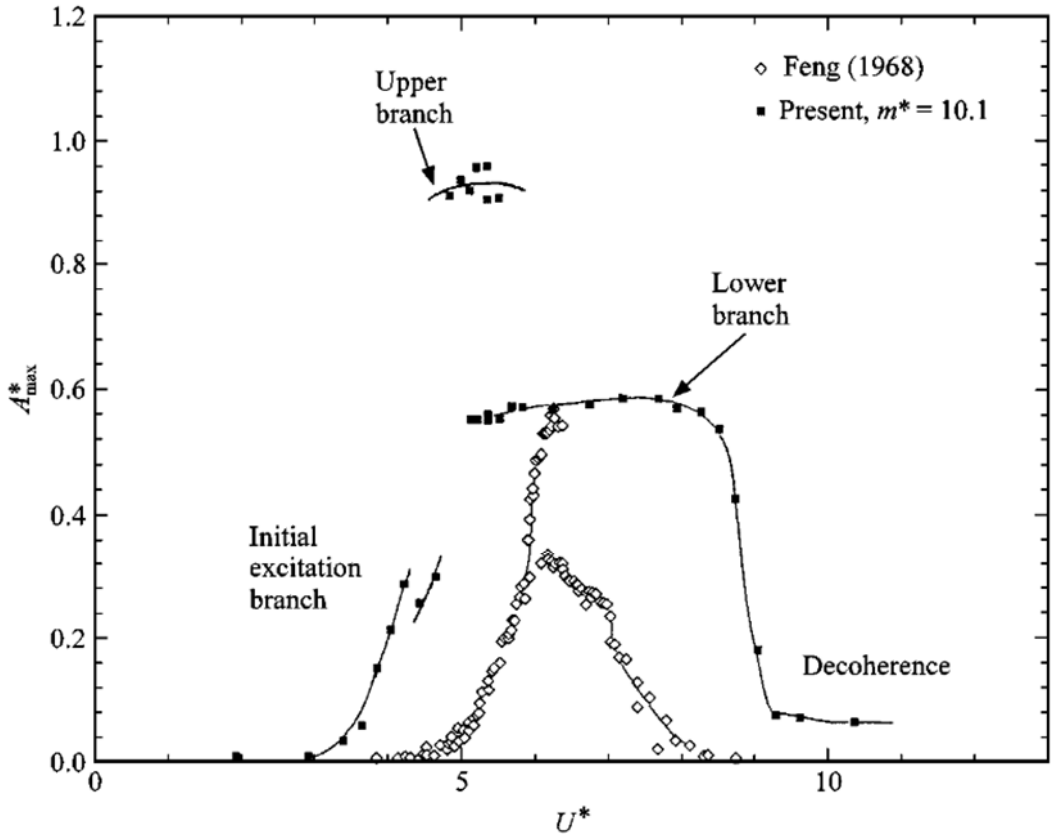

Figure 7: Peak amplitude vs reduced velocity for multiple damping ratio $\boldsymbol{m^*\zeta = 0.013}$ showing all three response branches of VIV (Khalak and Williamson 1999, fig. 2).

1.3.5 Vortices analysis

The formation of wake patterns produced by forced vibrations were considered by Williamson and Roshko (1988) and Brika and Laneville (1993) where patterns of vortices were recognised and classified into singletons (S) or pairs (P) formations such as two singular (2S), two pairs (2P) or a combination of both (P+S) as shown in figure 8 (Williamson and Govardhan 2004). These wake patterns are distinct modes of vortices found near the lock-in range, as defined previously, by increased vibrations near the natural frequency of the vibrating cylinder. Further combinations of vortices have been found including P, 2P-, 2P+2S and C being coalescence of numerous vortices into packets. Vortices classifications can be used to analyse the development of FIM through a vortex shedding map.

Vortices formation is a consequence of the FSI, pressure and viscous forces around the boundary layer and the subsequent boundary layer separation. Parameters affecting the boundary layer characteristics include the Reynolds number, surface roughness, flow state before interaction with the solid (i.e. disturbance free flow or disturbed flow

with turbulence), cylinder shape and end condition (Güven, Farell, and Patel 1980; Niemann and Hölscher 1990, 197; Park 2012, 8; Zdravkovich 1990, 53).

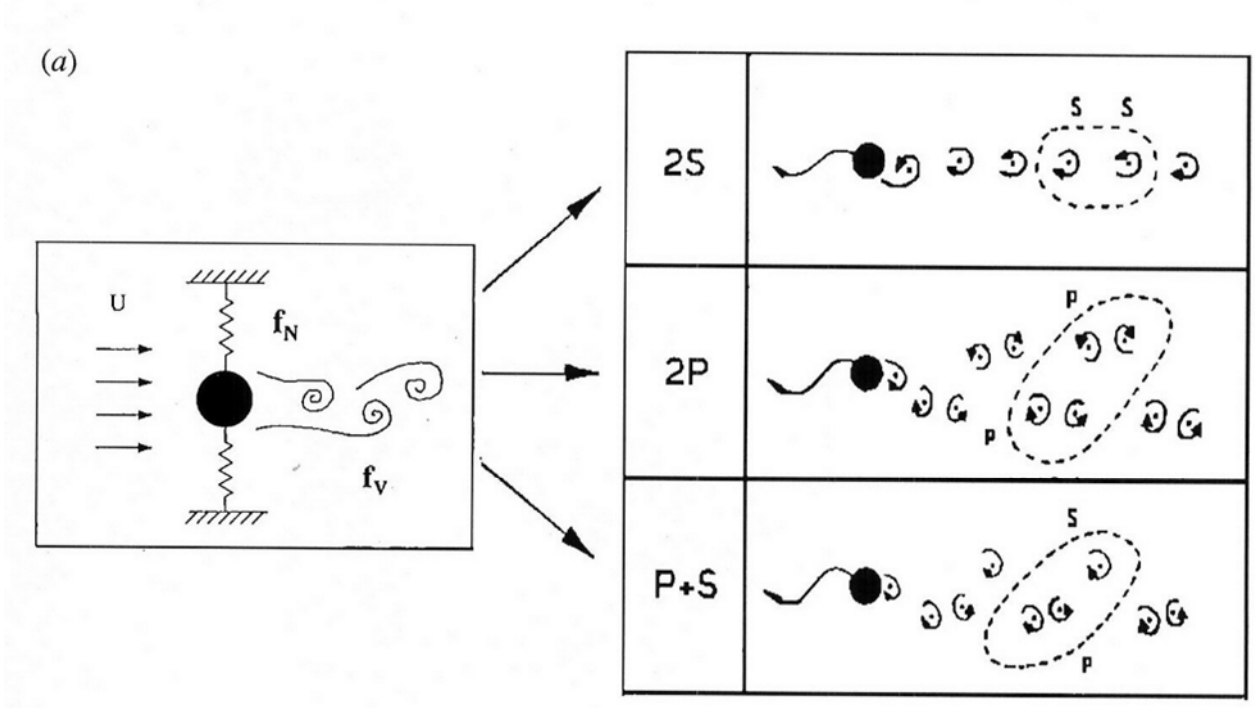

Figure 8: Schematic diagram showing modes of vortices from an elastically mounted cylinder (Williamson and Govardhan 2004, C–1)

1.3.6 Amplitude versus Reduced Velocity

An important FIM analysis tool is the amplitude ratio A^* versus reduced velocity U^* curves where the normalised peak displacement of an elastic or elastically attached circular cylinder is analysed for both averaged peak amplitudes and frequency. For 1 degree-of-freedom (DOF) cylinder motion the spanwise axis is typically free to oscillate as it has the highest amplitude (Bearman 2011, fig. 4). Figure 7 and 9a demonstrates this plot technique which illustrates multiple levels, or branches, of increased amplitudes for VIV. The study that produced the graph in figure 7 by Khalak and Williamson (1999) demonstrated a third branch of VIV at increased amplitude when low mass-damping was used linking back to the previous section and the work on damping ratios. The changes in the branches is due to two factors. The first is the FSI, pressure and viscous forces around the boundary layer responsible for the vortex shedding mode (2S,2P,2S+2P) as explained above and shown in figure 8. The second is the phase difference of the lift and drag forces which are a decreasing function of mass-damping and an increasing function of Reynolds number (Soti et al. 2018, 296–97). These plots have also been utilised to demonstrate the effect of variable damping

The degrees of freedom determine the number of lift and force vectors acting on the cylinder. In 1DOF the cylinder is restricted to movement perpendicular (transverse) to the flow while in a 2DOF the cylinder can vibrate in-line (direction of free stream) and perpendicular to the flow as visualised when plotted in a Lissajous diagram shown in figure 9b. It can clearly be seen that the amplitude is greater in the transverse direction.

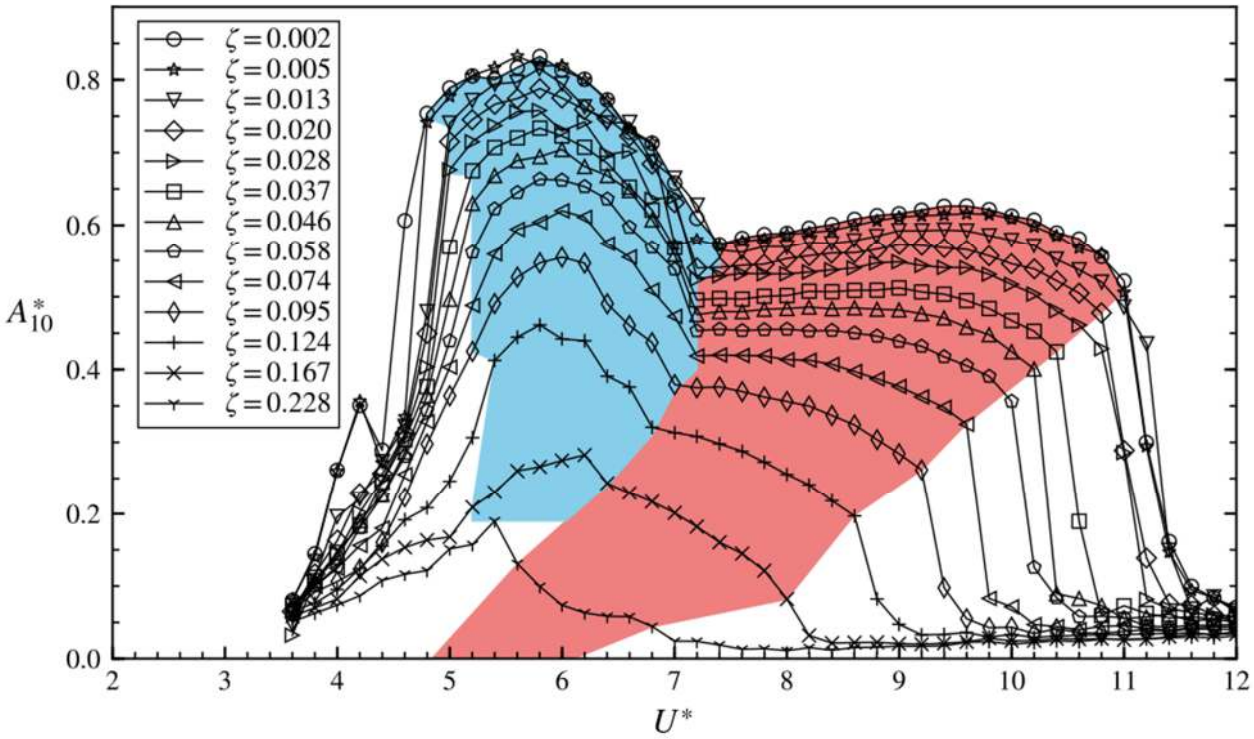

Figure 9a: Peak amplitude (top 10% max amplitude responses) vs reduced velocity for multiple damping ratios (Soti et al. 2018). 2200<Re<6661 and m*=3.0. Blue and red indicate upper and lower branches respectively. Note how the upper branch dissolves as damping increases.

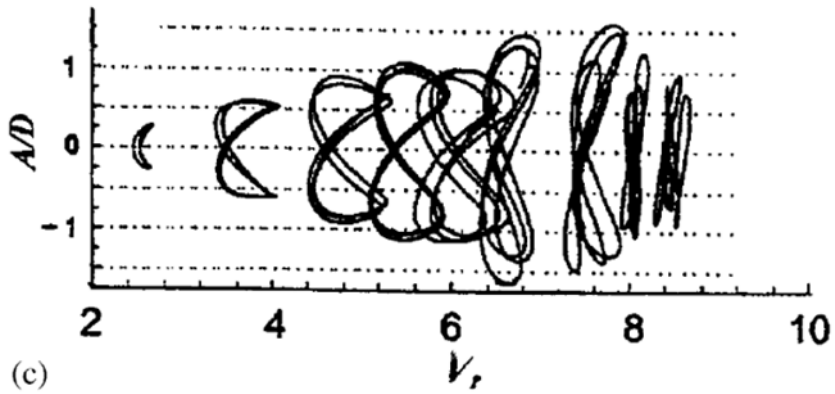

Figure 9b: 2-DOF Traces (Sarpkaya 2004)

1.3.7 Boundary Layer

The boundary layer was defined in section 1.1 and is further refined here with respect to the actions that take place in the boundary layer, to add definitions and elucidate some of the terminology through diagrams. Firstly, the boundary layer is energised by the level of surface roughness. From the fluid passing over roughened areas there is increased movement of the streamlines causing interference and energy transfer through the fluid. The effect is compounding and eventually results in movement to turbulence within the transition region of the boundary layer. Figure 2a had this detail. The coefficient of drag was shown in figure 5 for multiple shape types. Now looking specifically at the cylinder in this diagram, it is important with respect to the boundary layer because of the critical Reynolds number as described in section 1.3.1. The boundary layer separation point was also discussed in section 1.1 and illustrated in figures 2(b) and 2(c) and there is further detail below in figures 10(a) and 10(b). Figure 10(a) shows the boundary layer, shear layer and other zones in some detail for the fully turbulent case. Figure 10(b) adds some terms and describes the balance of forces creating wakes and vortices.

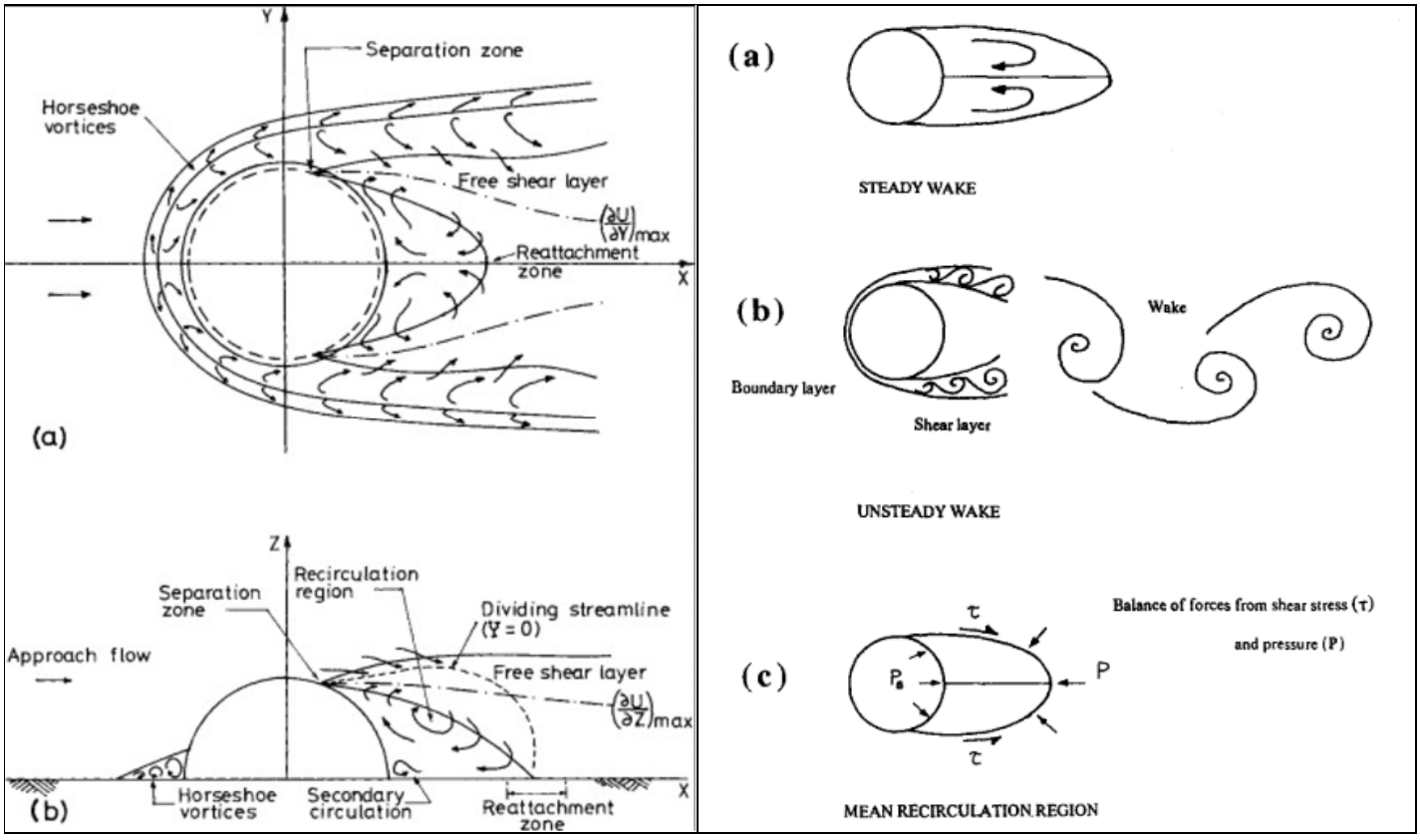

Figure 10: (a) LHS Turbulent boundary layers (Savory and Toy 1989, fig. 11)
(b) RHS Diagram of cylinder wake and layer terminology (Williamson 1996, fig. 4)

As the Reynolds number increases the separation point moves further forward from but flow in the boundary layer is still laminar. This continues up until the C_D decrease begins as the velocity of the fluid increases to a value where the boundary layer separation point begins moving rearward on the cylinder (Achenbach and Heinecke 1981). The pressure forces and viscous forces are unable to maintain the laminar flow and turbulent flow begins in the shear layer followed by reattachment resulting in an increasing value of C_D until finally turbulent separation occurs. The region between when the turbulence in the shear layer begins and when the layer becomes fully turbulent is termed the 'separation bubble'. Re_{crit}. is at the end of this phase of transition in flow characterisation where two 'separation bubbles' on either side of the cylinder (Niemann and Hölscher 1990, 198–99). The turbulent flow delays separation due to increased mixing within the boundary layer causing increased transport of momentum throughout the boundary layer thickness increasing the streamwise momentum in the boundary layer. This allows the flow to overcome the adverse pressure gradient and moving further back rapidly until the separation angle settles around 110° to 120° for a smooth cylinder (Niemann and Hölscher 1990, 198).

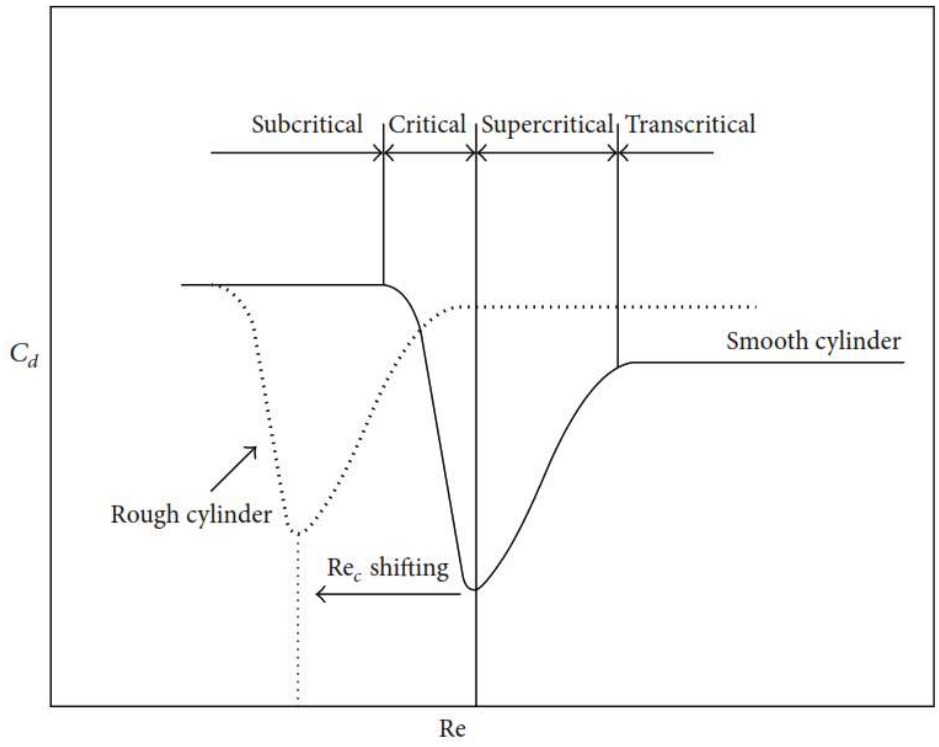

Figure 11: Definition of critical Reynolds number and the effect of rough surfaces explained later (Alonzo-García et al. 2015, fig. 1)

1.4 Computational Fluid Dynamics Terminology

Computation fluid dynamics (CFD) is a computer-based mathematical simulation technique designed to solve flow mechanics problems. It can be used across many situations including liquid flow, FSI, mass transfer, heat transfer and chemical reactions (Blazek 2015). CFD is an economic alternative to actual models or full-scale experiments for research in many scientific fields from electronics to earth sciences and has applications in medicine, industrial design, manufacturing, aerospace and chemical processing (Tu, Yeoh, and Chaoqun 2012). The simulation technique is limited in its application only by the generalisation of the models, the computing power available and the correct input and application of relevant physical and chemical properties and laws. Like most computer software output – quality of results is limited to the accuracy and quality of the data input. There are also issues associated with replicating previous research results and even reproducing results by the original authors when considerations of software upgrades, hardware upgrades and changing versions of additional applications have an influence on reliable and consistent repeatability (Mesnard and Barba 2016).

1.4.1 CFD Process

CFD pre-processing consists of stages to develop a rigorous model that will provide accurate solutions. Depending on the application there are significant differences in the way CFD solutions are implemented. The discussion that follows is only relevant to the study presented herein. The first stage is to develop a domain for the problem including deciding on two or three dimensions and the magnitudes required for the domain, in number of diameters of the cylinder to achieve the desired calculations. Some solutions require outer wall interaction with the cylinder while others, as in this case, are designed to remove any influence of the walls on the cylinder. This requires a larger domain, in the order of several diameters. The choice of domain size is a compromise between enough distance to accurately determine a solution without interference from boundary walls nor increasing significantly computational expense.

The next step in the process is to develop the mesh. The mesh defines the element placement and density impacting the accuracy of the solution and its ability to converge as these are the locations where calculations will be performed for each timestep. It is designed to provide accurate calculations for significant areas, which in this study are; the near wall of the cylinder, particularly from before the surface textures to after the separation point, and the flow

downstream of the cylinder. In accordance with the rule of the wall to be discussed shortly, a y+ value close to one is required near the cylinder wall.

The final step in pre-processing is to set boundary conditions for all walls and defining inlets and outlets. The wall options include no-slip signifying that the boundary layer turbulence will be calculated and no-shear to reduce the influence of the walls by minimising the interaction of the wall with the rest of the domain calculations. The cylinder is defined no slip while the top and bottom walls are no-shear. The inlet is the boundary on the left of the domain and the boundary on the right is the outlet.

The next steps in setting the CFD is to assign a turbulence model and a pressure velocity coupling method, validate the meshing against the model and method chosen to confirm suitability such as checking y+, lowering the mesh quality until it begins to affect results via a grid independence study and ensure the solution will converge over the total time selected. The grid independence study ensures that the most efficient use of computational resources is made.

To choose a turbulence model and pressure coupling scheme requires knowledge of the problem to be solved (ANSYS 2019a, chap. 28, 2019b, chaps. 12, 37). The turbulence model requires considerations such as the physics of the flow, the established practice for a specific class of problem, the level of accuracy required, the available computational resources and the amount of time available for the simulation The pressure velocity coupling scheme requires solution methods to solve the pressure and velocity partial differential equations. These solution sets required are a transient gradient, a pressure interpolation scheme and spatial discretization schemes for the time-dependant equations. For transient problems a time-dependent solution formulation is also required. Gradients are needed not only for constructing values of a scalar at the element faces, but also for computing secondary diffusion terms and velocity derivatives (ANSYS 2019a). Time-dependant equation requirements vary depending on the model but typically pressure, density, turbulent kinetic energy and turbulence dissipation rate can be required. Finally, for transient solutions the governing equations must be discretised in both space and time. Temporal discretisation involves the integration of every term in the differential equations over a time step.

1.4.2 Numerical Analysis by CFD

For fluid flow and FSI relevant to this research, the mathematical calculations solved are the conservation of mass and momentum. The conservation laws simply put mean that for a closed system there is no loss or gain of momentum, mass or energy unless there is an external input.

The relevant equation of mass conservation is at equation (1.5) and momentum conservation are equations (1.5.1-1.5.3) which, combined with the conservation of energy not required for this CFD study, make up the three-dimensional unsteady form of the Navier-Stokes equations. These coupled differential equations describe how velocity, pressure and density of a moving fluid are related. These include the effects of viscosity in the flow per time period. The equations include three independent spatial coordinates x, y and z; an independent time variable t; five dependant variables, pressure P, density ρ, and three components of the velocity vector u, w and z. All the dependant variables are functions of all four independent variables and therefore the equations are partial $(\partial/\partial t)$ differential equations not ordinary (d/dt) differential equations meaning that the independent variables are fixed for each independent variable being derived.

$$\frac{\partial \rho}{\partial t} + \frac{\partial(\rho u)}{\partial x} + \frac{\partial(\rho v)}{\partial y} + \frac{\partial(\rho w)}{\partial z} = 0 \tag{1.4}$$

$$\frac{\partial(\rho u)}{\partial t} + \frac{\partial(\rho u^2)}{\partial x} + \frac{\partial(\rho uv)}{\partial y} + \frac{\partial(\rho uw)}{\partial z} = -\frac{\partial P}{\partial x} + \frac{1}{Re}\left[\frac{\partial \tau_{xx}}{\partial x} + \frac{\partial \tau_{xy}}{\partial y} + \frac{\partial \tau_{xz}}{\partial z}\right] \tag{1.5.1}$$

$$\frac{\partial(\rho v)}{\partial t} + \frac{\partial(\rho uv)}{\partial x} + \frac{\partial(\rho v^2)}{\partial y} + \frac{\partial(\rho vw)}{\partial z} = -\frac{\partial P}{\partial y} + \frac{1}{Re}\left[\frac{\partial \tau_{xy}}{\partial x} + \frac{\partial \tau_{yy}}{\partial y} + \frac{\partial \tau_{yz}}{\partial z}\right] \tag{1.5.2}$$

$$\frac{\partial(\rho w)}{\partial t} + \frac{\partial(\rho uw)}{\partial x} + \frac{\partial(\rho vw)}{\partial y} + \frac{\partial(\rho w^2)}{\partial z} = -\frac{\partial P}{\partial z} + \frac{1}{Re}\left[\frac{\partial \tau_{xz}}{\partial x} + \frac{\partial \tau_{yz}}{\partial y} + \frac{\partial \tau_{zz}}{\partial z}\right] \tag{1.5.3}$$

Re is the Reynolds number, tau variables τ are the components of the stress tensors. The tau are diffusion terms whereby the stresses are carried by the random motion of the fluid. The terms on the left of the conservation of momentum equations are convection terms meaning they are related to a property occurring in the flow being moved by the ordered motion of the fluid (Glenn Research Center 2015). To solve the flow problem all four equations are solved, and the stress tensor terms are approximated using turbulence models.

To solve the numerical problem the differential equations are approximated by algebraic equations for the variables at discrete locations within the model (called elements) for each discrete time segment (called the sample time) with a pressure field. The pressure field cannot be solved from the equations directly and therefore an iterative process of adjusting the pressure until the resulting velocities meet mass requirements is required. This process is called pressure-velocity coupling and is based on a corrective term being applied to an initial pressure field value such that the velocity is driven to a value that satisfies momentum and mass conservation.

1.4.3 Mesh Quality

Considering only the 2-dimensional case there are two element types, triangles and quadrilaterals, available for meshing. Triangles are good for dynamic meshes where there will be deformation such as when there is a moving body that requires remeshing otherwise quadrilateral shapes are recommended. Each element has a centre point and three or four nodes defining the corners depending on the element shape. Each element has three or four adjoining elements. Elements make up faces with elements on the edge of faces having one less adjoining element. There can be zones within faces to allow for different meshing requirements in a zone, for example around curves there is different requirements to large rectangular shapes. At the edge of zones best practice is to have elements of similar size. There are five main components to determining element quality resulting in an overall mesh quality; skewness, orthogonal quality, element quality, aspect ratio and Jacobian ratio (ANSYS 2019c).

Skewness is the amount an element is lateral deformed or pushed sideways. An equilateral triangle pushed sideways becomes acute and then obtuse as quality drops. Values of skewness are from 0 to 1 with 0 being equilateral and ideal while 1 is unacceptable causing calculation corruption. Values below 0.25 are excellent and values below 0.5 are good. A highly skewed mesh will result in the solver being unable to converge below an acceptable level. Figure 12(a) illustrates skewness.

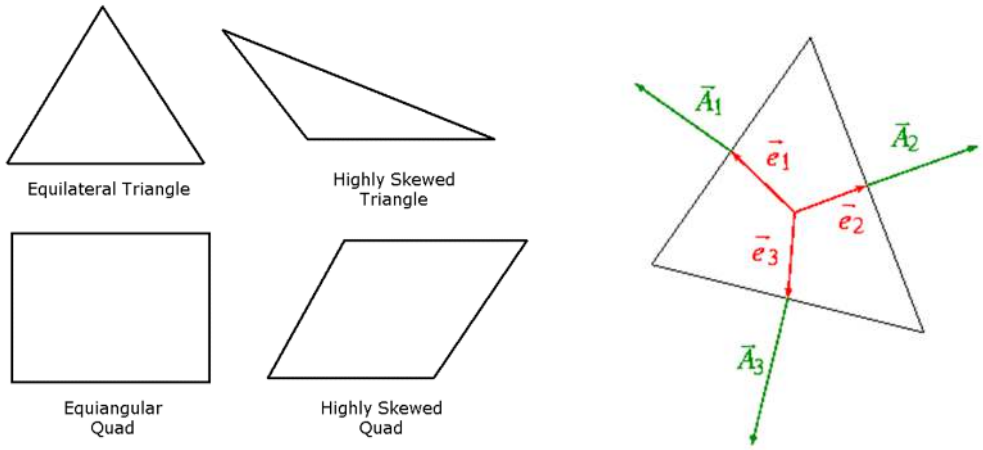

Figure 12: (a) Skewness (ANSYS 2019c, fig. 54) (b) orthogonal quality (ANSYS 2019c, fig. 58)

Orthogonal quality is a measure of the vectors between an element and its neighbouring element. The vectors are measured from the centre of the element and extend to the centre of each side and the centre of each adjoining element centre as shown in figure 12(b) for the triangle case. The closer the vectors are to being aligned the better the orthogonal quality. The value ranges from 0 (worst) to 1 (best) with any value below 0.01 needing evaluation for effect on solution quality while above 0.2 is considered acceptable.

The element quality metric is based on the ratio of the volume to the sum of the square of the edge lengths. A value of 1 indicates a perfect square/triangle while 0 means a zero or negative value.

Aspect ratio is a measure of elongation. It is calculated differently for triangles and quadrilaterals. For quadrilaterals each corner has two vectors to adjoining corners. These vectors are used to create four parallelograms, the area of each parallelogram is divided by the length of each component vector squared, to give 8 possible aspect ratios. Figure 13 makes understanding this concept easier. The minimum ratio is taken as the aspect ratio for the quad element. For triangles the ratio is between the area of triangle and the maximum edge length for each element. The values are scaled, so that an aspect ratio of 1 corresponds to a perfectly regular element, while an aspect ratio of 0 indicates that the element has zero area.

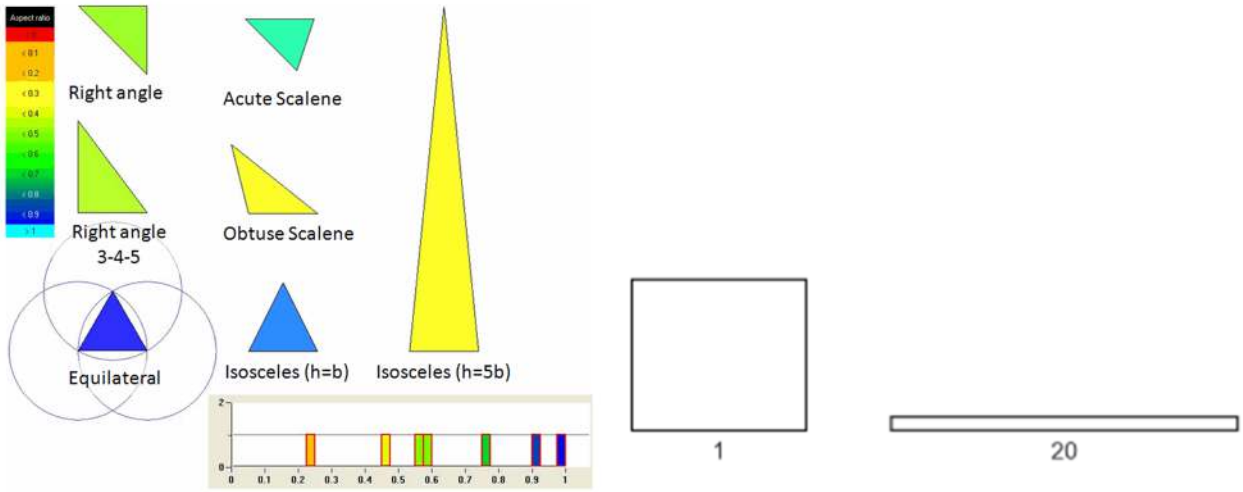

Figure 13: Aspect ratio examples for triangles (ANSYS 2016, fig. 399) and quadrilaterals (ANSYS 2019c, fig. 44)

Jacobian ratio is a measurement of the shape of a given element compared to that of an ideal element. If an element has a bad quality Jacobian ratio, the element may not map well from element space to real space, thereby making computations based on the element shape less reliable. The ideal shape of an element depends on element type and has a value of 1 as shown in figure 14. There are several different methods to calculate the Jacobian ratio and three options are provided in ANSYS. Jacobian Ratio calculated by ANSYS programming language definitions (MAPDL) is the ratio of the element is the ratio of the maximum to the minimum sampled value of R_J, while for Jacobian Ratio (Corner Nodes) and Jacobian Ratio (Gauss Points) are the ratio of the minimum to the maximum. Jacobian Ratio (MAPDL) is used in this study as it is optimised for ANYSYS and is assessed to be an erroneous -100 if the maximum and minimum have opposite signs.

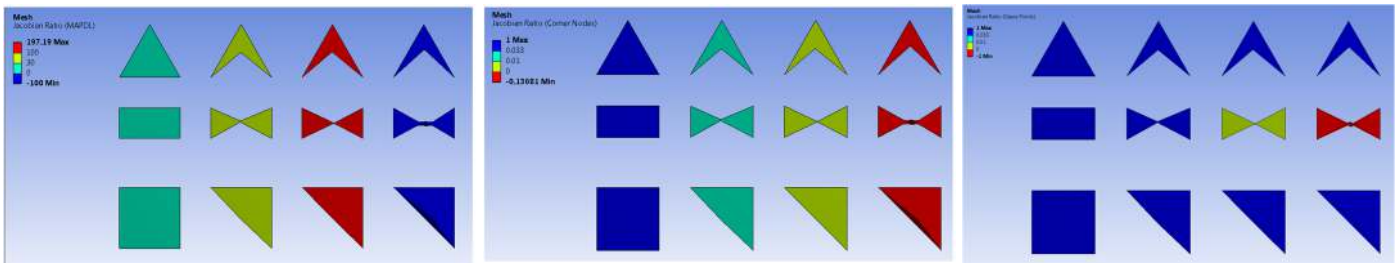

Figure 14: Jacobian Ratio Examples (ANSYS 2016, figs. 46–48)

1.4.4 Turbulence Models

Models are used to solve the turbulence stress tensors terms of the partial differential equations of fluid motion. Reynolds averaged Navier-Stokes (RANS) and unsteady RANS (URANS) are very commonly used in CFD for practical modelling applications because of their computational efficiency. They are time-averaged equations of

motion of fluid flow and are solved using the finite-volume method and closed with turbulence models. URANS is an extension of RANS where the time-dependant terms are included in the governing equations (Young and Ooi 2007, 1063). Most of the RANS use one of three models; Spalart-Allmaras (SA), k epsilon (k-ε) or k omega (k-ω) where; k is turbulence kinetic energy, ε is the rate of dissipation of turbulent kinetic energy and ω is the specific rate of dissipation of turbulent kinetic energy. SA is a one-equation model while the other two are two-equation models. They have been updated or have additional components to improve accuracy since their first introduction (Kinaci 2016). A commonly used example is the Shear Stress Transport (SST) adaption of k-ω where a hybrid is created. The k-ω model is used inside of the boundary layer and the k-ε model is used outside the boundary layer to optimise the benefits of both models meaning that SST can account for the transport of the turbulence shear stress (Menter 1994).

More advanced and computationally intensive CFD models exist including scale resolving simulations (SRS) and direct numerical simulation (DNS). Large eddy simulation (LES) is an SRS that dynamically adjusts as it calculates to remove small scale eddies and only calculates the large eddies using a high-pass filter. DNS on the other hand completes a Navier-Stokes calculation for each part of the flow and is computationally extremely demanding, typically only conducted at low Reynolds numbers with large computing resources found in universities and research facilities.

Detached eddy simulation (DES) and scale adaptive simulation (SAS) are hybrid techniques of RANS and SRS which allows reasonable computational effort with accurate results for high Reynolds number applications (Spalart et al. 2006; Shur et al. 2015). Figure 15 provides a visual comparison of the turbulence scales calculated by each model type.

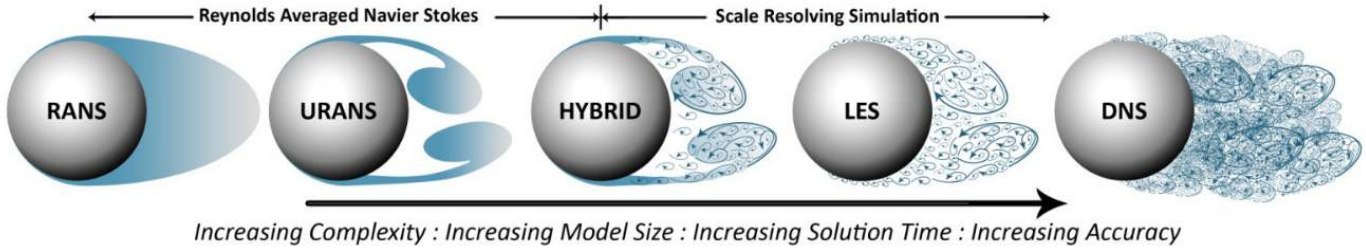

Figure 15: Comparison of different modelling approaches to turbulent spatial scales (Hart 2016, fig. 1)

1.4.5 Pressure-Velocity Couplings Methods

To solve the pressure-velocity coupling equations, numerical methods are employed. Examples used by the Fluent software include the semi-implicit method for pressure linked equations (SIMPLE), a variation of SIMPLE that corrects for significant velocity at each iteration and pressure implicit with splitting operations (PISO). The SIMPLE process considers a two-dimensional laminar steady flow equation in Cartesian coordinates with initial values of the pressure field, either from operator input or modelling based on standard variables. The process for SIMPLE after selection of the initial values is as follows: momentum equations are solved to get velocity terms; coefficients and source terms for the pressure correction equation are calculated; pressure corrections are solved; velocity corrections are calculated; finally pressure and velocity values are update and then the process repeats until a solution has converged. By converged, it means the residual is calculated and below a set threshold considered acceptable to meet solution requirements. The residual is the quantifiable value of the error in the calculation. The normal standard is for the residual to be three significant figures less than the original value (ANSYS 2019a, chap. 37.21). The PISO scheme is very similar to SIMPLE however there are two correction steps used with the aim of reducing the time to get a solution (ANSYS 2019a, chap. 28.4.3).

1.4.6 The Law of the Wall and y+

Turbulence models vary in the complexity of the numerical simulation especially in the area of the boundary layer. To model the velocities and other terms near the wall the y+ term is calculated. y+ (equation 1.6) is a value to define the distance from wall of the first element, made dimensionless with the shear velocity u_τ and kinematic viscosity υ.

$$y^+ = \frac{u_\tau \Delta y}{\upsilon} \tag{1.6}$$

where

$$u_\tau = \sqrt{\frac{\tau_w}{\rho}} \tag{1.6.1}$$

$$\tau_w = \mu \left(\frac{\partial u}{\partial y}\right)_{y=0} \tag{1.6.3}$$

$$\upsilon = \frac{\mu}{\rho} \tag{1.6.4}$$

with the terms τ_w being wall shear stress, ρ density, Δy the height of the first cell next to the wall, μ the dynamic viscosity and U the free stream fluid velocity. u^+ is a dimensionless velocity term equal to the fluid velocity parallel to the wall as a function of the cell height $\left(\frac{\partial u}{\partial y}\right)_{y=0}$ divided by the shear velocity u_τ.

The law of the wall is shown in figure 16 and is useful for CFD as it facilitates what size the first cell height of the mesh needs to be such that the boundary layer turbulence is modelled correctly (Salim and Cheah 2009). Examples are the k-ε model which requires a 30>y+>70 in the log-law region while the k-ω and SST models require y+<5 but preferably y+ approximately 1 in the viscous sub-layer. The SA model is suitable for use in either the log-law region or the viscous sub-layer. No model should have a y+ in the buffer zone for an accurate result.

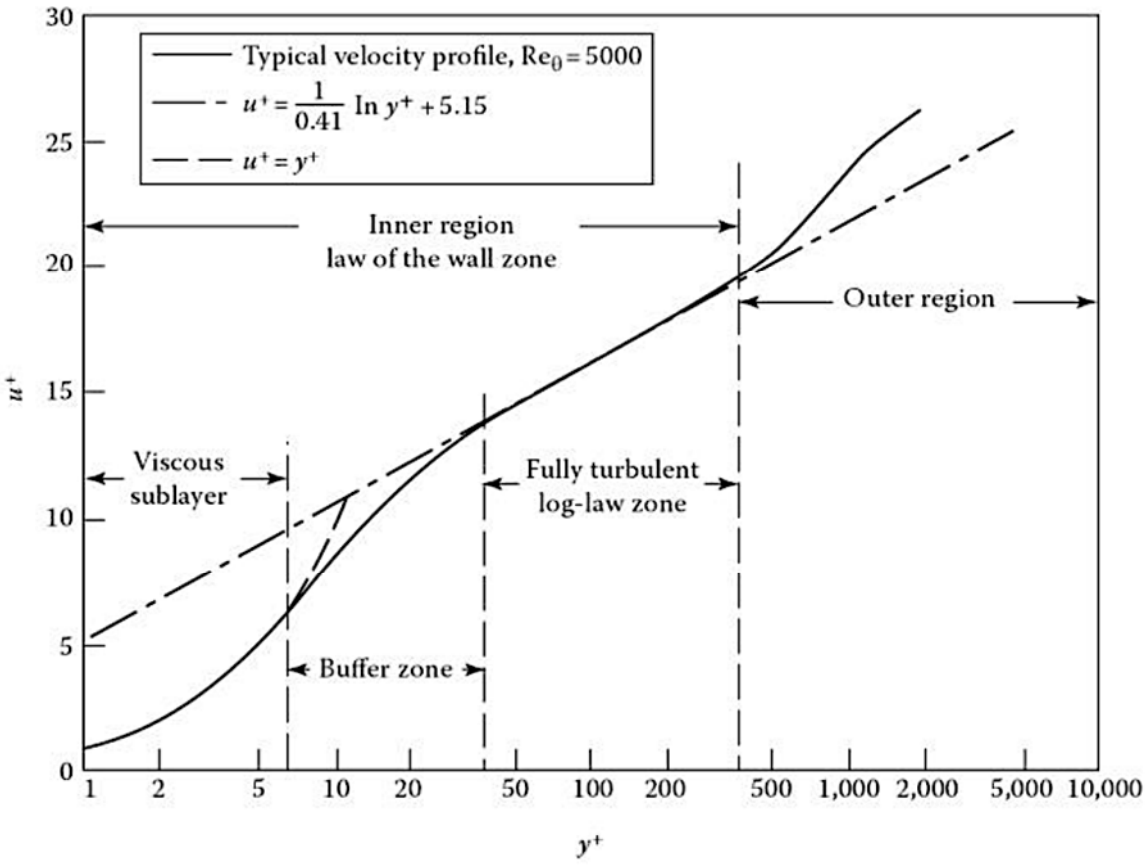

Figure 16: The Law of the Wall Figure (Pletcher, Anderson, and Tannehill 1984, 224)

2 Literature Review

As discussed, the conditions of FIM around a fixed cylinder are complex but reasonably well understood for low Reynolds numbers. FIM at higher Reynolds numbers is an active area of research however, consideration of issues and solutions for the marine environment is more limited; mainly considering engineering of suppressive techniques. Looking at research specifically for FIMEG development, there is limited content in the open literature. The following literature review covers the areas of FIMEG technology; surface texturing research for circular cylinders including rough surfaces, dimples and troughs; marine fouling and issues for rough surfaces and finally the implementation of CFD with respect to surface texturing.

2.1 FIMEG Technologies

FIMEG have been developed for study in universities and laboratories by countries including the United States, Korea, Japan, Switzerland, Spain, China and India. The fluid chosen is typically air or water as these present the most likely scenario for renewable energy sources. The most advanced system to date for water is the VHE VIVACE system first developed at the University of Michigan (Raghavan 2007; Bernitsas and Raghavan 2008) and now in commercial development. For air the Vortex Bladeless aeroelastic wind generator (Villarreal 2018) is in prototype testing. To inform context within the rest of this paper, VIVACE technology is detailed, and its strengths and weaknesses identified below.

VIVACE is a hydrokinetic power generating device designed initially in a laboratory at the University of Michigan and has expanded to a development company VHE currently trialling full-scale commercial models. The current design is modular and consist of four vertical circular tubes connected to a frame with internal linear generator. VIVACE successfully generates power in water velocities equivalent to the marine environment (i.e. $2.0x10^4<Re<2.0x10^5$) by using VIV and galloping. It was found that, referring to figure 7, the upper branch of VIV was accessible for VIVACE at relevant Reynolds numbers (Raghavan and Bernitsas 2011). In addition studies show that by using a technique called passive turbulence control (PTC), increased amplitudes were available by transitioning to galloping (Ding et al. 2016; Chang, Kumar, and Bernitsas 2011). Passive turbulence control consists of roughened surface strips of a specific height placed at specific angles from the front stagnation point. The PTC

increase the turbulent kinetic energy of the fluid in the boundary layer which has consequences for the FIM behaviour due to changes in the separation point. This will be discussed in detail.

Transverse FIM moves the cylinder and translate the kinetic energy of the water to electrical energy in the linear generator. The linear generator is a fixed long cylindrical stator with a ferromagnetic core and permanent magnets surrounded in part by a smaller translator (equivalent to a rotator) that moves across the stator by a direct connection to the cylinders. At the ends of the coil core there are electromagnets that non-linearly repel the approaching translator allowing the reversal in the direction of the cylinder and therefore continuous motion. Figure 17 shows a pictorial representation of VIVACE before it was converted to a vertical cylinder system.

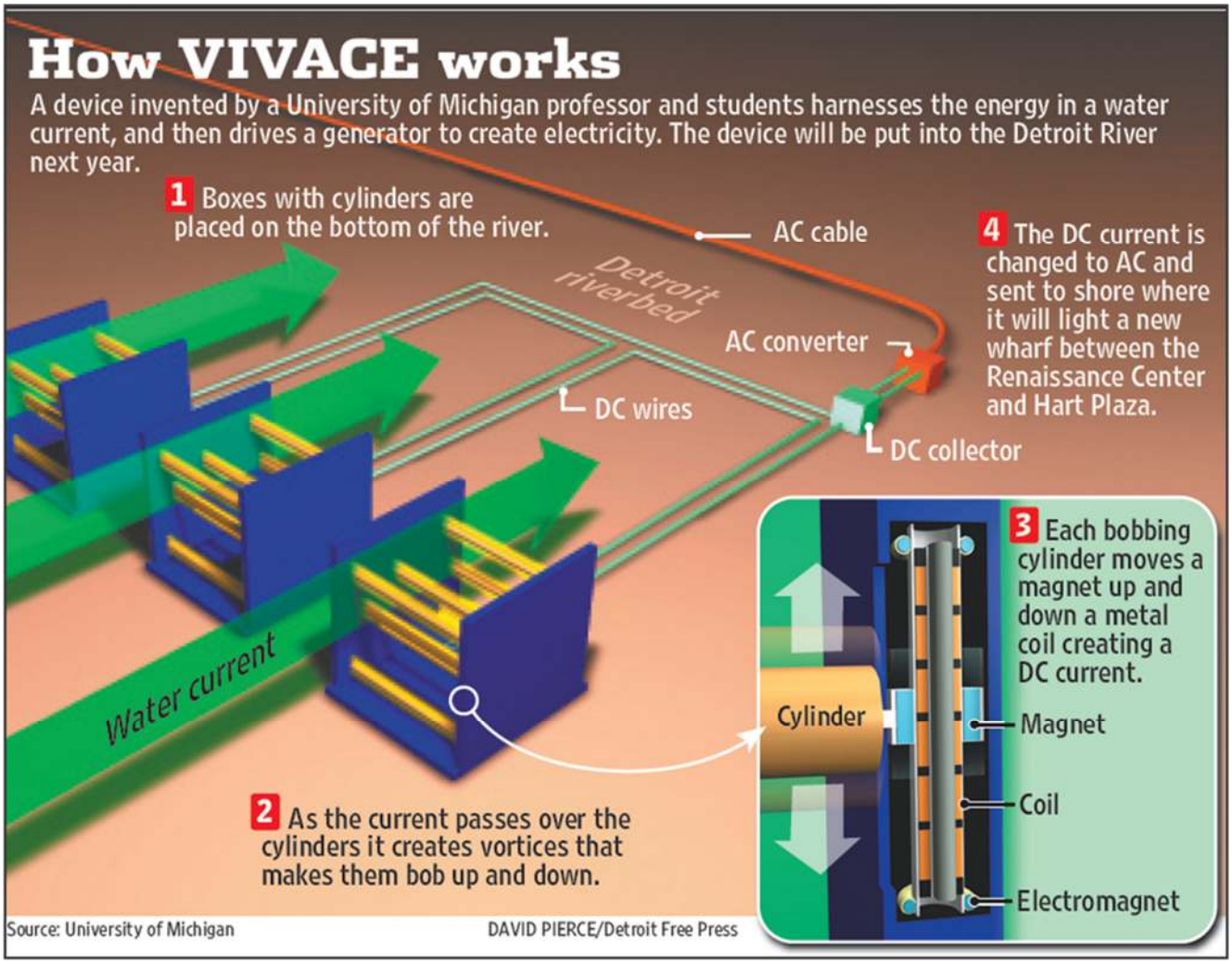

Figure 17: Pictorial representation of Vortex Hydro Energy (Vortex Hydro Energy 2019)

The advantage VIVACE has had in the development process through the University of Michigan is twofold; firstly the ability to conduct ongoing research and development enabled by access to world class facilities such as the Marine

Renewable Energy Laboratory (MRELab) which houses the low turbulence free surface water channel and a towing tank (University of Michigan 2019) and secondly, ongoing funding through the start-up company VHE.

The benefits of ongoing development have resulted in the VIVACE having the following characteristics (Lee and Bernitsas 2011):

- High energy density,
- Scalable and relocatable (with appropriate but common maritime vessels) implying also that it will be easy to extract for maintenance pending water depth,
- Reconfigurable for expected water velocities in different locations and marine environments,
- Operation in water velocities down to 1 knot by use of multiple horizontal cylinders biomimicking the efficiencies gained by schools of fish,
- Little to no effect on marine life due to relatively slow movement of the horizontal cylinders, and
- Simple power take-off mechanism via linear generators.

VIVACE is the most advanced and tested FIM energy generation device however there are also potential areas for design improvement that have not been considered in the open literature:

- The device is fixed in the water flow so it will need to be placed for optimised flow velocity within the river/ocean. As opposed to figure 17, the latest version of VIVACE has vertical cylinders allowing for greater direction variation of the incoming flow however ultimately if the flow direction changes the fixed placement of the PTC will decrease effectiveness.
- VIVACE only uses transverse 1DOF motion. While transverse motion produces higher amplitudes than inline motion as per figure 9b the use of only transverse motion for energy production means that the energy available in the inline motion is lost. Further research is required to determine if utilisation of inline motion detracts from transverse motion and the ultimate exergy equation.
- Fouling in the marine environment could have three significant impacts on the VIVACE system. In particular, the PTC and its roughness may increase the likelihood of marine fouling resulting in the following:

- Changing the PTC behaviour

- Affecting the shape of the cylinder

- Changing the values of two important ratios, the mass ratio and damping ratio.

2.2 Surface Roughness

Nomenclature to describe roughness and later indentations is formalised for this paper as follows. Protrusions and indentations when considered as a collective of surface alterations are termed textures. When considering a specific texture, the name of the texture such as roughness will be used. Definitions of roughness is a random vertical feature with and average height above the surface. A dimple is defined as an indentation made by part of a sphere inlaid into the surface. A strip is defined as a spanwise section of texture of specified width starting at a specific angle around the cylinder from the front stagnation point. A channel is defined as a rounded indentation spanwise along the cylinder. Indentations or protrusions of other shapes or characteristics will be defined when used. Averaged roughness height or the largest value of indentation depth are defined as texture height, k_d and are relative to the regular surface level. The diameter of the cylinder is D, the diameter of a circular textures is d with the diameter of a sphere that would make a dimple is $\overline{d}$. Depth of the boundary layer at the leading edge of textures is δ_0 called dimple alpha. These terms result in a number of ratios that will be used to compare studies and results; k_d/D which will be used as the standard where possible in this paper, k_d/d , δ_0/d and d/D.

To this point smooth circular cylinders have been discussed. Surface roughness is considered because of its effect on the characteristics of FIM due to changes in the boundary layer behaviour. It is relevant because it is used to alter FIM motion in VIVACE and because it can be expected to become an issue for devices in the marine environment due to biofouling explained later in the literature review. At Reynolds numbers up to 200 there is negligible effect of increasing the surface roughness (Zdravkovich 1990, 59). The first noticeable effect of surface roughness is a change in the shear layer characteristics of increased turbulence and altered vortices. These are caused by increases in the turbulence levels inside the boundary layer bringing forward the transition from laminar to turbulent phase, as described in section 1.1 and figure 2a, on the cylinder surface. With increasing roughness or Reynolds number the

effect is the reduction or completely disappearance of transition regimes that are seen for smooth cylinders as characterised in table 3 (Zdravkovich 1990, 59, 61).

2.2.1 Complete Roughness Cover

Early studies concerning roughness considered completely covered cylinders to evaluate the effects on drag coefficients and Reynolds numbers. Some studies were specifically interested in the critical Reynolds number region. Park (2012, 10–11) summarises the studies succinctly for $2.5\text{x}10^{-3} < k_d/D < 3.03\text{x}10^{-3}$ while Zeonoddini et al (2016, 380–82) give a good summary overall. The main outcomes relevant for this study, in the TrSL3 region, are considerations of roughness thickness total height and position on the cylinder. The boundary layer thickness and its associated energy level is related to the overall height of the roughness with increased k_d increasing energy levels due to increased turbulence. Otherwise up until the transition to a fully turbulent boundary layer the surface roughness has minimal effect. The drag coefficient is almost constant up to the area around the critical Reynolds number, as for the smooth cylinder although there may be slightly varied. Because of the increased energy levels within the boundary layer the transition to a fully developed turbulent boundary layer occurs earlier than the smooth cylinder equivalent. As a consequence there is a rapid decrease in C_D towards the critical Reynolds number that is also typically a higher value than the smooth cylinder as the single bubble turbulent boundary layer is completed quickly and C_D recovers to close to previous levels. The early decrease in C_D does not cause the vortex shedding to abate however as long as k_d/D>0.01 (Zdravkovich 1990, 59). It was also found that as roughness height increased these changes became more pronounced.

2.2.2 Localised Roughness

Local strips of roughness spanwise across a circular cylinder has also been studied. There are several parameters that can be changed and studied when considering localised surface roughness namely; the position of the roughness strip $\alpha_{r,n}$, the number of roughness strips n, the angle over which the roughness strips cover θ_n , the angle of the roughness strip on the cylinder relative to the incoming fluid flow $\theta_{n,s}$, the depth of the roughness k_d and if it varies over n or θ_n etc. Teverovskii (1968) considered the position of the roughness and different roughness sizes. It was found that roughness positioned behind the smooth cylinder equivalent separation point (SCESP) had little effect while roughness before the SCESP increased the Strouhal frequency because of the increased energy in the boundary layer.

Results varied for roughness in and around the SCESP depending on the surface roughness height. Roughness about the size of the boundary layer had a similar impact on energy in the boundary layer as roughness in front of the SCESP increasing the Strouhal frequency while roughness larger than the boundary layer decreased the Strouhal frequency because the boundary layer was completely separated from the cylinder.

2.2.3 Passive Turbulence Control

MRELab has been conducting studies into local roughness for the VIVACE in order to enhance the amplitude of FIM with the aim of increasing power output in the TrSL3 range of Reynolds numbers. Chang (2011) conducted studies using passive turbulence control (PTC) strips selectively placed onto the VIVACE rigid cylinders to experimentally investigate flow separation and effects on the boundary layer. This was designed to show induced higher vorticity and therefore lift. The results of the experiments showed maximum amplitudes of 3D during galloping which is the physical limit of the VIVACE system suggesting higher amplitude are possible. For strip placement $\alpha_{r,1}$ from 20° to 64° the amplitude was reduced in VIV but initiated and continually increased during galloping. The frequency ratio increased for VIV and decreased for galloping. Strip placement was a factor for complete suppression of FIM below 10° and around 64°. Strip roughness height k_d, which was in the order of the thickness of the boundary layer, did not significantly affect amplitude or frequency ratio however it initiated earlier galloping. For strip width θ_1, it was found that increasing $\theta_1$led to decreased VIV amplitudes and increased galloping amplitudes for $8° < \theta_1 < 24°$. In the range $24° < \theta_1 < 32°$ increasing suppression of all FIM modes was observed until FIM ceased completely, like the behaviour observed for whole cylinder roughness coverage. Strip width was not found to affect the frequency ratio.

Park (2012; 2013) completed a PhD on mapping the regions where different FIM are suppressed or enhanced due to selective placement of PTC strips and further reported the application of these results for VIVACE. The conclusion was that location, height and width of the PTC all played an important role in the outcome however, location around the cylinder was the most significant. The FIM amplitude from PTC was enhanced in all galloping while VIV was suppressed compared to smooth cylinders. There was no mode where VIV and galloping co-exists and the extent of the region between VIV and galloping FIM and the consequential amplitude reduction therein depends on the strip placement. Galloping modes were dependant on whether the galloping was self-initiated by the FIM or required an

external input. The PTC-to-FIM map described what FIM was produced depending on PTC placement and there were multiple maps for varying PTC heights.

Work by Sun and Kim (2016), Ding (2016) and Park (2016) at MRELab further developed the relationship between PTC and FIM. Park determined a further refinement for location of the PTC on VIVACE and the effects on VIV specifically creating three zones of suppression, two weak and one strong (greater than 30% amplitude reduction) depending on placement. Sun and Kim where able to use the PTC findings to study optimisation of energy conversion. This resulted in the VIVACE system being able to capture useful energy at water flows down to approximately 0.4 m/s (0.78 knots) with no upper limit other than the physical limitations of the device. By adjusting other parameters within the system such as spring stiffness the transition gap between VIV and galloping was reduced significantly and still resulted in useful amplitudes. Power and efficiency curves were produced, and they are both a factor of Reynolds number but do not have equivalent maxima positions. VIV is more efficient, while galloping produces more power. It was determined that by adjusting parameters and device configuration it was possible to optimise the system to local conditions. Ding contributed to further understanding of PTC and FIM by conducting a comparison between PTC simulated in CFD and experimental results. Ding also studied the effect of PTC on the known issue of CFD incorrectly simulating the boundary layer separation point of smooth cylinder for Re>10,000 when using 2D URANS turbulence models with $30 < y^+ < 70$ (Wu, Bernitsas, and Maki 2014). The PTC removed this issue because the separation point is determined by the roughness and 2D URANS was able to accurately simulate the boundary layer.

Zhang and Sun (2018) conducted experiments accompanied with CFD simulation of PTC where the roughness was placed asymmetrically. The findings were compared with results for smooth cylinders and cylinders with symmetrical PTC with two aims. The first was to determine if amplitude and resultant power of FIM could be increased by asymmetrical roughness and secondly, evaluate the CFD accuracy with respect to boundary layer separation points for smooth and roughed cylinders in the same conditions. The findings were that in VIV, smooth cylinders produced the largest amplitude while double sided PTC produced the smallest amplitude. For galloping the symmetric PTC produced the largest amplitude and VIV the smallest. Single sided PTC produced asymmetrical amplitudes about the equilibrium point, with larger amplitudes on the smooth side for both VIV and galloping. The single sided PTC

produced higher amplitudes in the transition between VIV and galloping than both the other setups. The CFD simulated the boundary layer separation correctly for the PTC side but incorrectly for the smooth side.

2.3 Dimples and Channels

Instead of a protrusion above the surface there have been studies to investigate the effect on boundary layers from depressions on solid surfaces. One of the first studies to investigate dimples on a circular cylinder and still the most quoted in the literature review is the study of airflow around a fixed circular cylinder by Bearman and Harvey (1993). The experiment was for a $k_d/D = 9.1\text{x}10^{-3}$ for $2\text{x}10^4 < Re < 3\text{x}10^5$. The results of the experiment were to show that dimples presented an earlier critical Reynolds number like roughened cylinders except they created a greater fall in C_D and the recovery post drop was not as great but of a greater amount than for a sphere.

Ligrani et al (2001) investigated the flow structure of air over a pattern of circular depressions on a flat plate using flow visualisation from smoke. They used $6\text{x}10^2 < Re < 1.1\text{x}10^4$ and $k_d/d = 0.2$. They found that primary vortex pairs are tripped by the dimples beginning at the centre of the dimple and that after the creation of the first vortex an inflow into the dimple cavity occurred and that a secondary vortex pair was created closer to the dimpled surface. Having multiple dimple rows caused the elliptical shape of the vortices to become unsteady in height and intensity.

The effect of a dimple edge shape was investigated by passing air over a flat plate with rows of dimples (Mitsudharmadi, Tay, and Tsai 2009). It was found that the edge type did not play a significant role in the resulting flow for $k_d/d \geq 8\%$ and for values less than this there is no flow separation. The results of the deeper dimples are an increase in mean sheer stress in the region of the dimple and flow divergence from just in front of the dimple leading edge to just past the trailing edge where it converges, and flow reattaches. Although the flow for the shallow dimples did not separate there was complex behaviour of the boundary layer reported and a reduction of the dimple depth to below a k_d/d value of 4% is required to investigate if this complex behaviour will achieve significant results for circular cylinder FIM but is outside the scope of this dissertation.

The shape of grooves was varied to determine any influence on flow characteristics of a circular cylinder in air (Yamagishi and Oki 2004). Triangular grooves versus cylindrical grooves were measured and parameters of drag, pressure, turbulence and separation point were examined experimentally and via CFD. Interesting findings were that

the shape effects the final separation point of the boundary layer even though the difference between the two shapes is quite subtle, they were in the same position on the cylinder from the front stagnation point and they had the same $k_d/D = 1.458x10^{-2}$ at $1x10^4 < Re < 1x10^5$. Results of significance include greater pressure distribution and significantly later separation of the boundary layer from triangular groves. The circular grooves had greater reversal flow inside the groove resulting in greater turbulent kinetic energy.

Evenly distributed dimple patterns with varying k_d/d, area ratio and shapes were examined for different circumstances, being high speed low load versus low speed high load, to understand micro-hydrodynamic effects (Yu, Huang, and Wang 2013). The result of analysing research by different researchers revealed that for low speed high load conditions shallow and simple dimples with higher area ratio have a higher friction reduction effect than those designed on hydrodynamic pressure generation.

Flow over a patterned surface was studied by passing air over a circular metal sheet (Butt, Jehring, and Egbers 2014). The patterns were hexagonal, and comparisons were made between the leading edge of the hexagonal shape being a point (P) or an edge (E). The hexagonal shapes were indented or protruding outwards by $k_d/D = 1.98x10^{-2}$ for $3.14x10^4 \leq Re \leq 2.77x10^5$. Drag coefficients and changes in mean velocity behind the cylinder were measured. A separation and reattachment along with a downstream shift of final separation point was identified for all configurations due to an increase in the turbulent intensity of the flow near the surface. The patterns with protruding shapes were found to have the largest effects on reducing drag coefficients while indented shapes were close to smooth surface results. Further the hexagonal shape caused the separation points to be zigzag along the spanwise length of the cylinder.

One of the latest indentation studies is the measurement of drag and lift coefficients from dimpled cylinders in water and comparing the results for variation by dimple coverage and orientation (B. Zhou et al. 2015). The variation of coverage was conducted by using a cylinder that was fully or half covered with dimples. The dimple coverage factor was also varied with two levels of equally spaced dimples varied by the number of dimples around the circumference of 16 or 32. Other parameters of the experiment were $k_d/D = 0.05$ and $7.43x10^3 < \text{Re} < 1.798x10^4$. The final variation of the experiment was the orientation of the cylinder with respect to the front stagnation point being the rotated through 90°, 180° and 270° for the half-covered cylinders. Results from the tank testing did not give any

definitive results other than general agreement that dimples in the flow cause a decrease in $C_D$and C_L except for an outlier that wasn't explained. The cylinder with dense dimples over half the cylinder rotated through 270° degrees such that it had a smooth half of the cylinder was facing the free stream had a higher C_D than of the smooth cylinder while the same cylinder orientation with half the dimple coverage factor was consistently below the smooth cylinder. It is possible that the half dimple that would have been near the top and bottom of the cylinder in this case was causing increased drag because of turbulence about the leading edge or due to energizing of the boundary layer however further research is required that is beyond the scope of this paper.

2.4 Marine Biofouling

Marine biofouling is defined as an undesirable action by marine organisms and their by-products to attach themselves to marine structures, interfering with the original design of the device and ultimately affecting its efficiency (Nir and Reches, n.d.). The issue of marine biofouling is covered in a plethora of studies particularly regarding shipping and its effects on efficiency and marine structures and its effect on fluid forces and engineering issues such as inspections (Demirel et al. 2017; Schultz 2007; Owen et al. 2018). Anti-fouling techniques also receive much attention in the literature regarding coatings and treatments for the prevention or removal of marine biofouling (Berntsson et al. 2000; Gittens et al. 2013; Nurioglu, Esteves, and De With 2015). For this study, the relevance of marine biofouling is to the action of FSI about circular cylinders modified with localised roughness, and the effect of changes in the topology of the cylinder surface. Zeinoddini et al. (2016, 2017) and Jadidi et al (2018) have studied the effects of marine fouling on VIV in some detail using a towing tank and artificial marine organisms. The research has included aspects of size, shape, separation spacing and aggregation. The conclusion of their research is that marine biofouling causes a significant reduction on VIV amplitude and lift force with the effect being due to (in reducing order of magnitude) coverage ratio, aggregation, flow incidence and shape.

Marco-scale biofouling is generally proceeded by micro-scale biofouling and so the size of roughness applicable to localised roughness for FIM is directly related to micro-organism colonisation (Nurioglu, Esteves, and De With 2015, 6558). Current research into non-toxic antibiofouling (AF) and fouling-release (FR) coatings suggest the combination of two techniques will become prevalent (Nir and Reches, n.d.; Nurioglu, Esteves, and De With 2015). The first is the use of biopolymers for the AF/FR of proteins at the cellular level and is not relevant to this research. The second is surface texturing size and spacing for the AF/FR of settling spores. The sizes suggested are in the range of 2

micrometres which is relevant for the scale of the roughness of the PTC with average grit height of 260 micrometres. The issue is that the relatively large roughness of the PTC creates valleys that, even with a thin film deposition of micrometres thick material, provides significant areas for spores to settle which will ultimately lead to mass colonisation and reduction in effectiveness of the roughness.

The use of thin film electrodeposition as an anti-biofouling technique for micro-organisms has been successfully conducted using many techniques. Tungsten oxides (TO) via an electrochemical deposition technique, in particular, has properties of excellent adhesion to metal surfaces, operates under high stress and pressure environments and has exceptional robustness as well as providing anti corrosive properties while being non-toxic (Tesler et al. 2015, 8). The omniphobic slippery liquid-infused porous surface TO (TO-SLIPS) films almost completely repel the absorption of organic molecules on the surface when in motion due to interfacial tension is enough to prevent initiation and delaminate existing biofilm (Tesler et al. 2015, 7) and is suggested as the AF/FR technique for FIMEG.

2.5 Computational Fluid Dynamics (CFD) for Surface Texturing

Effects of dimples on laminar boundary layers are investigated in the first of three DNS studies by Beratlis et al (2014). Two and eight rows of dimples are investigated in laminar flow with a 'dimple Reynolds number' of $Re_\delta = 1x10^3$ where $Re_\delta = U\delta_0/\upsilon$, and δ_0 is the boundary layer thickness at the leading edge of the surface texture. The depth to diameter ratio k_d/d = 0.1 and the boundary layer thickness is half the dimple depth. The paper reviews the results of previous experiments with respect to spheres in a fluid and the relationship of Reynolds number to the coefficient of drag. Indentations and protrusions both have the same effect on the critical Reynolds number which is to increase the minimum C_d and decrease Re_{crit}. Beratlis et al (2014, 612) state that regarding surface texture studies " indicate that the turbulent boundary layer like flow, induced by sand-grain roughness is different from the one generated by the dimples". They go on to explain that the dimples generate turbulence by shear layer instability while sand-grain roughness follows a more general rule of turbulent flow from boundary layer transition over a wall, although the mechanisms for surface texturing induced turbulence are not well understood. Multiple rows of dimples are shown to create a continuous cloud of turbulence if the dimples continue which enhances boundary layer thickness. The increased turbulence increases the momentum of the boundary layer such that it extends beyond the cessation of the dimples as compared to a couple of rows only.

Quantitative differences in boundary layer thickness, boundary layer stability and shift of separation point exist for groves versus dimples (both circular and hexagonal) for fluid flow over a flat plate in the second study (Beratlis et al. 2016). The effects of the dimples and groove are clearly demonstrated via high resolution simulation images where thin spanwise turbulence is formed approximately $2/3$d from the leading edge and rises in height between 0.2d for the groove and 2d for the circular dimple. These spanwise turbulence areas are carried streamwise by complex patterns of fluid that eventually become hairpin like vortices. The instability is continuous along the span for the groove while for the dimples the instability is intermittent along the span. The study also demonstrates the difference in turbulence values with respect to dimple alpha and dimple Reynolds number by plotting skin friction coefficients downstream of a groove demonstrating that both factors are vital to turbulent flow generation.

The third paper in the Beratlis et al (2018) series develops further the concept of smooth, dimpled and roughened surfaces using DNS but now considers underlying curved surfaces. The authors note that studies to date for surface textures such as dimples on curved surfaces were lacking in the literature. Direct comparisons with flat surfaces coefficient of drag behaviour over various Reynolds numbers were difficult due to the differences in the pressure-velocity relationships around spheres and this is also relevant to discussions of flow around circular cylinders. It is suggested that experiments and results to date can be used as guides only. Findings of the study show that for a curved roughened surface the drag coefficient follows a similar shape to a smooth surface however the decrease occurs at a lower Reynolds number and is not as intense. The mechanism for transition to turbulence and flow separation is at the stagnation point of the roughness and forms a shear layer that is highly three dimensional and unstable moving around the roughness and eventually forming into hairpin streamwise structures. For dimples the drag coefficient reaches a minimum and stays close to that value as the Reynolds number increases. The mechanism for turbulence and separation is the interaction of the flow with the turbulence initiated inside the depression called 'recirculation bubbles' occurring at the second dimple with flow remaining attached over the first dimple. These results for dimples are similar to the experimental findings for golf balls and sand-grain roughness (Beratlis, Balaras, and Squires 2018, fig. 1).

A paper that informs CFD choice is a study that compares CFD turbulence models for flow over curved surfaces using URANS, SRS and hybrids such as DES compares (Hart 2016). The simulations relate to golf balls at $1\text{x}10^4 < Re < 1.15\text{x}10^5$ with dimple $k_d/D = 9.58\text{x}10^{-2}$. The research compares turbulence models suited for simulating

separating flows based on dimples. All CFD models studied in the paper except LES, being a full SRS model, use or incorporate the underlying k-ω SST model. The CFD models are compared with experimental data of drag coefficient versus Reynolds number and found to be generally in agreement, as per figure 18. All the models were found to resolve the dimple shear layer structure when correctly meshed in consideration of y+ and mesh quality. The URANS model failed to predict the small-scale structures and did not demonstrate the periodic shedding. The models that were superior were the hybrid models of scale adaptive simulation (SAS) and delayed DES (DDES).

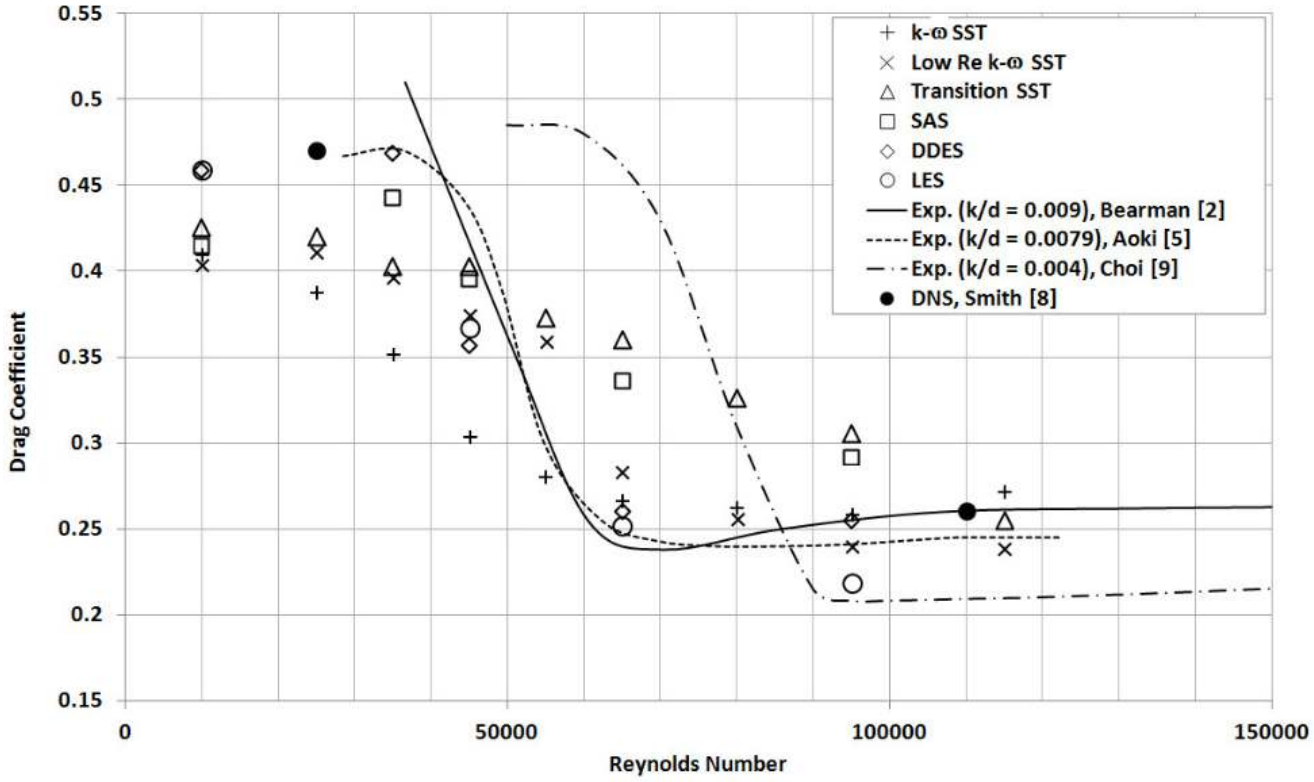

Figure 18: Comparison of CFD turbulence models for spheres versus experimental data

3 Model Design and CFD Setup

The aim of this section is to detail the model designs of the PTC cylinder and the indented alternatives, explain CFD optimisation methods and explain the CFD setup. PTC and dimple design parameters and images are provided herein to give context to the differences with the models. Explanation of the CFD model and method choices and option selections is included. Section 4 will cover the comparison between CFD simulation results for this study with the literature. The rational for dimple design is included in section 5 with the CFD results for indentations.

This study is conducted using ANSYS Workbench Academic Student 2019 R1 which consists of many modules including those related to fluid dynamics. The modules used in this study are 'DesignModeler' for domain design, 'Mesh' for meshing, 'Fluent' for CFD setup and solutions and 'Results' for post processing display. The academic version had a limit on the number of elements in a mesh to 512,000 limiting the y+<5 mesh design to a two-dimension model only. All calculations are completed on a Metabox P750DM-2G using up to 8 parallel processing cores.

The fluid domain design in figure 19 is chosen to allow a direct comparison with the PTC analysis of Ding et al (2016) as are the simulation physical properties of density, free stream velocity and viscosity at table 4. The details of the PTC are also the same as per the configuration in Ding et al. The dimple analysis consists of five test configurations D1-D5 detailed explicitly in table 4 but a general definition is as follows (all angles from the front stagnation point); D1 is five dimples of the same depth for 20°-60°, D2 is three dimples of varying depth from 20°-43°, D3 is one dimple at 55° and finally D4 is one dimple at 15°.

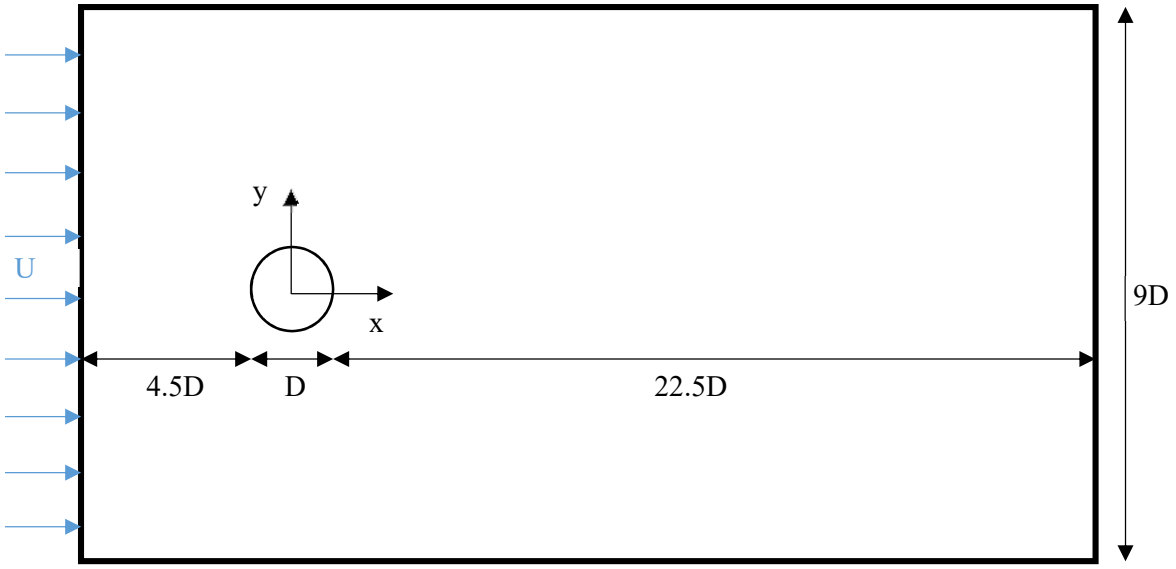

Figure 19: Model Domain Design

Table 4: Model physical properties (Ding et al. 2016, 1248–49)

Diameter of circular cylinder D	mm	88.9
Dimples (D1)		
Indentation placement angle	$degrees$	20
Angular coverage	$degrees$	40
Dimple depth k_d	mm	0.5378
Dimple diameter d	mm	4.8895
Number of dimples		5
Dimple separation	mm	1.6
Dimple depth to diameter ratio k_d/d		$1.1\text{x}10^{-1}$
		11%

Dimple depth to cylinder diameter ratio k_d/D		$6.05\text{x}10^{-3}$ 0.605%
Dimples (D2)		
Indentation placement angle	$degrees$	20
Angular coverage	$degrees$	23.042
Dimple diameter d	mm	4.8895
Number of dimples		3
Dimple separation	mm	1.6
Dimple depth k_d n=1	mm	1.0757
Dimple depth to diameter ratio k_d/d		$2.2\text{x}10^{-1}$ 22%
Dimple depth to cylinder diameter ratio k_d/D		$1.21\text{x}10^{-2}$ 1.21%
Dimple depth k_d n=2	mm	0.80677
Dimple depth to diameter ratio k_d/d		$1.65\text{x}10^{-1}$ 16.5%
Dimple depth to cylinder diameter ratio k_d/D		$9.075\text{x}10^{-3}$ 0.9075%
Dimple depth k_d n=3	mm	0.5378
Dimple depth to diameter ratio k_d/d		$1.1\text{x}10^{-1}$ 11%
Dimple depth to cylinder diameter ratio k_d/D		$6.05\text{x}10^{-3}$ 0.605%
Dimples (D3)		
Indentation placement angle	$degrees$	55.416
Angular coverage	$degrees$	9.1771
Dimple depth k_d	mm	0.7112
Dimple diameter d	mm	7.112
Number of dimples		1
Dimple sphere diameter $\overline{d}$	mm	22.803
Dimple depth to diameter ratio k_d/d		$1\text{x}10^{-1}$ 10%
Dimple depth to cylinder diameter ratio k_d/D		$8\text{x}10^{-3}$ 0.8%
Dimples (D4)		
Indentation placement angle	$degrees$	15.416
Angular coverage	$degrees$	9.1771
Dimple depth k_d	mm	0.7112
Dimple diameter d	mm	7.112
Number of dimples		1
Dimple sphere diameter $\overline{d}$	mm	22.803
Dimple depth to diameter ratio k_d/d		$1\text{x}10^{-1}$ 10%
Dimple depth to cylinder diameter ratio k_d/D		$8\text{x}10^{-3}$ 0.8%
Effective mass	kg	2.05
Displaced mass	kg	5.6707
Dynamic Viscosity	Ns/m^2	$1.1379\text{x}10^{-3}$
Natural frequency in water	Hz	1.48
Oscillating mass	kg	10.75
PTC		
Strip placement angle	$degrees$	20
Angular coverage	$degrees$	16
Sandpaper and tape thickness	mm	0.587
Average grit thickness	mm	0.26

Total average strip thickness	mm	0.847
Strip thickness height to arc coverage (equiv to k_d/d)		$6.85\text{x}10^{-2}$ 6.85%
PTC height to cylinder diameter ratio (equiv k_d/D)		$9.53\text{x}10^{-3}$ 0.953%
Water density	kg/m^3	$9.991026\text{x}10^2$

Figures 20 show the main boundaries within the fluid domain designated as the outer domain, the moving domain sub-domain and the inner sub-domains. The moving sub-domain either side of the inner sub-domain contains all the elements that will be moved and remeshed by the cylinder spanwise motion. The square 2Dx2D inner sub-domain contains all the cylinder surface and a micro domain if one is used. The inner sub-domain moves with the cylinder motion to avoid any remeshing around the cylinder itself. The micro domain is only used for the PTC model and contains the surface texturing and the frontal stagnation point due to the very small element size requirements to achieve y+~1. The domains were created with computational expense in mind without affecting the solution quality. As recommended by the ANYSYS Meshing guide (2019c) the moving sub-domain uses a triangular elements while all other domains use quadrilateral elements. Appendix 1 shows the domains highlighted including the special case of the PTC micro domain.

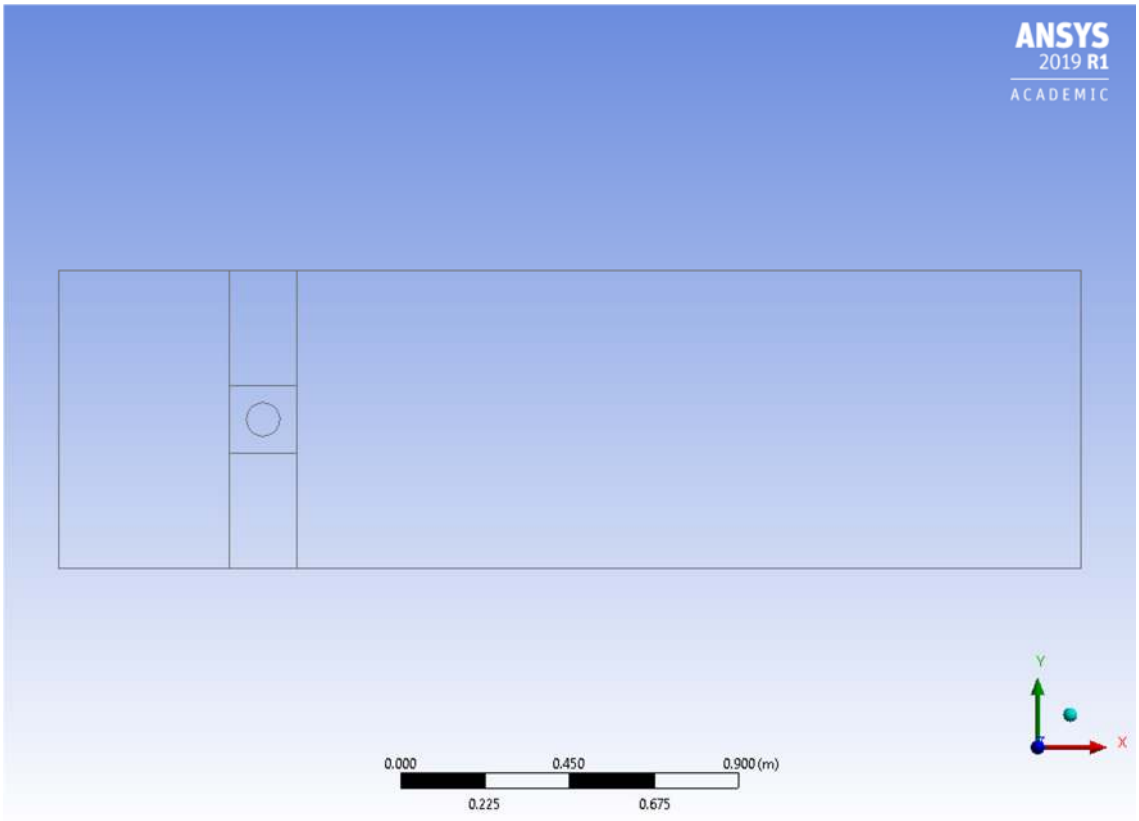

Figure 20: Image of the total domain

There were numerous iterations of adjustment to the mesh to get a satisfactory setting for the moving cylinder case. Issues included floating point exceptions because the mesh was not fine enough and calculations would not converge, instead going the opposite direction and becoming too large. Zero volume element errors occurred because the mesh would move to far in a single time step reducing the value of the volume below zero before it could be remeshed. Dynamic meshing is the process of adjusting the mesh around the moving parts which in this case is the inner sub-domain. The requirements for remeshing are to keep the mesh within the mesh quality limits of the original setup. This is achieved through several sub-routines called smoothing, layering and remeshing. Smoothing is the adjustment of the element centre position within the mesh. Layering is the process of merging elements that are being squashed below a certain value and splitting elements that are being stretched beyond a certain value. Remeshing is the adjustment of elements along a boundary, across a face or other regions and includes setting of parameters for minimum mesh qualities to trigger remeshing. Implicit updating is another option useful in dynamic meshing that has been utilised in this study. The implicit update causes the simulation to adjust the mesh for each iteration of a solution calculation instead of at each converged solution. Also, implicit updating will continue adjusting the mesh until errors in the mesh fall below a certain level as for the other residuals so that a remesh error is less likely to occur. Getting the right settings for one model simulation did not natural flow across to others and fine tuning was required throughout the CFD simulation process which takes an inordinate amount of time when processing can take hours to days before an error occurs that requires rectification.

An illustration of the overall mesh is given in figure 21(a). Figure 21(b) shows the named sections in the model which allow the assigning of properties. The named sections are the inlet which has the initial free flow velocity condition, the outlet which has a zero pressure assignment designed to allow free flow out but no back flow, the cylinder which has a no-slip condition applied and the outer-wall which is the top and bottom no-shear condition. Finer detail images of the mesh of the inner sub-domain are presented at appendix 2.

21(a)

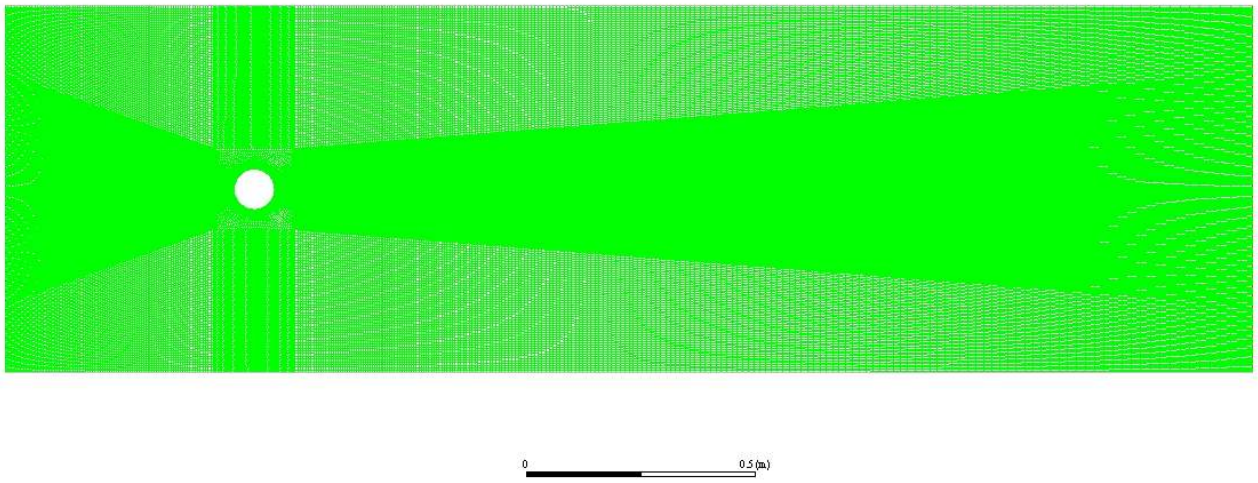

21(b)

Figure 21: Mesh diagrams (a) Overall mesh (b) Sections including inlet (blue), outlet (red), cylinder (centre grey) and outer wall (top and bottom grey)

The size of the cells in the square sub-domain are small and designed to produce a y+ approximately equal to one. The overall goal of the grid resolution is to achieve a convergent and accurate result with the maximum computational efficiency. To conduct the grid sensitivity, Fluent is solved for a steady case using the SST k-ω turbulence model with the low Reynolds number option selected and the PISO coupling solver method with a value of 10 set for skewness correction. The SST k-ω model is selected because it is the simplest available to resolve the turbulence down to y+≈1 but still requires the level of grid scale and accuracy to achieve convergence. The PISO solver is used because it is the same solver as used by Ding et al (2016) for the VIVACE simulation and recommended for transient simulations which will be conducted in the final simulations. The low Reynolds number option is selected because it accounts for the low Reynolds numbers experienced within the boundary layer as the distance from the wall decreases.

The PISO skewness correction is used because of the fine resolution required around the PTC needing distortion correction. The schemes used for the PISO solution, in accordance with the recommendations of the Fluent User Guide (ANSYS 2019b, chaps. 12, 37), are listed in table 5.

Table 5: Pressure-Velocity Coupling Solution Scheme for Grid Independence Study

Scheme	PISO
Neighbour Correction	1
Skewness Correction	10
Neighbour-Skewness Coupling	Yes
Spatial Discretization	
Gradient	Least Squares Cell-Based Gradient Evaluation
Pressure	PRESTO!
Density	Second Order Upwind
Momentum	Third-Order MUSCL Scheme
Turbulent Kinetic Energy	Third-Order MUSCL Scheme
Turbulent Dissipation Rate	Third-Order MUSCL Scheme
Transient Formulation	N/A – steady state solution

The grid parameters and the results of a sensitivity test are in table 6 which shows that increasing the size of the inner grid quickly caused meshing failure due to inability to capture the curvature around the PTC. The two larger grid sizes did not converge satisfactorily and so the fine grid with the largest number of cells was used in this study. The convergence data for the three grids is at figures 22(a) to 22(c).

Table 6: Grid Sensitivity Study Re=30,000

	Desired Value	Course	Medium	Fine
Cell count	Smallest	229110	248086	310054
C_D	~1	N/A	N/A	1.0392
Strouhal number	~0.2	N/A	N/A	0.237
Aspect ratio	Max < 5	3.66	3.34	3.87
Skewness	Avg < 0.25	0.13	0.14	0.13
Orthogonal quality	Avg ~1	0.97	0.97	0.97
Element quality	Avg ~ 1	0.88	0.88	0.88
Residual Convergence	Yes (# iterations)	No	No	Yes (764)
y+	<5 prefer 1	1.0	0.9	0.9

22(a)

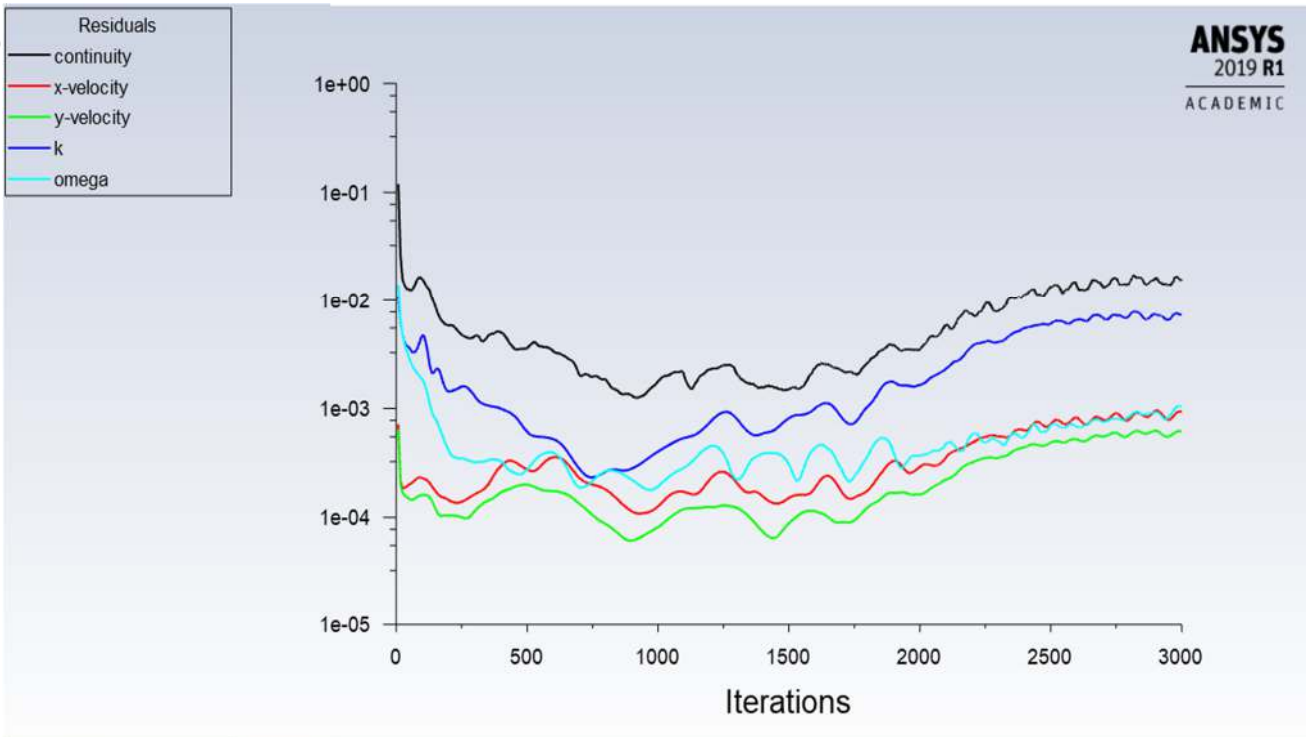
Residuals
continuity
x-velocity
y-velocity
k
omega
ANSYS
2019 R1
ACADEMIC
1e+00
1e-01
1e-02
1e-03
1e-04
1e-05
0
500
1000
1500
2000
2500
3000
Iterations

22(b)

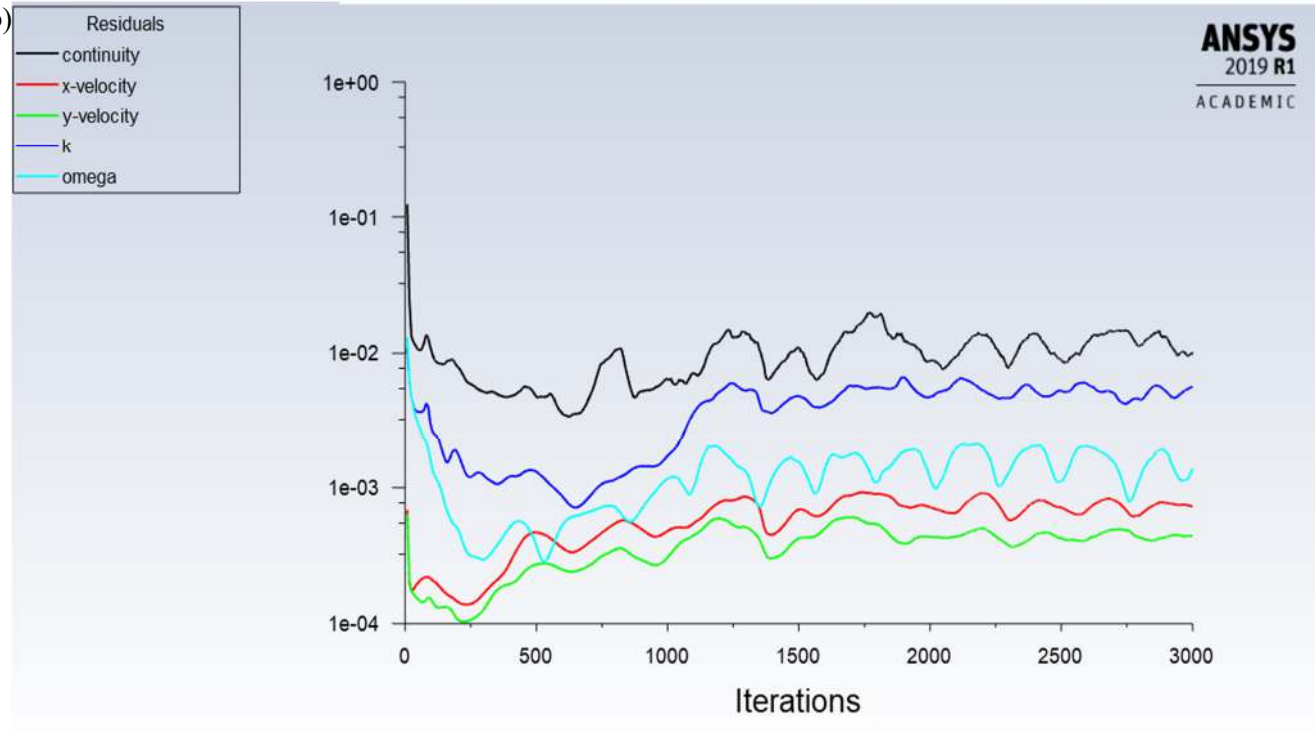
Residuals
continuity
x-velocity
y-velocity
k
omega
ANSYS
2019 R1
ACADEMIC
1e+00
1e-01
1e-02
1e-03
1e-04
0
500
1000
1500
2000
2500
3000
Iterations

22(c)

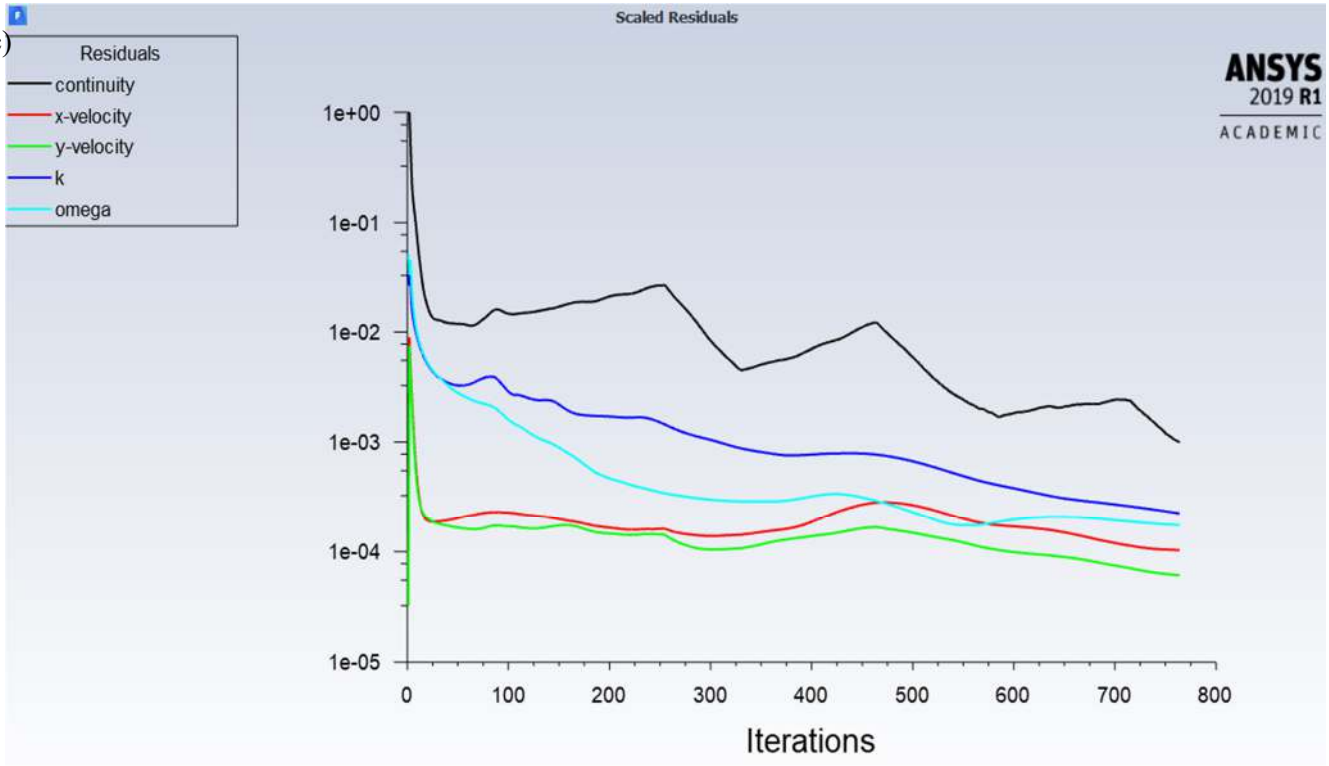

Figure 22: Residual plots for three PTC grid sizes (a) course (b) medium (c) fine

Next was the setup of the CFD models and methods in preparation for solving the motion simulation of the cylinder using a transient solution. From the literature review (Hart 2016) it is clear that DDES gave good results with the SST k-ω model incorporated and is used in this study with properties as listed in table 7. The pressure velocity coupling remains a PISO solution with the addition of the transient formulation.

Table 7: Pressure-Velocity Coupling Solution Scheme for PTC and indentations

Scheme	PISO
Neighbour Correction	1
Skewness Correction	10
Neighbour-Skewness Coupling	Yes
Spatial Discretization	
Gradient	Least Squares Cell-Based Gradient Evaluation
Pressure	PRESTO!
Density	Second Order Upwind
Momentum	Third-Order MUSCL Scheme
Turbulent Kinetic Energy	Third-Order MUSCL Scheme
Turbulent Dissipation Rate	Third-Order MUSCL Scheme
Transient Formulation	Bounded Second-Order Implicit Time Integration

4 PTC CFD Comparison

The results of the PTC simulation in this study are compared with Ding et al (2016) to create a valid baseline of the setup for the next stage of the research. First is a closer look at the results of flow around the PTC to determine the action at the wall as this has not been looked at by other studies. The points of interest are the pressure coefficient and velocity profiles. Three profiles of each are taken at three points in the movement of the cylinder at Reynolds numbers 30,000 and 90,000 respectively and shown in figure 24. The first frame (which is on the bottom of the three images) is just after starting motion, arbitrarily in the +y direction from the maximum -y position. The second frame is as the cylinder passes through the centreline of the domain and the third frame is 3/4 of its motion from $-y_{max}$ to $+y_{max}$ positions. The positions are illustrated in figure 23.

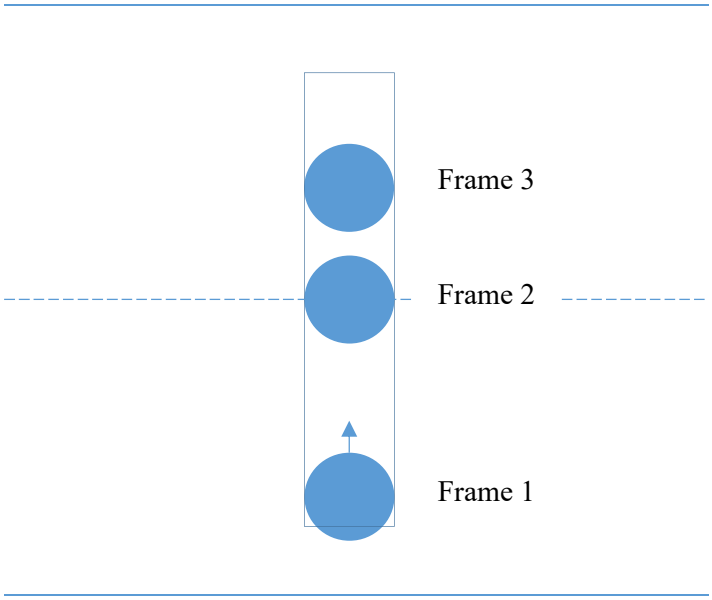

Figure 23: Position of cylinder during frame freezes for pressure and velocity analysis around PTC and how they appear in the figures 24 below from frame 1 on the bottom to frame 3 on top.

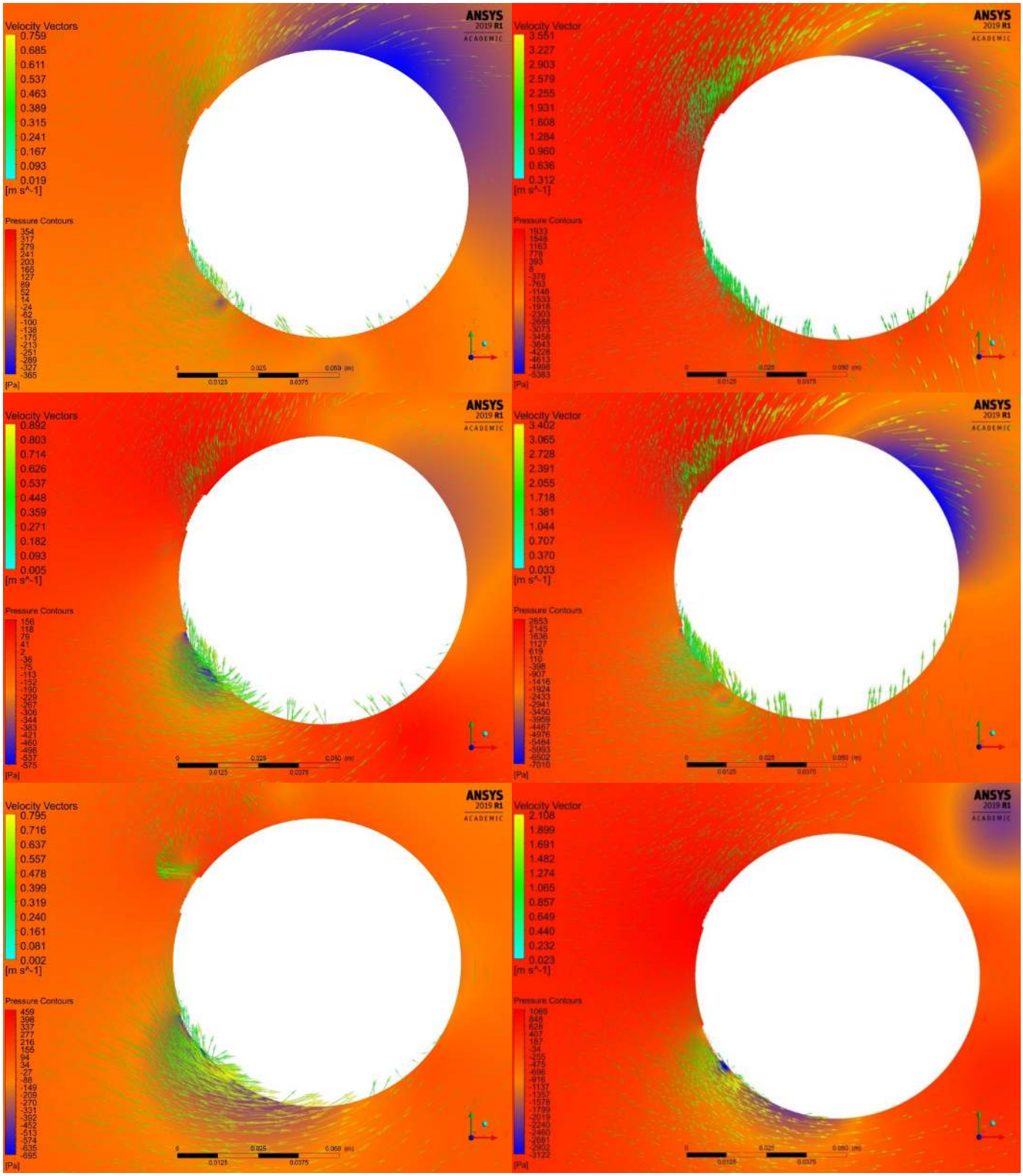

Figure 24: Comparison of pressures and velocities as the cylinder is in motion for three different Re of 30,000 (left) and 90,000 (right)

These pressure and velocity diagrams are useful as they show the effects of the PTC on the flow around the front of the cylinder. The pressure and velocity are scaled in each image to the local values giving a comparison of the effects as the Reynolds number increases. Note that the cylinder is travelling up the page in each image.

Reynolds number equal to 30,000 are the leftmost set of each row of images. At the bottom of the upwards motion (bottom left diagram) the flow around the top PTC shows that although there is a significant pressure bubble at the top edge of the PTC the velocity is being accelerated away from the cylinder and then reversed. This is a remnant of the original downwards motion of the cylinder and the subsequent reversal of direction. On the bottom PTC the pressure drop begins around the PTC and there is complex velocity and pressure micro phenomena occurring in and around the PTC and thus the boundary layer. The macro effect of the bottom PTC is that of increased turbulence whereas on a smooth surface there would be steadily dropping pressure and laminar flow in the boundary layer. The second Re=30,000 diagram middle left shows that the top PTC is having a small effect only on the leading edge reversing a small amount of flow. The bottom PTC is continuing to cause turbulence across its surface, but no longer extends past the PTC towards the bottom of the cylinder and the area of low pressure has decreased with increased flow in the direction of motion. The overall pressure has increased around the cylinder and the main pressure nodes are at the 5 o'clock and 10 o'clock positions. The final frame for Re=30,000 top left shows pressures overall are dropping around the cylinder, with a low-pressure bubble around 1 o'clock and separation occurring around 11 o'clock aft of the top PTC. The bottom PTC has a small low-pressure bubble due to flow being turned around and pushing up against the roughness.

Reynolds number equal to 90,000 are the righthand group of images. The result of increasing Reynolds number is to amplify the numbers involved for the Reynolds number 30,000 case with respect to pressure and velocity in both the values but also the magnitude of the differential between areas. An example is the low-pressure area at the aft end of the lower PTC for the first frame of each Reynolds number. As Reynolds number has increased the pressure bubble at the training edge of the PTC has gone from being indistinct amongst the other low pressure areas within the PTC at Reynolds number 30,000 to being an area of relatively very low pressure affecting the flow around it including flow reversal despite the increased flow momentum and the majority of the flow not being affected by the PTC. The movement of the separation point further back on the cylinder with increased Reynolds number is also evident suggesting that at Reynolds number 90,000 the cylinder is approaching the end of the TrSL3 regime and beginning to enter TrBL0. This is in agreement with Ding et al (2016, 1252) results.

Quantitative results of the CFD analysis and the comparison to Ding et al (2016) with respect to displacement history and frequency spectrum are presented in figures 25 to 30 and table 8 is a summary of the results for Reynolds numbers at 30,000 intervals.

Table 8: Comparison of amplitude ratio and frequency ratio between Ding et al (2016) and current study

Reynolds Number	Ding et al		Current study	
	A^*_{60}	f^*	A^*	f^*
30000	0.58	0.39	0.15	0.08
60000	1.58	1.09	0.54	0.54
90000	1.79	1.11	0.82	0.55

Some immediate differences in the results of figures 26 to 31 are the lack of data in the current study. This is due to the resources available. To achieve the same density of data a time step size for the transient simulations of $4.5\text{x}10^{-4}$ seconds is required. When a simulation was started at this time step size on the computing resources available it was estimated to require over a week of processing based on the initial time to resolve residual convergences. Indeed, the simulation data density presented here varies by time scale and the quantity of data collected to optimise the computing resources and still give meaningful comparisons. This has been partially achieved with Re=90,000 result failing due to meshing issues after 26 hours of computation and insufficient time to recalculate without compromising the collection of further results. The results shown here are the outcome of approximately 8 hours processing each.

A further issue is with the definition of the motion for the cylinder being defined as the integral of the cylinder position is that the centre location is not tracked by the area of the cylinder. This has resulted in a ratio error of unknown size and skewed results. An analysis of the differences in results did yield a factor of $0.975\pm7\text{x}10^{-3}$ difference on average between the amplitude ratio results indicating that they are consistent and relevant however this brings into question the validity of quantifying the results of the indentations using the PTC as a baseline.

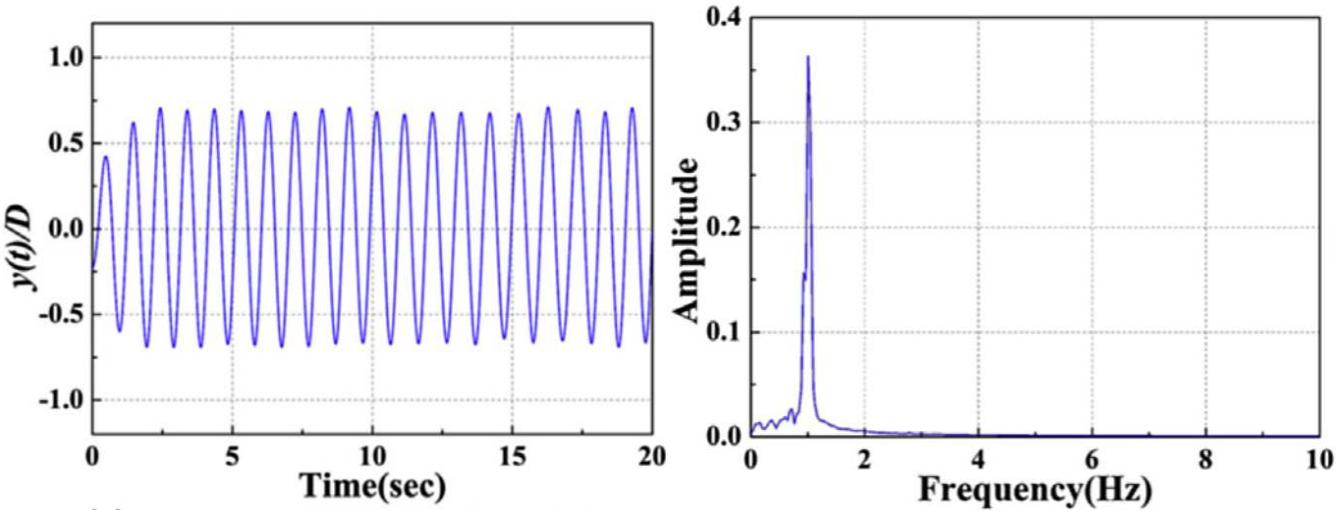

Figure 25: Ding et al (Ding et al. 2016, fig. 8) Re=30,000 displacement ratio and frequency spectrum

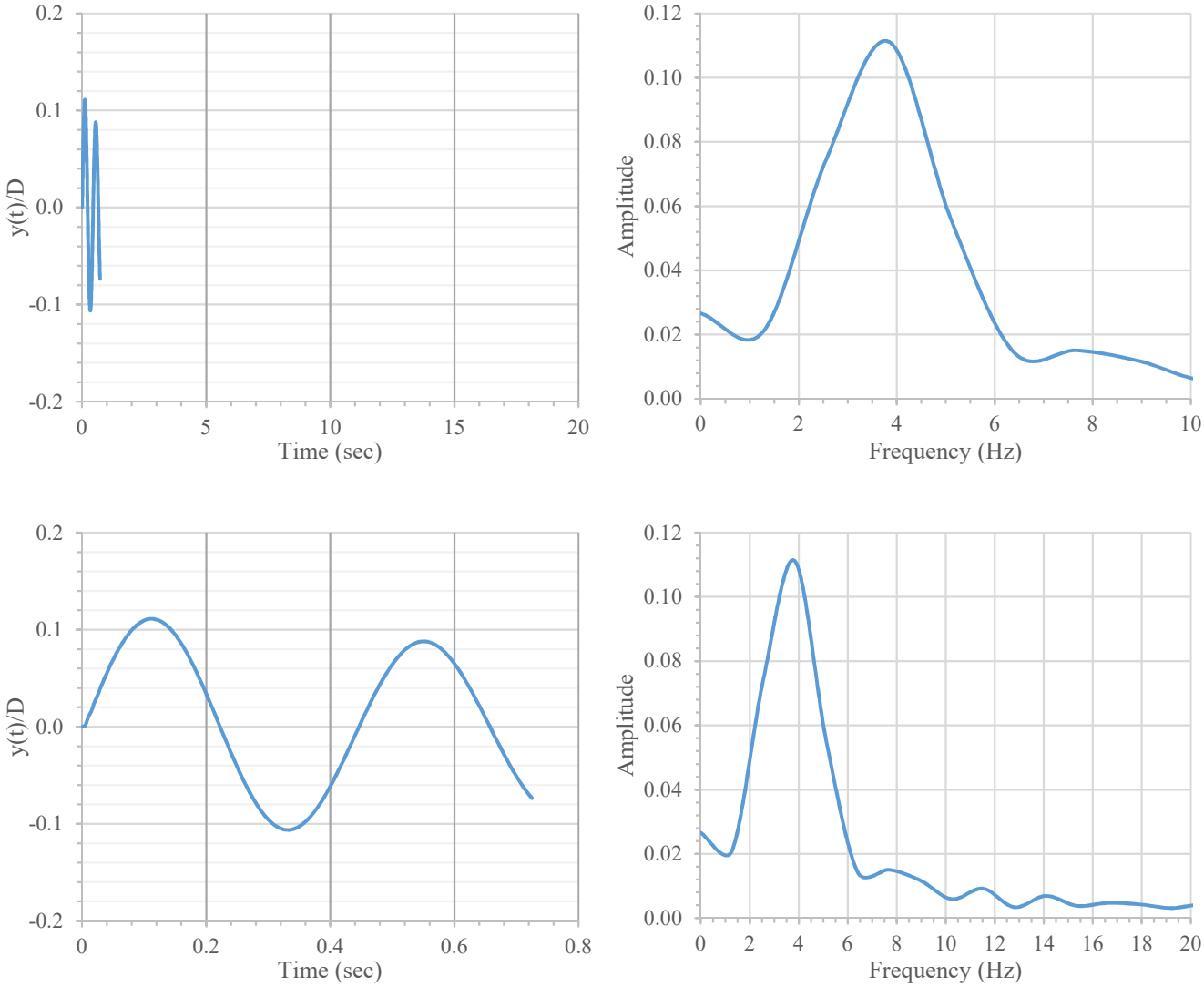

Figure 26: Current Study PTC Re=30,000 displacement ratio and frequency spectrum showing the same scales as figure 25 and then more realistic scales

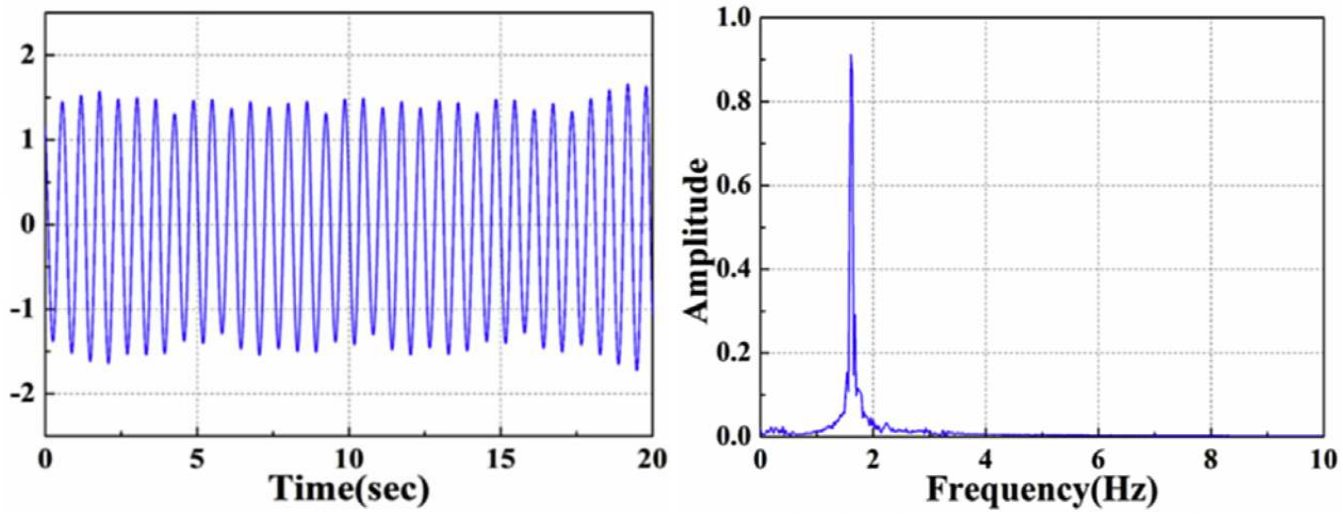

Figure 27: Ding et al (Ding et al. 2016, fig. 8) Re=60,000 displacement ratio and frequency spectrum

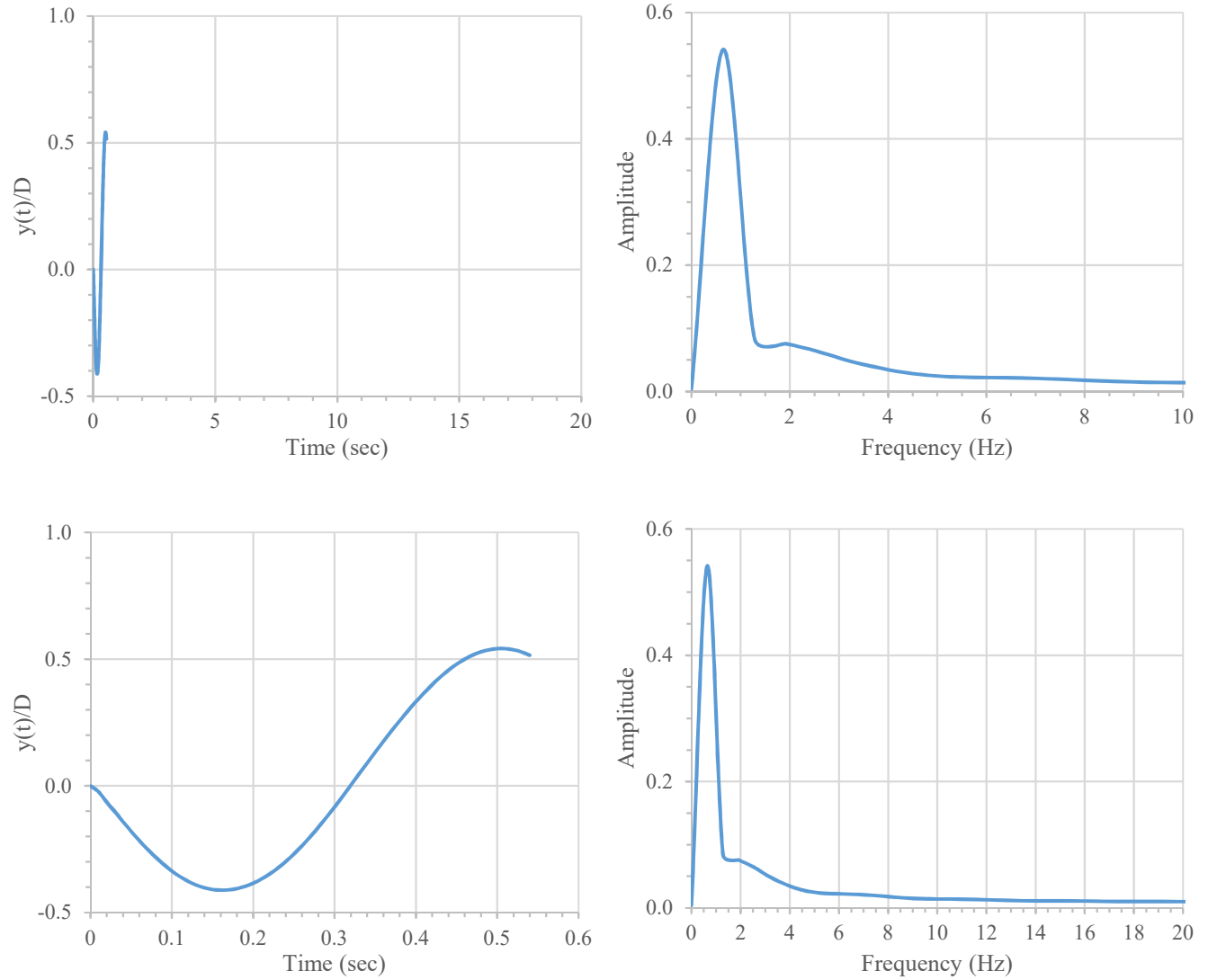

Figure 28: Current Study PTC Re=60,000 displacement ratio and frequency spectrum showing the same scales as figure 27 and then more realistic scales

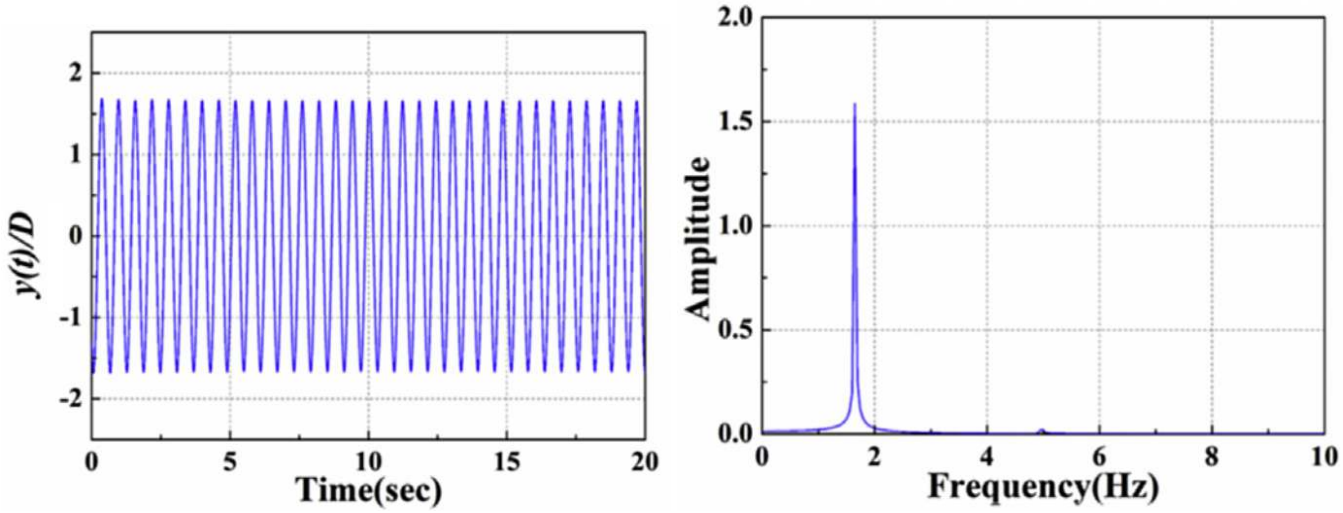

Figure 29: Ding et al (Ding et al. 2016, fig. 8) Re=90,000 displacement ratio and frequency spectrum

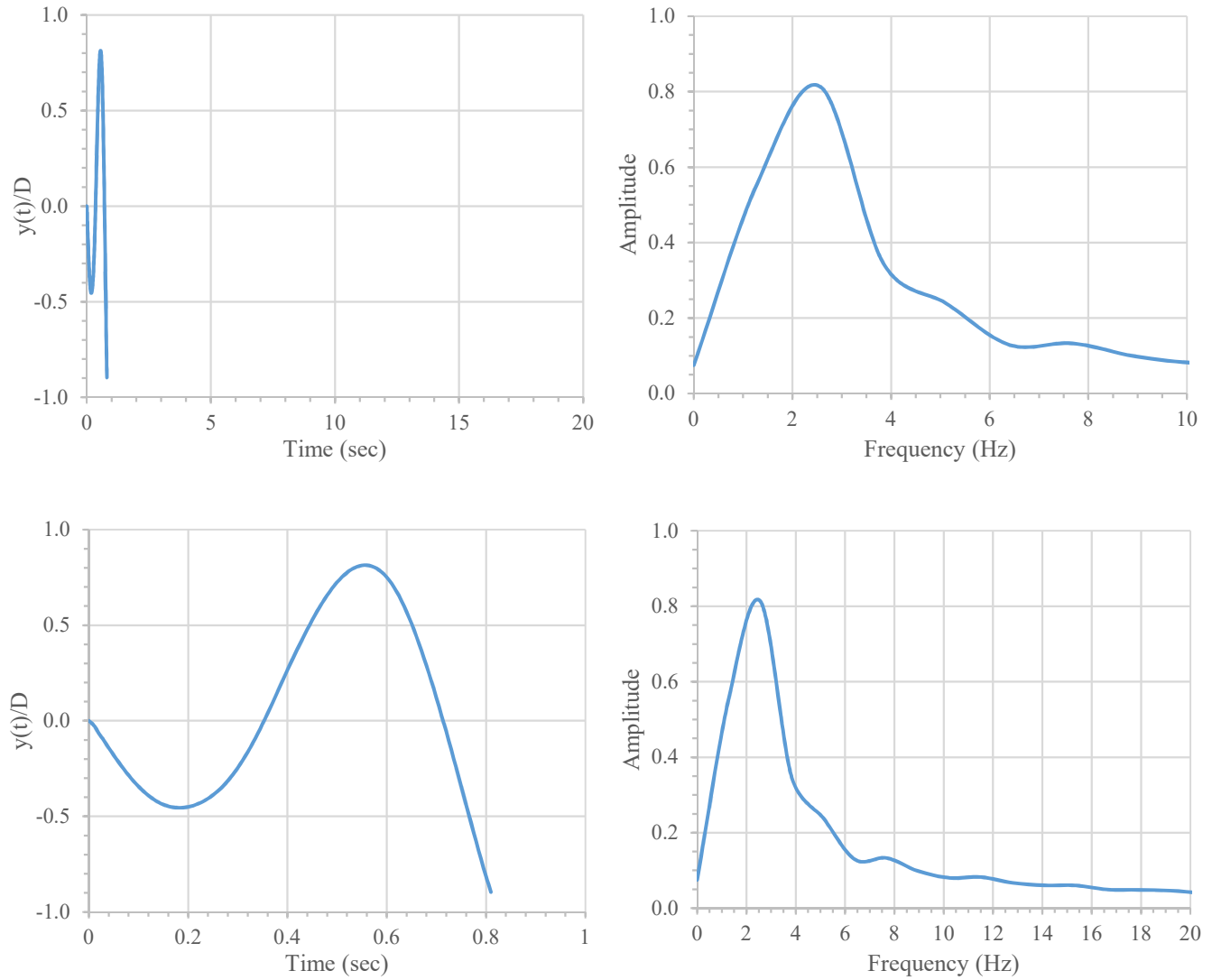

Figure 30: Current Study PTC Re=90,000 displacement ratio and frequency spectrum showing the same scales as figure 29 and then more realistic scales

Another method considered for PTC result validation is analysis of the motion videos created. Snapshots of the videos are taken and presented in figure 31-32 showing that displacement is indeed greater than shown in the data presented in table 8 however there are increased method errors with this approach. Error generating limitations of this technique include not only measurement accuracy but time between video frame grabs is lost. Table 9 has the comparisons with table 8 based on approximations from the motion files.

Table 9: Measurement comparisons of amplitude ratio using images

Reynolds Number	Ding et al	Current study from Fluent	Current study from images
30000	0.58	0.15	0.5
60000	1.58	0.54	1.88
90000	1.79	0.82	2.85

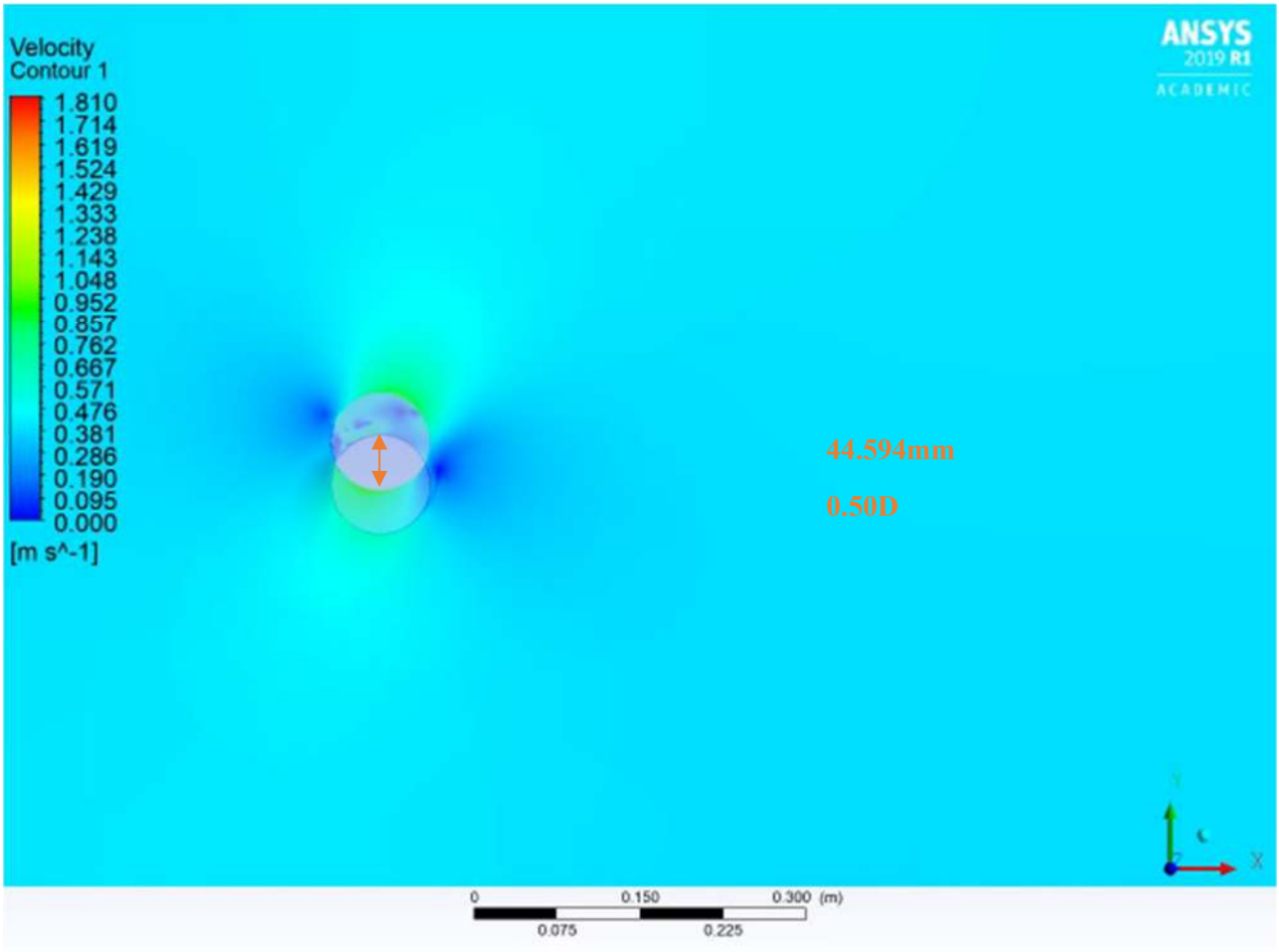

Figure 31: Amplitude measured by video stills for Re=30,000 in Photoshop CC©

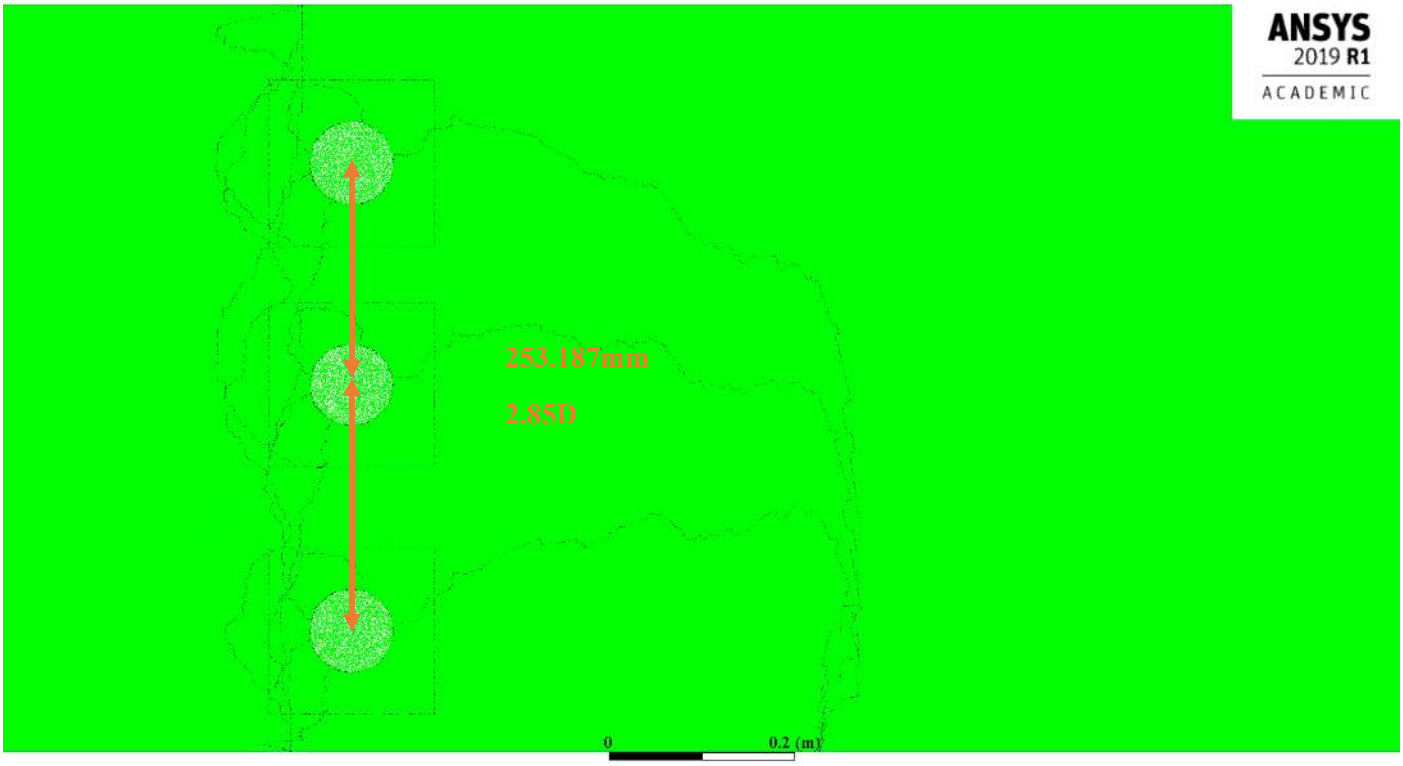

Figure 32: Amplitude measured by video stills for Re=90,000 in Photoshop CC©

The results of the image analysis suggest that the amplitude data collected, being the integrated product of all the cylinder circumference position at each time step is produced an incorrect value for the amplitude of the centre of the cylinder. Applying a correction factor to the data using the graph in figure 33, produced by correlating the errors from table 9 will assist in analysing the dimple results to come. The large difference in value for the Reynolds number 90,000 case may be due to the approaching drag crisis. For a smooth cylinder the expectation would be for a large amplitude drop in and around this region however the literature suggest that the effect of surface roughness as applied in this case and in Ding et al (2016, 1252–53) is that the drop is very minor and then galloping commences with significant increases in amplitude.

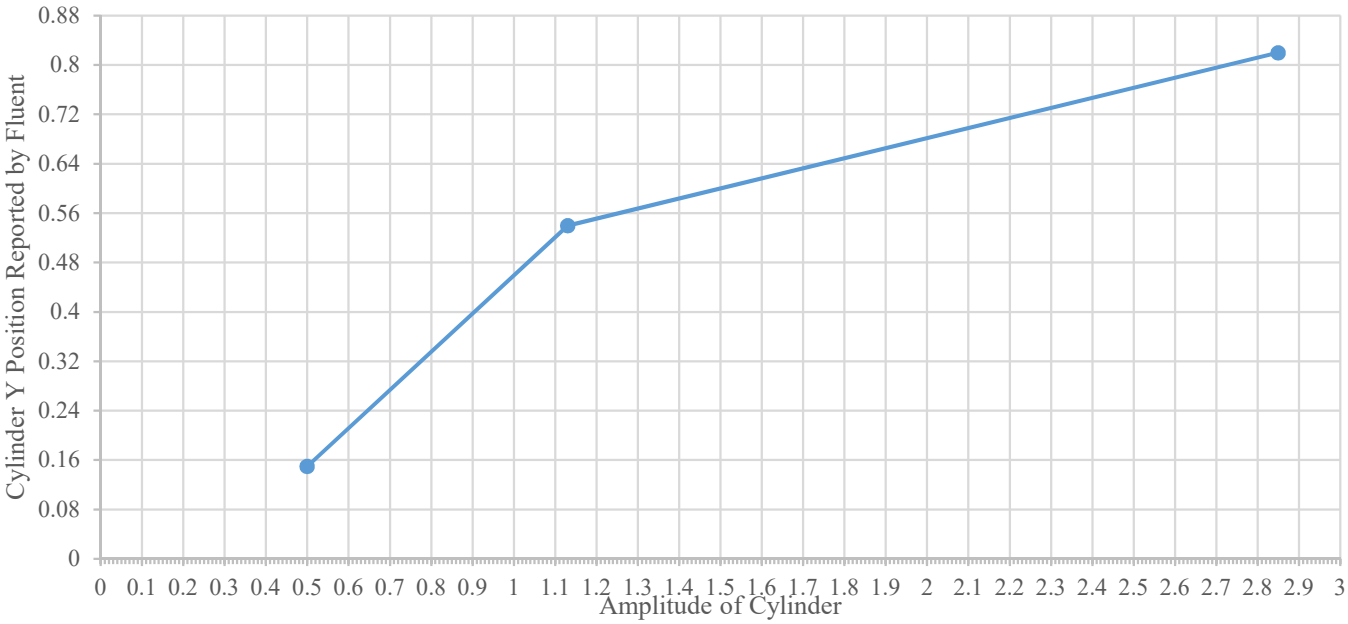

Figure 33: Correction factors for cylinder position as reported by Fluent

Subsequent analysis post writing this section of the report has found that the amplitude data was being written to file however it was being written to the same folder and file name during each simulation through operator error. Therefore, the accurate results for each of the simulations was overwritten and lost. The last files found were for PTC Re=60,000 and are presented in figure 34 as the actual results of amplitude ratio and frequency spectrum.

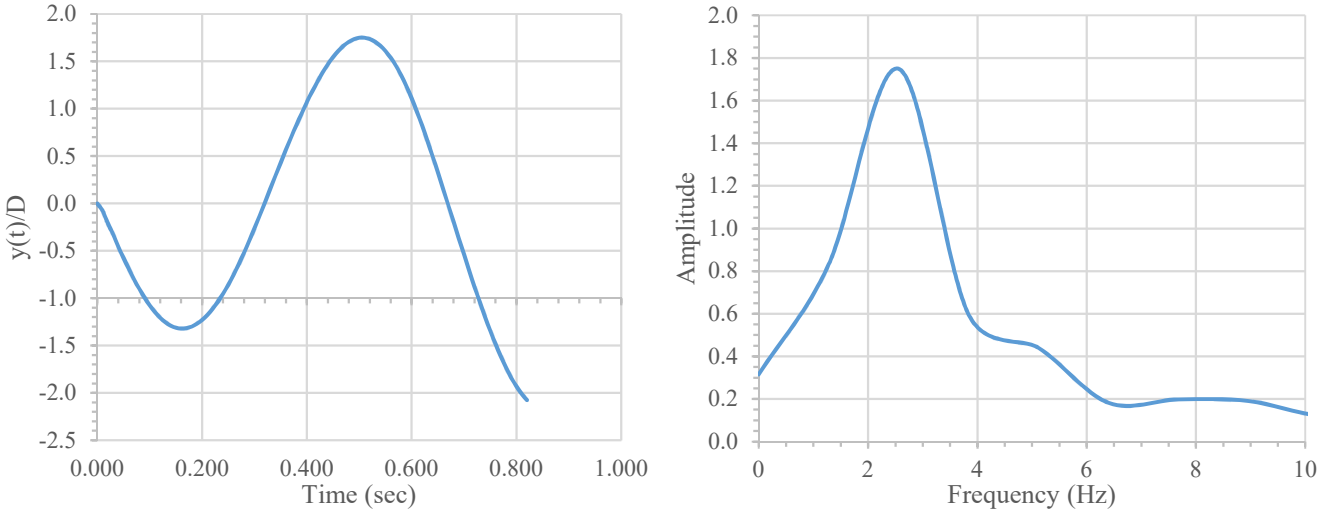

Figure 34: Actual data for amplitude ratio and frequency spectrum for PTC of Re=30,000

Comparing the results in figure 34 with figure 27 confirms a similar result between the PTC in this simulation with the published results regarding amplitude. This corroborates the finding that this simulation represents a suitable system for comparison of surface roughness versus indentations.

5 Indentation Cylinder CFD Results and Discussion

Dimple configurations will be investigated in four cases. The results of the simulations will be compared to the results of already discussed for PTC. The data to be considered will include flow analysis, amplitude ratios and frequency ratios.

5.1 Dimple Case 1 (D1) – Five indentations, Same $k_d/D = 6.05\text{x}10^{-3}$, Arc 20° - 60°

This initial case for dimples was to investigate a solution that provided a wide range of angles to optimise a fixed cylinder for flow angles away from the optimum. Diagrams of pressure and velocity at figure 35.

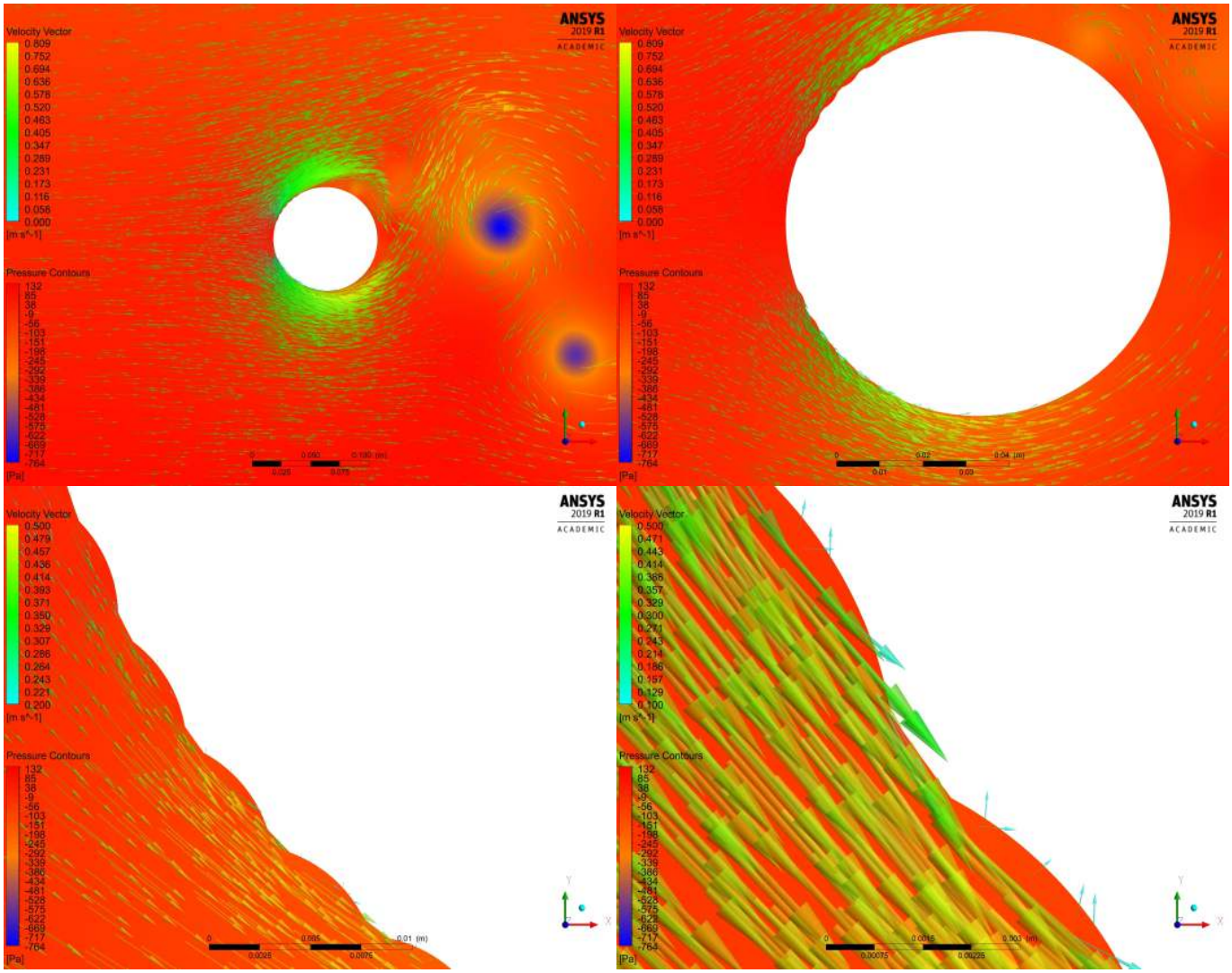

Figure 35: Pressure and velocity diagrams for D1 at Re=30,000

The data amplitude and frequency spectrum data for D1 at Re=30,000 is presented at figure 36.

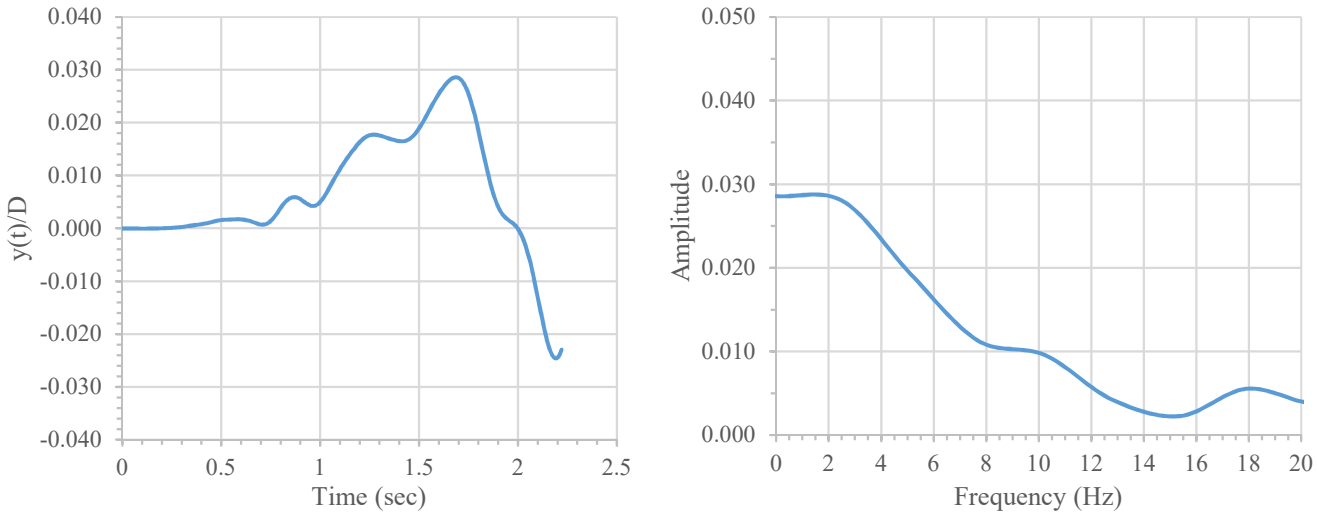

Figure 36: Five dimple setup results for amplitude ratio and frequency spectrum at Re=30,000

5.2 Dimple Case 2 (D2) – Three indentations, Varying $k_d/D = 6.05\text{x}10^{-3} - 1.21\text{x}10^{-2}$, Arc 20° - 43°

This case was to consider the effects of varying dimple depth ratio k_d/D given the results of D1 with the aim to achieve an initial separation but reattachment and consolidation of the boundary layer after the degradation of turbulent flow from the increasingly shallow dimples. The simulations for this case did not progress to any form of oscillation and were completely damped. The simulation was run multiple times with different configurations and in the end resulted in no results because of simulations exhausting computer resources without a result other than very minor excursions from the centreline.

5.3 Dimple Case 3 (D3) – One indentation, $k_d/D = 8\text{x}10^{-3}$, Arc 55°

From the results of Beratlis et al (2014) and Hart (2016) it was determined to try a single dimple at 60° which is considered the upper limit of where to place PTC (Chang, Kumar, and Bernitsas 2011). Figure 37 has the pressure and velocity vector results.

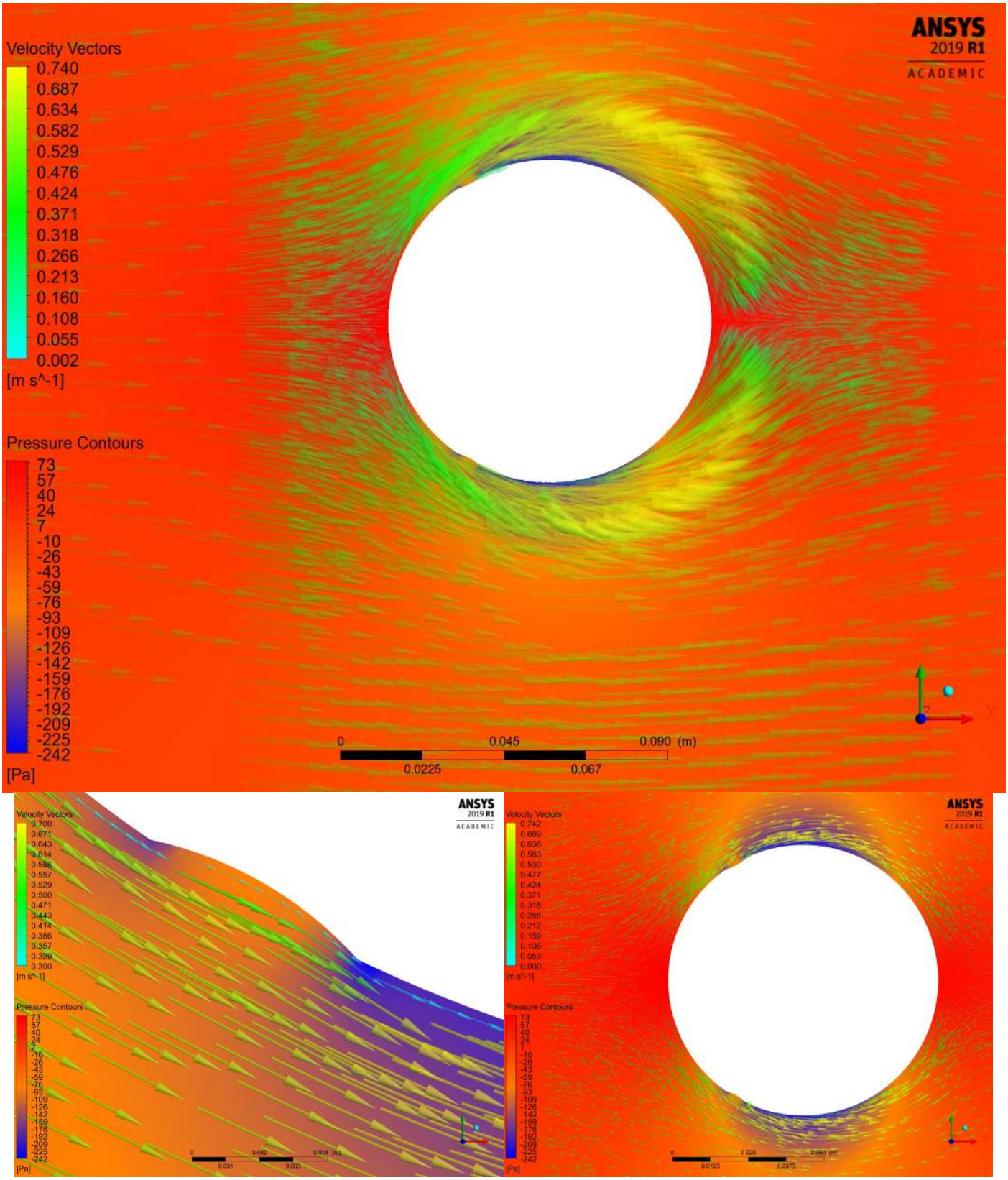

Figure 37: Case D3 pressure contours and velocity vectors at varying levels of zoom.

5.4 Dimple Case 4 (D4) – One indentation, $k_d/D = 8x10^{-3}$, Arc 15°

The theory here is that D3 effected the boundary layer so moving the same dimple to the area that the PTC operates may be effective. This is the most promising of the dimple cases but is unclear on the result due to simulation failure and therefore no stable FIM was evident. Figure 38 presents the data of amplitude and frequency spectrum for D4 at Re=30,000. The two peaks in the frequency spectrum suggest the cylinder has two frequencies that it will modulate at depending on the pressure distribution and wake patterns. Without a video of the motion it is difficult to determine if the variation between the two frequencies was periodic. In any case the amplitude ratio prior to the simulation failure was underwhelming while the gradient of the final increase was promising.

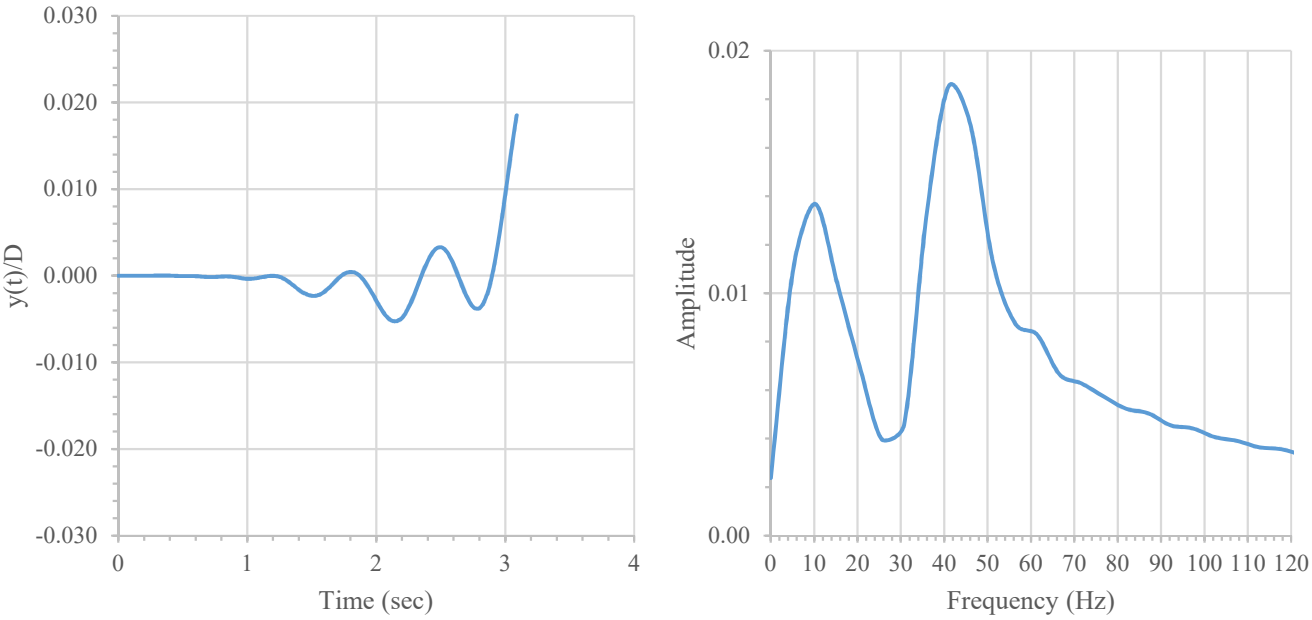

Figure 38: D4 results of amplitude and frequency spectrum at Re=30,000 before simulation failure

5.5 Discussion of Results

Dimples have not had the same effectiveness in amplifying FIM as PTC in the domains tested. Case 3 and 4 showed that a single dimple is capable of significantly effecting the boundary layer however the mechanism of why this did not resolve into significant amplitude variations like PTC is unclear given the failure of the simulation.

Case one completely dampened the oscillation at Re=30,000. A longer run would have been preferred to see if the trend continued however it was thought moving to other Reynolds numbers and dimple configurations was more

likely to produce results and so higher Reynolds numbers were not conducted. There continued to be vortex shedding as has been found in studies of fully covered dimples.

Case two was a failure with no oscillations occurring and almost total damping. There was a high level of interaction with the boundary layer at the leading and trailing edge of the dimple. The separation point was maintained in a single place for the time period the simulations was run and so also created almost complete damping.

There is still much to investigate and understand about circular cylinders with partial coverage of indentations. The time taken to complete a full cycle of CFD for each dimple scenario, the intermittent failures of simulations for varying reasons, inexperience with the software and multiple formats for determining results all contributed to the both inconsistency in tabling data and poor graphical analysis.

The failure to have a conclusive result is meaningful of itself. The CFD objective, model inputs, model outputs and limited variables are understood but the criteria for determining what to do post model failure was not considered or clearly articulated during the data collection phase. The decision model to determine next steps such as change Reynolds number, redesign model, move to next case or re-run the existing simulation was not conducted in a process driven method based on rational consideration of the underlying issues but rather ad-hoc theorising on what the results of the next case may be. Indeed, there was insufficient articulation or reasoning behind different simulation case design at the time of design.

The lessons learnt here for future studies is to understand what results will look like and a decision matrix on failure or success and what data is required to confirm this allowing a move to the next case. This may for example be a gate model process where passing through a gate to the next iteration of simulation/case/design is dependent on satisfying a checklist of outcomes based on reasonable, repeatable and understood result. The development of the gate checklist may require an initial scoping process like the outcomes presented in this study. Once the gate checklist is completed it should have limited alteration allowed otherwise the results become invalid across the study.

6 Conclusion and Recommendations

This dissertation investigates the use of indentations versus surface roughness for FIM of an elastically attached cylinder at velocities relevant to the marine environment. Specifically required is a CFD analyses of smooth indentations as a viable alternative to the current design of VIVACE using PTC surface roughness after establishing that this system has a potential problem with biofouling.

Completing this study required understanding and applying complex FIM and FSI; CFD limitations and implementation methodology and determining and learning suitable CFD software. The introduction describes the hypothesised problem and proposed solution and details terminology and basic physics required to analyse the results with topics on FIM, VIV and CFD. The literature review provides understanding of existing research in FIMEG technology, the analysis of surface roughness and proposed alternative of indentations effect on FIM, marine biofouling research and finally CFD techniques for analysis of the FIM.

It is established in the literature review that biofouling will indeed be a problem for the current design of VIVACE due to the size, angle and spacing of the surface roughness which will lead to colonisation by marine organisms and reduction in the effectiveness of FIM amplitudes. The hypothesis that dimples or other indentations are free from biofouling is not evident in the literature however there is evidence to suggest that smooth surfaces with thin film deposition are successful as an antibiofouling coating. It is concluded for the first research objective that smooth indented cylinders could be a viable alternative to roughened surfaces to mitigate marine biofouling for VIVACE.

An investigation using CFD to establish if indentations will produce similar amplitude response to PTC of an elastically attached cylinder to is undertaken. To conduct the investigation a baselining of the CFD setup with existing literature is conducted and then alternative design analysis interface and application.

Section three described the CFD model design and setup, highlighting the considerations used to overcome or minimise shortfalls of CFD for FSI identified in the literature review. Most importantly this section described the exact setup so that the study could be recreated in the future for comparison, validation, critique or refinement.

Section four compared results between a replication of the PTC simulation using this authors setup versus published results in order to establish a valid baseline of the setup for the next stage of the research. This section illustrated the flow around the surface of the cylinder at varying Reynolds numbers and describes the effect of the PTC as determined by the simulation. Issues with the validity of the initial comparison technique were discussed and an alternative method identified which provided confirmation of comparable results between the models validating findings from the indentation study.

Section five details the result of this research regarding indentations effectiveness as an alternative to PTC. Four variations of smooth and shallow indentations called dimples were simulated. Case one consisted of multiple dimples to allow for variations in oncoming water flow angles, case two used varying dimple depths, case three was a single dimple at the extremes of where PTC might be placed on the cylinder and case four was a single dimple in the same position as the existing PTC. The results are inconclusive at the time of writing due to computational resource limitations however none of the dimple cases tested produced significant oscillations to the level that would be conceivable to replace PTC and indeed the majority had the opposite effect and dampened the FIM.

The inability to conclusively determine the outcome of indentations versus surface roughness is due to several failures:

- The requirement for longer time runs of the CFD through two mechanisms:
    - Higher powered computers or online processing to reduce the time to complete calculations, and
    - Improved model configuration to prevent errors of memory shortage and/or model collapse.
- The need for an improved process:
    - To understand results of one simulation versus another, and
    - A decision matrix on when and how to proceed through well-defined indentation designs.

- Further training on the CFD software will also provide insight into improved model design.

Further research on this topic is recommended to inform the future development of FIMEG. Specific aspects that require further refinement, analysis and investigation include:

- Completion of timescales to confirm baseline of model design.

- Investigation to confirm:

    - Power and efficiency effects of biofouling on PTC specifically in the VAVACE case,

    - Maintenance and financial implications of biofouling are a significant factor, and

    - Thin film deposition will not work for roughened surfaces.

- Confirmation of smooth indentations treated with thin film deposition are anti-biofouling.

- Three-dimensional simulations to investigate:

    - Crossflow between indentations,

    - Dimple patterns, and

    - Channel/s spanwise along the cylinder vice dimples.

References

Achenbach, E. 1971. “Influence of Surface Roughness on the Cross-Flow Around a Circular Cylinder.” *Journal of Fluid Mechanics* 46: 321–35.

Achenbach, E., and E. Heinecke. 1981. “On Vortex Shedding from Smooth and Rough Cylinders in the Range of Reynolds Numbers 6e3 to 5e6.” *Journal of Fluid Mechanics* 109: 239–51.

Alonzo-García, A., C. Del C. Gutiérrez-Torres, J. A. Jiménez-Bernal, J. L. López-Aguado-Montes, J. G. Barbosa-Saldaña, H. R. Mollinedo-Ponce-De-Leon, and S. A. Martinez-Delgadillo. 2015. “Large Eddy Simulation of the Subcritical Flow over a v Grooved Circular Cylinder.” *Nuclear Engineering and Design* 291 (July): 35–46. https://doi.org/10.1016/j.nucengdes.2015.05.001.

ANSYS. 2016. *ANSYS Meshers Guide*. 16th ed.

———. 2019a. *Fluent Theory Guide*. 19.3.

———. 2019b. *Fluent Users Guide*. 19.3.

———. 2019c. *Meshers User Guide*. 19.3.

Arioli, G., and F. Gazzola. 2015. “A New Mathematical Explanation of What Triggered the Catastrophic Torsional Mode of the Tacoma Narrows Bridge.” *Applied Mathematical Modelling* 39 (2): 901–12. https://doi.org/10.1016/j.apm.2014.06.022.

Bearman, P. W. 2011. “Circular Cylinder Wakes and Vortex-Induced Vibrations.” *Journal of Fluids and Structures* 27 (5–6): 648–58. https://doi.org/10.1016/j.jfluidstructs.2011.03.021.

BEARMAN, P. W., and J. K. HARVEY. 1993. “Control of Circular Cylinder Flow by the Use of Dimples.” *AIAA Journal* 31 (10): 1753–56. https://doi.org/10.2514/3.11844.

Beratlis, N., E. Balaras, and K. Squires. 2014. “Effects of Dimples on Laminar Boundary Layers.” *Journal of Turbulence* 15 (9): 611–27. https://doi.org/10.1080/14685248.2014.918270.

———. 2018. “The Role of Surface Texturing on the Physics of Boundary Layer Separation over a Bump.” *International Journal of Heat and Fluid Flow* 73 (August): 223–35. https://doi.org/10.1016/j.ijheatfluidflow.2018.08.006.

Beratlis, N., E. Balaras, K. Squires, and A. Vizard. 2016. “Simulations of Laminar Boundary-Layer Flow Encountering Large-Scale Surface Indentions.” *Physics of Fluids* 28 (3). https://doi.org/10.1063/1.4943664.

Bernitsas, M. M. 2015. “VIVACE „Vortex Induced Vibration Aquatic Clean Energy…: A New Concept in Generation of Clean and Renewable Energy From Fluid Flow.” OMAE06-92645. https://doi.org/10.1115/1.2957913.

Bernitsas, M. M., and K. Raghavan. 2008. Reduction of vortex induced forces and motion through surface roughness control. 8,684,040, issued 2008.

Berntsson, Kent M., Per R. Jonsson, Magnus Lejhall, and Paul Gatenholm. 2000. “Analysis of Behavioural Rejection of Micro-Textured Surfaces and Implications for Recruitment by the Barnacle Balanus Improvisus.” *Journal of Experimental Marine Biology and Ecology* 251 (1): 59–83. https://doi.org/10.1016/S0022-0981(00)00210-0.

Blazek, J. 2015. *Computational Fluid Dynamics: Principles and Applications*. 3rd ed. https://doi.org/https://doi.org/10.1016/B978-0-08-099995-1.00001-4.

Brika, D., and A. Laneville. 1993. “Vortex-Induced Vibrations of a Long Flexible Circular Cylinder.” *Journal of Fluid Mechanics* 250 (1): 481. https://doi.org/10.1017/S0022112093001533.

Butt, U., L. Jehring, and C. Egbers. 2014. “Mechanism of Drag Reduction for Circular Cylinders with Patterned

Surface." *International Journal of Heat and Fluid Flow* 45 (1): 128–34. https://doi.org/10.1016/j.ijheatfluidflow.2013.10.008.

Çengel, Y. A., and A. A. Ghajar. 2011. *Heat and Mass Transfer : Fundamentals & Applications*. 4th ed. McGraw-Hill.

Chang, C. C., R. A. Kumar, and M. M. Bernitsas. 2011. "VIV and Galloping of Single Circular Cylinder with Surface Roughness at 3.0×104≤Re≤1.2×105." *Ocean Engineering* 38 (16): 1713–32. https://doi.org/10.1016/j.oceaneng.2011.07.013.

Demirel, Yigit Kemal, Dogancan Uzun, Yansheng Zhang, Ho Chun Fang, Alexander H. Day, and Osman Turan. 2017. "Effect of Barnacle Fouling on Ship Resistance and Powering." *Biofouling* 33 (10): 819–34. https://doi.org/10.1080/08927014.2017.1373279.

Ding, Lin, Li Zhang, Michael M. Bernitsas, and Che Chun Chang. 2016. "Numerical Simulation and Experimental Validation for Energy Harvesting of Single-Cylinder VIVACE Converter with Passive Turbulence Control." *Renewable Energy* 85: 1246–59. https://doi.org/10.1016/j.renene.2015.07.088.

Gabbai, R. D., and H. Benaroya. 2005. "An Overview of Modeling and Experiments of Vortex-Induced Vibration of Circular Cylinders." *Journal of Sound and Vibration* 282 (3–5): 575–616. https://doi.org/10.1016/j.jsv.2004.04.017.

Gao, Yun, Shixiao Fu, Jungao Wang, Leijian Song, and Yifan Chen. 2015. "Experimental Study of the Effects of Surface Roughness on the Vortex-Induced Vibration Response of a Flexible Cylinder." *Ocean Engineering* 103: 40–54. https://doi.org/10.1016/j.oceaneng.2015.04.052.

Garcia, Elizabeth M.H., and Michael M. Bernitsas. 2018. "Effect of Damping on Variable Added Mass and Lift of Circular Cylinders in Vortex-Induced Vibrations." *Journal of Fluids and Structures* 80: 451–72. https://doi.org/10.1016/j.jfluidstructs.2018.02.005.

Gittens, Jeanette E., Thomas J. Smith, Rami Suleiman, and Robert Akid. 2013. "Current and Emerging Environmentally-Friendly Systems for Fouling Control in the Marine Environment." *Biotechnology Advances* 31 (8): 1738–53. https://doi.org/10.1016/j.biotechadv.2013.09.002.

Glenn Research Center. 2015. "Navier-Stokes Equations." 2015. https://www.grc.nasa.gov/www/k-12/airplane/nseqs.html.

Govardhan, R. N., and C. H. K. Williamson. 2006. *Defining the "modified Griffin Plot" in Vortex-Induced Vibration: Revealing the Effect of Reynolds Number Using Controlled Damping*. *Journal of Fluid Mechanics*. Vol. 561. https://doi.org/10.1017/S0022112006000310.

Griffin, O. M., R. A. Skop, and S. E. Ramberg. 1975. "The Resonant, Vortex-Excited Vibrations of Structures and Cable Systems." In *Offshore Technology Conference*, 14. https://doi.org/10.4043/2319-MS.

Groh, R. 2016. "Boundary Layer Separation and Pressure Drag." Lecture Notes. 2016. https://aerospaceengineeringblog.com/boundary-layer-separation-and-pressure-drag/.

Güven, O, C Farell, and V C Patel. 1980. "Surface-Roughness Effects on the Mean Flow Past Circular Cylinders." *Journal of Fluid Mechanics* 98 (4): 673–701. https://doi.org/10.1017/S0022112080000341.

Hart, John. 2016. "Comparison of Turbulence Modeling Approaches to the Simulation of a Dimpled Sphere." *Procedia Engineering* 147 (0): 68–73. https://doi.org/10.1016/j.proeng.2016.06.191.

Jadidi, P., M. Zeinoddini, M. Soltanpour, A. P. Zandi, and M. S. Seif. 2018. "Towards an Understanding of Marine Fouling Effects on VIV of Circular Cylinders: Aggregation Effects." *Ocean Engineering* 147 (November 2017): 227–42. https://doi.org/10.1016/j.oceaneng.2017.10.037.

Khalak, A., and C. H. K. Williamson. 1997. "Fluid Forces and Dynamics of a Hydroelastic Structure with Very Low Mass and Damping." *Journal of Fluids and Structures* 11 (8): 973–82. https://doi.org/10.1006/jfls.1997.0110.

———. 1999. “Motions, Forces and Mode Transitions in Vortex-Induced Vibrations At Low Mass-Damping.” *Journal of Fluids and Structures* 13 (7–8): 813–51. https://doi.org/10.1006/jfls.1999.0236.

Kinaci, O. K. 2016. “2-D Urans Simulations of Vortex Induced Vibrations of Circular Cylinder at Trsl3 Flow Regime.” *Journal of Applied Fluid Mechanics* 9 (5): 2537–44. https://doi.org/10.18869/acadpub.jafm.68.236.25136.

Koughan, J. 1996. “The Collapse of the Tacoma Narrows Bridge, Evaluation of Competing Theories of Its Demise, and the Effects of the Disaster of Succeeding Bridge Designs.” University of Texas.

Lee, J. H., and M. M. Bernitsas. 2011. “High-Damping, High-Reynolds VIV Tests for Energy Harnessing Using the VIVACE Converter.” *Ocean Engineering* 38 (16): 1697–1712. https://doi.org/10.1016/j.oceaneng.2011.06.007.

Ligrani, P. M., J. L. Harrison, G. I. Mahmmod, and M. L. Hill. 2001. “Flow Structure Due to Dimple Depressions on a Channel Surface.” *Physics of Fluids* 13 (11): 3442–51. https://doi.org/10.1063/1.1404139.

Menter, F. 1994. “Two-Equation Eddy-Viscosity Turbulence Models for Engineering Applications.” *American Institute of Aeronautics and Astronautics* 32 (8): 1598–1605. https://doi.org/10.2514/3.12149.

Mesnard, Olivier, and Lorena A. Barba. 2016. “Reproducible and Replicable CFD: It’s Harder than You Think.”

Mitsudharmadi, H., C. M.J. Tay, and H. M. Tsai. 2009. “Effect of Rounded Edged Dimple Arrays on the Boundary Layer Development.” *Journal of Visualization* 12 (1): 17–25. https://doi.org/10.1007/BF03181939.

Munson, B. R., D. F. Young, and T. H. Okiishi. 1998. *Fundamentals of Fluid Mechanics*. Wiley.

Niemann, H. J., and N. Hölscher. 1990. “A Review of Recent Experiments on the Flow Past Circular Cylinders.” *Journal of Wind Engineering and Industrial Aerodynamics* 33 (1–2): 197–209. https://doi.org/10.1016/0167-6105(90)90035-B.

Nir, Sivan, and Meital Reches. n.d. “ScienceDirect Bio-Inspired Antifouling Approaches : The Quest towards Non-Toxic and Non-Biocidal Materials.” *Current Opinion in Biotechnology* 39 (Figure 2): 48–55. https://doi.org/10.1016/j.copbio.2015.12.012.

Nurioglu, Ayda G., A. Catarina C. Esteves, and Gijsbertus De With. 2015. “Non-Toxic, Non-Biocide-Release Antifouling Coatings Based on Molecular Structure Design for Marine Applications.” *Journal of Materials Chemistry B* 3 (32): 6547–70. https://doi.org/10.1039/c5tb00232j.

Owen, David, Yigit Kemal Demirel, Elif Oguz, Tahsin Tezdogan, and Atilla Incecik. 2018. “Investigating the Effect of Biofouling on Propeller Characteristics Using CFD.” *Ocean Engineering* 159 (February): 505–16. https://doi.org/10.1016/j.oceaneng.2018.01.087.

Park, H. 2012. “Mapping of Passive Turbulence Control to Flow Induced Motions of Circular Cylinders.” University of Michigan.

Park, H., R. A. Kumar, and M. M. Bernitsas. 2013. “Enhancement of Flow-Induced Motion of Rigid Circular Cylinder on Springs by Localized Surface Roughness at 3×10 4 ≤Re≤1. 2×10 5.” *Ocean Engineering* 72: 403–15. https://doi.org/10.1016/j.oceaneng.2013.06.026.

———. 2016. “Suppression of Vortex-Induced Vibrations of Rigid Circular Cylinder on Springs by Localized Surface Roughness at 3×104≤Re≤1.2×105.” *Ocean Engineering* 111: 218–33. https://doi.org/10.1016/j.oceaneng.2015.10.044.

Pletcher, R., D. Anderson, and J. Tannehill. 1984. *Computational Fluid Mechanics and Heat Transfer*. McRaw-Hill.

Raghavan, K. 2007. “Energy Extraction from a Steady Flow Using Vortex Induced Vibration.” The University of Michigan.

Raghavan, K., and M. M. Bernitsas. 2011. “Experimental Investigation of Reynolds Number Effect on Vortex Induced

Vibration of Rigid Circular Cylinder on Elastic Supports." *Ocean Engineering* 38 (5–6): 719–31. https://doi.org/10.1016/j.oceaneng.2010.09.003.

Roshko, A., and W. Fiszdon. 1969. "On the Persistance of Transition in the Nearwake." *Problems of Hydrodynamics and Continuum Mechanics*, 606–16.

Rostami, Ali Bakhshandeh, and Mohammadmehdi Armandei. 2017. "Renewable Energy Harvesting by Vortex-Induced Motions: Review and Benchmarking of Technologies." *Renewable and Sustainable Energy Reviews* 70 (June 2016): 193–214. https://doi.org/10.1016/j.rser.2016.11.202.

Salim, S. M., and S. C. Cheah. 2009. "Wall Y+ Strategy for Dealing with Wall-Bounded Turbulent Flows." In *Proceedings of the International MultiConference of Engineers and Computer Scientists*. Vol. 2.

Sarpkaya, T. 2004. "A Critical Review of the Intrinsic Nature of VIV." *Fluid Mechanics and Its Applications* 75: 159–61. https://doi.org/10.1007/978-94-007-0995-9_10.

Savory, E., and N. Toy. 1989. "The Seperated Shear Layers Associated with Hemispherical Bodies in Turbulent Boundary Layers." In *Advances in Wind Engineering*, 291–300. https://doi.org/10.1016/B978-0-444-87156-5.50039-4.

Schewe, G. 1983. "On the Force Fluctuations Acting on a Circular Cylinder in Cross Flow from Subcritical to the Transcritical Reynolds Number." *Journal of Fluid Mechanics* 133: 265–85. https://doi.org/https://doi.org/10.1017/S0022112083001913.

Schultz, Michael P. 2007. "Effects of Coating Roughness and Biofouling on Ship Resistance and Powering." *Biofouling* 23 (5): 331–41. https://doi.org/10.1080/08927010701461974.

Scobie, James A., Carl M. Sangan, and Gary D. Lock. 2014. "Flow Visualisation Experiments on Sports Balls." *Procedia Engineering* 72: 738–43. https://doi.org/10.1016/j.proeng.2014.06.125.

Scruton, C. 1955. "Wind-Excited Oscillations of Tall Stacks." *Engineering*, no. 199: 806–8.

———. 1965. "On the Wind-Excited Oscillations of Stacks, Towers and Masts." In *International Conference on the Wind Effects on Buildings and Structures, 1963.*, 1–37. Teddington, Middlesex.

Shiels, D., A. Leonard, and A. Roshko. 2001. "FLOW-INDUCED VIBRATION OF A CIRCULAR CYLINDER AT LIMITING STRUCTURAL PARAMETERS." *Journal of Fluids and Structures*, no. 15: 3–21. https://doi.org/10.1006/jfls.2000.0330.

Shur, Mikhail L., Philippe R. Spalart, Mikhail Kh Strelets, and Andrey K. Travin. 2015. "An Enhanced Version of Des with Rapid Transition from RANS to Les in Separated Flows." *Flow, Turbulence and Combustion* 95 (4): 709–37. https://doi.org/10.1007/s10494-015-9618-0.

Soti, Atul Kumar, Jisheng Zhao, Mark C. Thompson, John Sheridan, and Rajneesh Bhardwaj. 2018. "Damping Effects on Vortex-Induced Vibration of a Circular Cylinder and Implications for Power Extraction." *Journal of Fluids and Structures* 81: 289–308. https://doi.org/10.1016/j.jfluidstructs.2018.04.013.

Spalart, P. R., S. Deck, M. L. Shur, K. D. Squires, M. Kh Strelets, and A. Travin. 2006. "A New Version of Detached-Eddy Simulation, Resistant to Ambiguous Grid Densities." *Theoretical and Computational Fluid Dynamics* 20 (3): 181–95. https://doi.org/10.1007/s00162-006-0015-0.

Sun, Hai, Eun Soo Kim, Gary Nowakowski, Erik Mauer, and Michael M. Bernitsas. 2016. "Effect of Mass-Ratio, Damping, and Stiffness on Optimal Hydrokinetic Energy Conversion of a Single, Rough Cylinder in Flow Induced Motions." *Renewable Energy* 99: 936–59. https://doi.org/10.1016/j.renene.2016.07.024.

Sun, Hai, Chunhui Ma, and Michael M. Bernitsas. 2018. "Hydrokinetic Power Conversion Using Flow Induced Vibrations with Nonlinear (Adaptive Piecewise-Linear) Springs." *Energy* 143: 1085–1106. https://doi.org/10.1016/j.energy.2017.10.140.

Tesler, Alexander B., Philseok Kim, Stefan Kolle, Caitlin Howell, Onye Ahanotu, and Joanna Aizenberg. 2015. "Extremely Durable Biofouling-Resistant Metallic Surfaces Based on Electrodeposited Nanoporous Tungstite Films on Steel." *Nature Communications* 6: 1–10. https://doi.org/10.1038/ncomms9649.

Teverovskii, B.M. 1968. "Effect of Surface Roughness on the Vibration of a Cylinder in Hydrodynamic Conditions." *Russian Engineering Journal* 68 (12).

Tu, J., G. H. Yeoh, and L. Chaoqun. 2012. *Computational Fluid Dynamics: A Practical Approach*. 2nd Kindle. Butterworth-Heinemann.

University of Michigan. 2019. "MRELab." 2019. http://www.umich.edu/~mrel/.

Vandiver, J. Kim. 2012. "Damping Parameters for Flow-Induced Vibration." *Journal of Fluids and Structures* 35: 105–19. https://doi.org/10.1016/j.jfluidstructs.2012.07.002.

Villarreal, David J. Yáñez. 2018. "VIV Resonant Wind Generators."

Vortex Bladeless. 2019. "Vortex Bladeless Current Stage." 2019. https://vortexbladeless.com/story-vortex-bladeless-tech-startup/.

Vortex Hydro Energy. 2019. "VIVACE: How It Works." 2019. https://www.vortexhydroenergy.com/technology/how-it-works/.

Williamson, C. H. K. 1996. "VORTEX DYNAMICS IN THE CYLINDER WAKE." *Annual Review of Fluid Mechanics* 28 (1): 477–539. https://doi.org/10.2514/6.1999-3806.

Williamson, C. H. K., and R. N. Govardhan. 2004. "Vortex-Induced Vibrations." *Annual Review of Fluid Mechanics* 36 (1): 413–55. https://doi.org/10.1146/annurev.fluid.36.050802.122128.

———. 2008. "A Brief Review of Recent Results in Vortex-Induced Vibrations." *Journal of Wind Engineering and Industrial Aerodynamics* 96 (6–7): 713–35. https://doi.org/10.1016/j.jweia.2007.06.019.

Williamson, C. H. K., and A. Roshko. 1988. "Vortex Formation in the Wake of an Oscillating Cylinder." *Journal of Fluids and Structures* 2 (4): 355–81. https://doi.org/https://doi.org/10.1016/S0889-9746(88)90058-8.

Wu, W., M. M. Bernitsas, and K. Maki. 2014. "RANS Simulation Versus Experiments of Flow Induced Motion of Circular Cylinder With Passive Turbulence Control at 35,000 < RE < 130,000." *Journal of Offshore Mechanics and Arctic Engineering* 136 (4). https://doi.org/10.1115/1.4027895.

Yamagishi, Y., and M. Oki. 2004. "Effect of Groove Shape on Flow Characteristics around a Circular Cylinder with Grooves." *The Visualisation Society of Japan* 7 (3): 209–16.

Young, Me, and A Ooi. 2007. "Comparative Assessment of LES and URANS for Flow Over a Cylinder at a Reynolds Number of 3900." *Proc. of the 16th Australasian Fluid Mechanics Conference (AFMC)*, no. December: 1063–1070.

Yu, H., W. Huang, and X. K. Wang. 2013. "Dimple Patterns Design for Different Circumstances." *Lubrication Science* 25: 67–78. https://doi.org/10.1002/ls.168.

Zdravkovich, M. M. 1990. "Conceptual Overview of Laminar and Turbulent Flows Past Smooth and Rough Circular Cylinders." *Journal of Wind Engineering and Industrial Aerodynamics* 33 (1–2): 53–62. https://doi.org/10.1016/0167-6105(90)90020-D.

———. 1997. *Flow Around Circular Cylinders Volume 1: Fundamentals*. Oxford University Press.

Zeinoddini, M., A. Bakhtiari, M. Ehteshami, and M. S. Seif. 2016. "Towards an Understanding of the Marine Fouling Effects on VIV of Circular Cylinders: Response of Cylinders with Regular Pyramidal Roughness." *Applied Ocean Research* 59: 378–94. https://doi.org/10.1016/j.apor.2016.05.013.

Zeinoddini, M, A Bakhtiari, F Schoefs, and A P Zandi. 2017. "Towards an Understanding of Marine Fouling Effects

on the Vortex-Induced Vibrations of Circular Cylinders : Partial Coverage Issue." *Biofouling* 7014: 1–13. https://doi.org/10.1080/08927014.2017.1291803.

Zhang, Dahai, Hai Sun, Wenhao Wang, and Michael M Bernitsas. 2018. "Rigid Cylinder with Asymmetric Roughness in Flow Induced Vibrations." *Ocean Engineering* 150 (154): 363–76. https://doi.org/10.1016/j.oceaneng.2018.01.005.

Zhou, Bo, Xikun Wang, Wei Guo, Wie Min Gho, and Soon Keat Tan. 2015. "Control of Flow Past a Dimpled Circular Cylinder." *Experimental Thermal and Fluid Science* 69: 19–26. https://doi.org/10.1016/j.expthermflusci.2015.07.020.

Zhou, Z., F. Scuiller, J. F. Charpentier, F. Scuiller, M. Benbouzid, Ti. T. An, and J. Frédéric. 2014. "An Up-to-Date Review of Large Marine Tidal Current Turbine Technologies." In *IEEE PEAC*, 448–84. https://doi.org/10.1109/PEAC.2014.7037903.

Appendix 1 – Fluid Domains

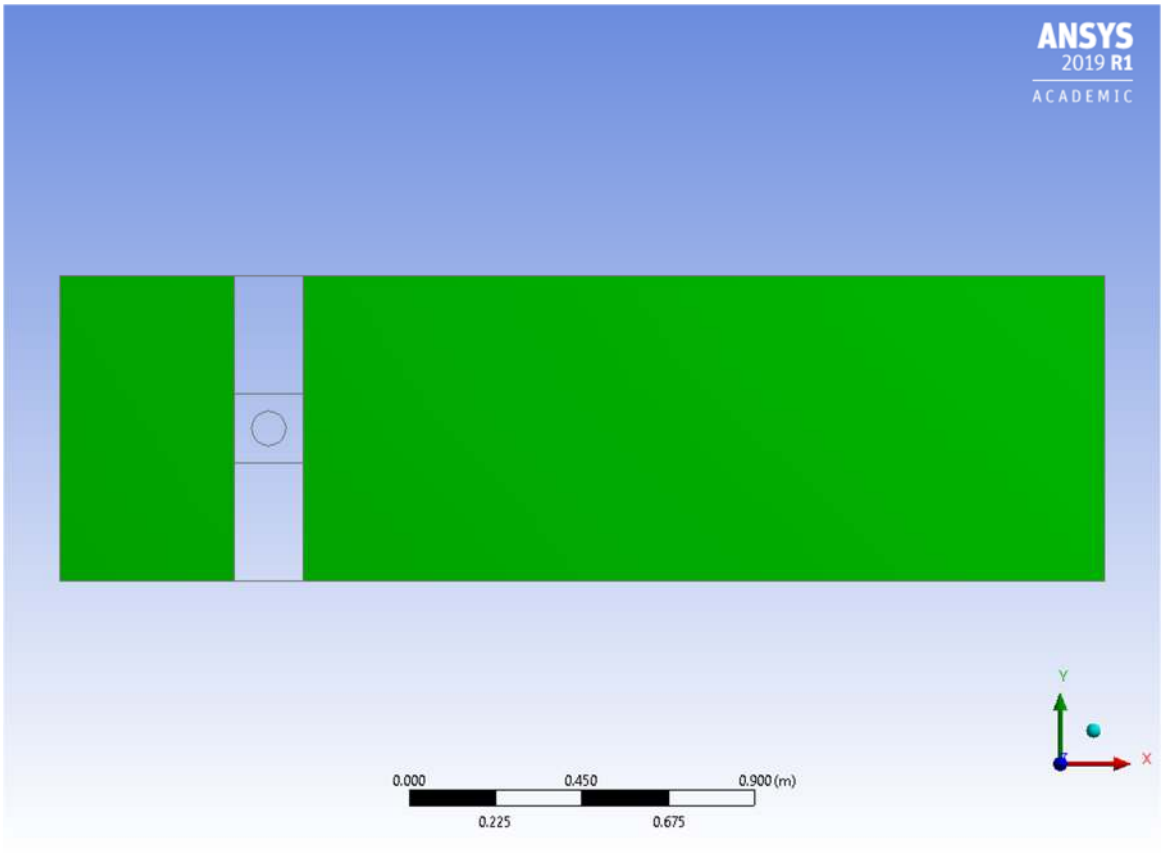

Outer domain

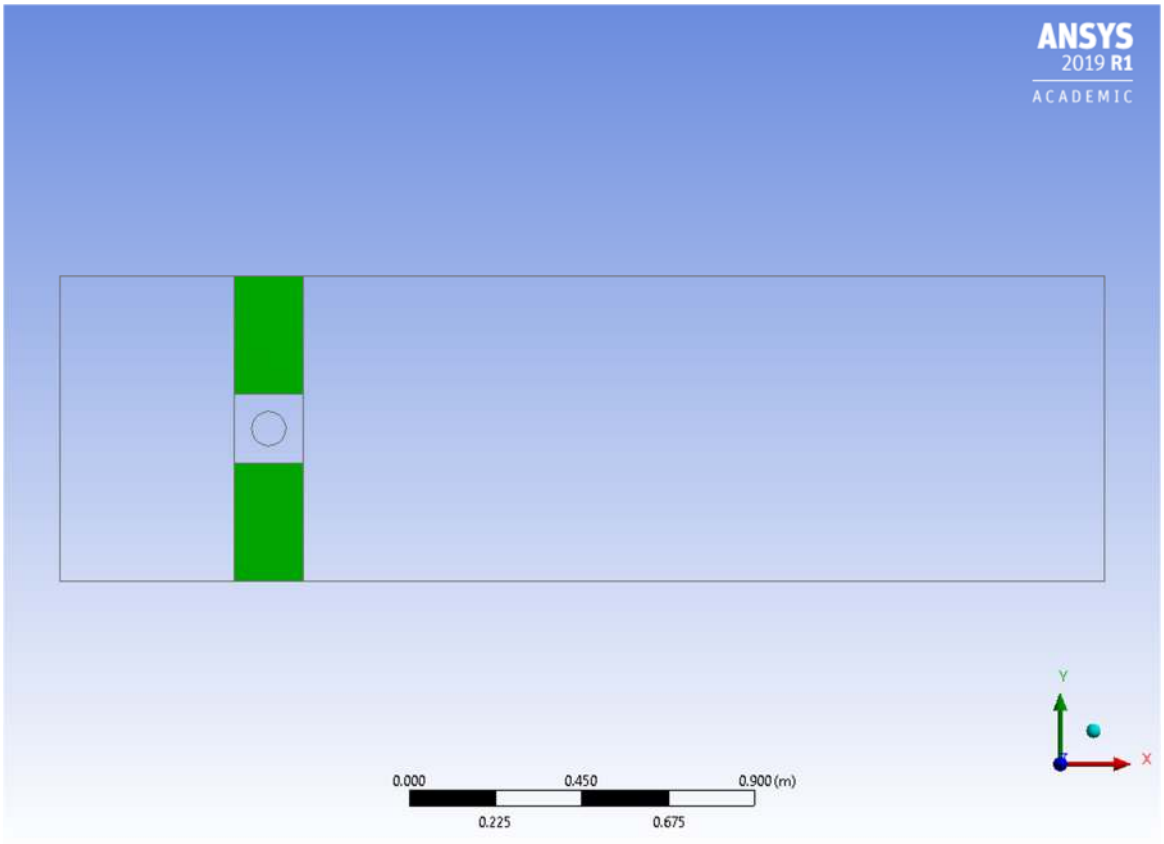

Moving sub-domain

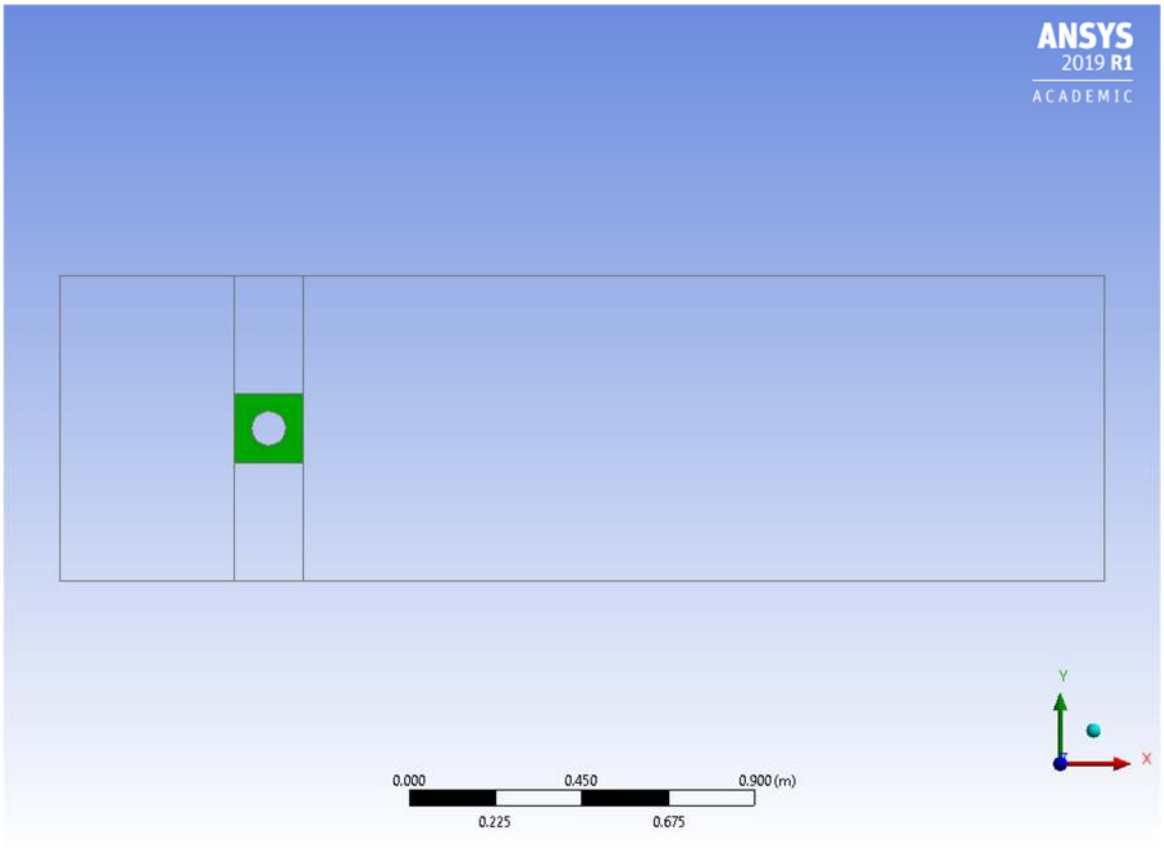

Inner sub-domain

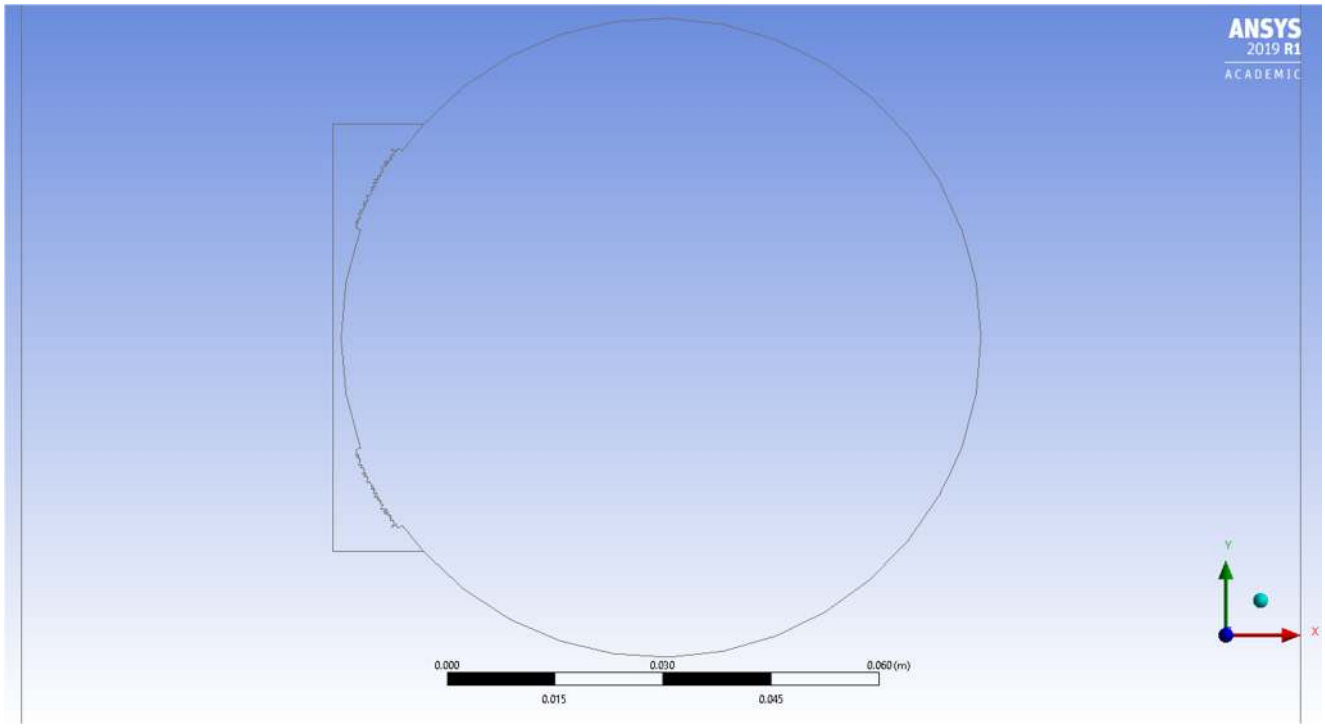

PTC Micro domain

Appendix 2 – Sub-domain Mesh Diagrams

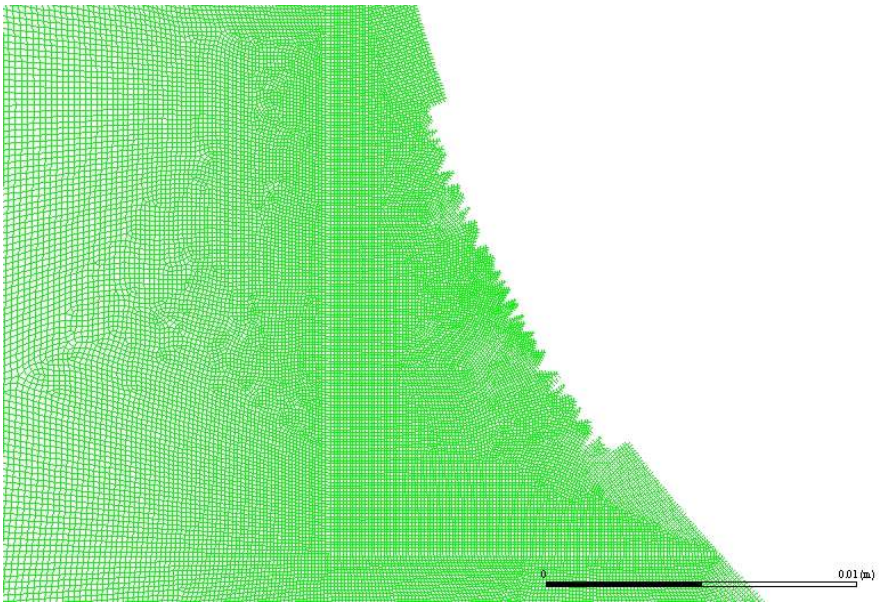

PTC micro domain

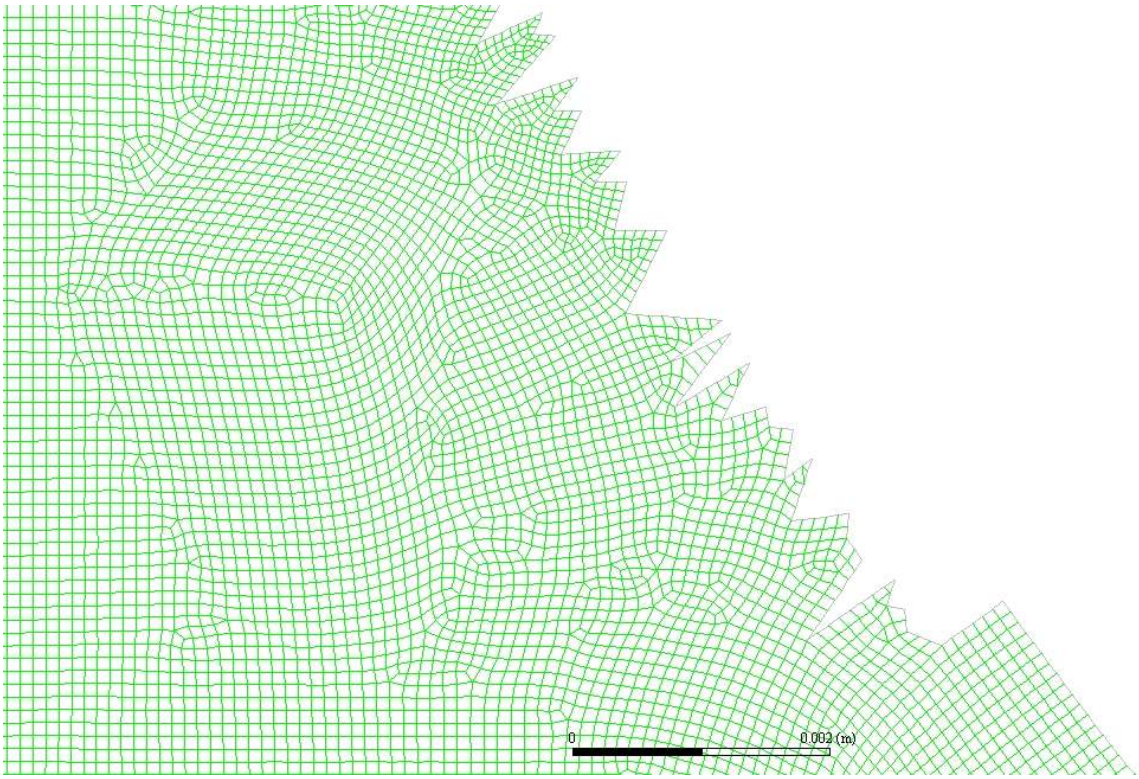

PTC close-up

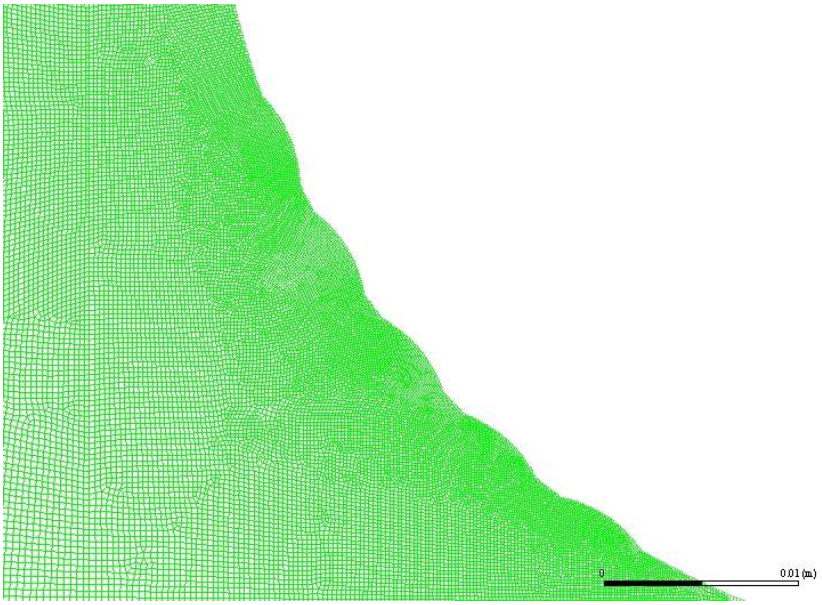

Dimple (D1) inner sub-domain close-up

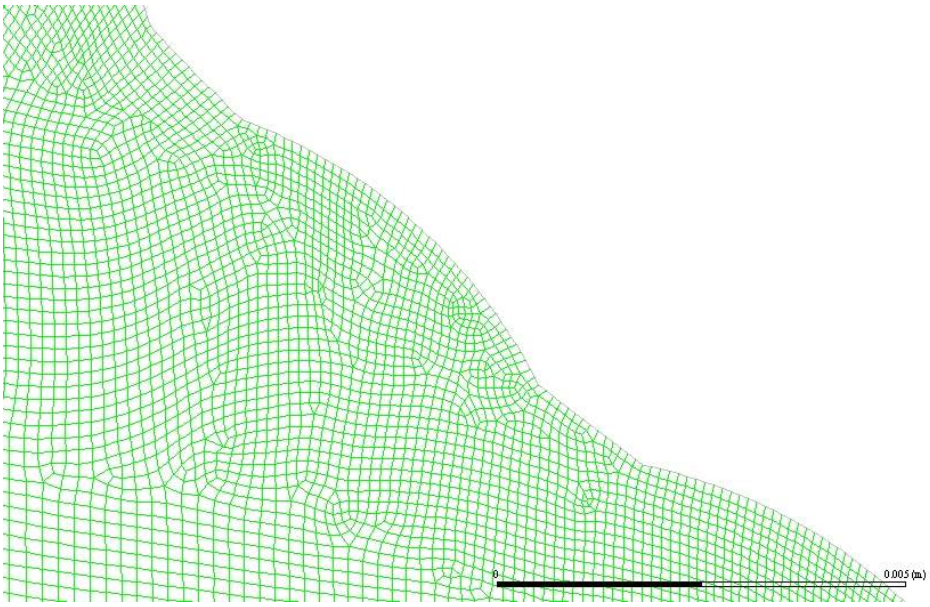

Dimple (D1) close up